Modelling aeroelastic deformation of soft wing membrane kites

J.A.W. Poland

TU Delft

Modelling aeroelastic deformation of soft wing membrane kites

by

J.A.W. Poland

to obtain the degree of Master of Science in
Aerospace Engineering at Delft University of Technology
to be defended publicly on 26th of January, 2022 at 14:00.

Supervisor:	Dr.-Ing. R. Schmehl	TU Delft
Thesis committee:	Dr.-Ing. R. Schmehl	TU Delft, chair
	Prof. dr. ir. C.J. Simão Ferreira	TU Delft
	Dr. ir. J. Sodja	TU Delft
	Ir. M. Schelbergen	TU Delft
	Ir. J. Breuer	Kitepower B.V.

An electronic version of this thesis is available at `https://repository.tudelft.nl/`

Cover Image: Footage shot on 03/05/2021 during experiments with S. Jonard.

TU Delft

Delft University of Technology

The undersigned hereby certify that they have read and recommend to the Faculty of Aerospace Engineering and Department of Aerodynamics & Wind Energy for acceptance a thesis entitled

"Modelling aeroelastic deformation of soft wing membrane kites"

by

J.A.W. Poland

in partial fulfilment of the requirements for the degree of

Master of Science in Aerospace Engineering at TU Delft

Dated: 26 January 2022

Thesis committee:

Dr.-Ing. R. Schmehl (TU Delft)

Prof. dr. ir. C.J. Simão Ferreira (TU Delft)

Dr. ir. J. Sodja (TU Delft)

Ir. M. Schelbergen (TU Delft)

Ir. J. Breuer (Kitepower B.V.)

Preface

“Airplanes are unanchored kites.” - Louis Ferber (1862 - 1900)

Kite research within the airborne wind energy sector was something I stumbled upon about two years ago. I never expected to find a research domain that aligns so perfectly with what I find interesting, what I consider ethically just and what I am good at. Besides the research subject itself, the advice and company of many around me are what made this particular research so enjoyable.

I would like to express my gratitude towards my daily supervisor R. Schmehl. His input, insights, motivational quotes, introductions, and overall company was much appreciated. I was especially fond of our weekly progress meetings over a cup of coffee in a local cafe in Rotterdam.

I would furthermore like to thank M. Schelbergen for always answering my questions and his general continuous involvement. J. Breuer for providing me with much needed data and answers. J. Blom for being an ideal colleague, his advice and most welcome company on our many kite field trips. S. Jonard for advice and requesting me to do experiments with him using one of my kites. D. Eijkelhof for sharing his experiences and providing me with some early on research tips. Furthermore, R. Kooij and W. Arink for their critical comments. The airborne wind energy research group for their general advice. My parents for their unconditional support and advice on where to focus on. My roommates for their company in our home office, making my research days, and lunches in particular, a lot of fun.

J.A.W. Poland
Rotterdam, January 2022

Abstract

Kitepower B.V. (https://thekitepower.com/) is an airborne wind energy (AWE) company, that generates energy with a leading-edge inflatable (LEI) soft-wing membrane kite. Improving energy generation can be done by increasing the aerodynamic performance of the kite, which is ideally done using shape-performance optimization procedures that require fast models. Fast and accurate LEI kite models are difficult to develop, due to the flexible nature of the kite. The flexibility allows several shape changes, which substantially change the aerodynamic characteristics [33, 47, 68]. The changing shape forms a complex aeroelastic problem, which is generally solved using fluid-structure interaction (FSI) models [7]. The two main deformation modes, symmetrical bending and asymmetrical twist, are used to control the force production and turn the kite [8, 51]. This research will focus on predicting the shape deformation, i.e. the structural component of a FSI model, using the V3 LEI kite of Kitepower B.V. as research subject. The model should be modular, fast and accurate to excel as a building block for the above-mentioned optimization procedure.

It is important to experimentally validate models, therefore, footage shot in flight was analyzed using photogrammetry. The width changes were analyzed, because they provide a good indication of the wing bending. The asymmetric deformation results were not of sufficient quality for quantitative analysis, therefore, only the symmetric deformation results are used quantitatively. The local trailing-edge (TE) lengths are measured, because its linked to the local membrane billowing, which is expected to affect the aerodynamics and the global shape.

The kite wing is described as a wireframe representation consisting of multiple plates. The leading-edge (LE) and side edges of the plate represent the tubular frame and are of constant length. The TE is also of constant length, except for when billowing effects are included. Because the V3's tubular frame is supported on both the LE and TE by the bridle line system, all corners of all plates represent bridle line attachment points. The point locations determine the shape of the kite wing and are calculated using a bridle line system representation, calculation algorithm and geometric actuation input. Symmetric actuation input affects the bending deformation mode and asymmetric actuation, i.e. steering, the twist deformation mode.

The best formulated geometrical calculation algorithm is called trilateration, which has a runtime of 2 ms. To work, it requires empirical relations and a straight bridle line assumption. Because slacking bridles were observed in the symmetrical state, only 7-plates could be taken into account. Slacking bridles were furthermore observed in the asymmetrical state, therefore, asymmetrical actuation input is not simulated. A force-based particle system model (PSM) was formulated to resolve the slacking bridle-induced problems, which has a runtime of 40 s. It is pseudo-physical due to the non-physical inputs, used for the spring representation of the bridles and plate edges. The PSM solves a dynamic problem of which only the steady-state solution is considered relevant and physical. Two symmetric actuation inputs were used, both 7-plate trilateration-based and 9-plate PSM-based show best result. The present errors are mainly attributed to modeling incorrect bridle line lengths, starting from the wrong initial shape and using inaccurate loading conditions.

It has become clear that the PSM can predict the change in width due to symmetrical actuation within 1% of the experimentally obtained width. Because of its relatively low computational cost, non-dependence on empirical relations, aerodynamic model coupling potential and its ability to predict both main deformation modes, the PSM is considered an ideal structural building block. Combined with the insights from this research, the PSM forms a solid foundation for the next generation of FSI based kite design tools. The main recommendation is to validate the asymmetrical deformation, by acquiring more accurate input and validation data.

Contents

Nomenclature

Abbreviations

Abbreviation	Definition
AWE	Airborne wind energy
AWES	Airborne wind energy system
CAD	Computer aided design
Ch.	Chapter
CFD	Computational fluid dynamics
DOF	Degrees of freedom
EOM	Equations of motion
FE	Finite element method
Fig.	Figure
FSI	Fluid-structure interaction
HAWT	Horizontal axis wind turbine
KCU	Kite control unit
LE	Leading edge
LEI	Leading edge inflatable
PSM	Particle system model
QSM	Quasi-steady model
Sec.	Section
TE	Trailing edge
V3	The 25m^2 kite of Kitepower B.V.
2D	Two-dimensional
3D	Three-dimensional

Latin symbols

Symbol	Definition	Unit
a	Line between middle LE point and tip	m
A_t	Area of the tetrahedon	m^2
b	Line between KCU and tip	m
C	Damping constant	N s m^{-1}
C_D	Drag coefficient	-
C_L	Lift coefficient	-
$\vec{c}_{m,i}$	Vector representing chord of plate i	m
c_{ref}	Reference chord	m
d	Line between KCU and middle LE point	m
$D_{i,j}$	Length of diagonal line i,j	m
e	Line between tip and middle TE point	m
$E_{i,j}$	Length of edge i,j	m
f_i	Frequency i	s^{-1}
$\vec{F}_d$	Damping force	N
$\vec{F}_r$	Resultant force	N
$\vec{F}_s$	Spring force	N
K	Spring constant	N m^{-1}
$\vec{L}$	Lift force	N

Symbol	Definition	Unit
L^*	Lift scaling factor	-
$l_{edge,i}$	Edge length of plate i	m
l_d	Depower tape length	m
l_{im}	Imaginary line length	m
L_p	Distance from KCU to pulley	m
$\vec{L_p}$	Plate lift force	N
l_0	Spring restitution length	m
LE_{mp}	Middle point of the leading edge	m
$\vec{LE_i}$	Vector representing the LE of plate	-
N	Number of samples	-
m	Mass	kg
P_{cross}	Line-of-sight crossing point on TE	m
P_i	Point i	m
$P_{l,i}$	Plate i	$-$
$\vec{q}$	Positions of the particles	m
r	Distance from LE_{mp} to P_{cross}	m
R	Distance from KCU to P_{cross}	m
S	Surface area	m^2
s	Semi-perimeter	m
SE	Standard error	m
$S_{t,i}$	Strut i	i
$\vec{u}$	Velocities of the particles	m/s
$\vec{u_i}$	Unit vector in direction i	-
u_p	Power setting	-
u_s	Steering setting	-
$\vec{v_a}$	Velocity	m/s
V_t	Volume of the tetrahedon	m^3
$\vec{v_w}$	Wind velocity	m/s
W	Width between tip bridle line attachment points	m
x	Position	m
$\dot{x}$	Velocity	m/s
$\ddot{x}$	Acceleration	m/s^2
x^*	x-axis in new frame	-
x_p	x-coordinate of pulley	m
x_p^*	x-coordinate of pulley in new frame	-
y_p	y-coordinate of pulley	m
z_p	z-coordinate of pulley	m
$z_{p_{Cross}}$	z-coordinate of P_{cross}	m

Greek symbols

Symbol	Definition	Unit
α	Angle of attack	°
α_d	Depower angle	°
α_s	Side-slip angle	°
β	Elevation angle	°
Δl_d	l_d change between the powered and depowered state	-
ΔL	Extension of L_p	m
Δl	Extension of the spring	m
θ	Angle between y-axis and pulley line-of-sight	°
μ	Mean of the measured widths	m

Symbol	Definition	Unit
ρ	Density	kg/m^3
σ	Standard deviation	-

List of Figures

List of Tables

1

Introduction

To counteract global warming, many countries have set ambitious targets to transition from fossil fuels to renewable energy sources [52].Whether or not wind energy alone could theoretically supply all the world's energy needs is an ongoing debate between scientists [36].The horizontal axis wind turbine (HAWT) is the most commonly used instrument to perform the desired conversion of kinetic energy present in the atmosphere to electrical energy. Looking at the structural components of a conventional HAWT one finds that most mass does not directly contribute to the power production, i.e. more than half of the power is produced by only the outer 30% of the blades [16]. An alternative to wind turbines is airborne wind energy systems (AWESs), these systems use a kite to harvest kinetic energy. According to J. Breukels, a kite is defined as:

> *"A tethered heavier-than-air device able to achieve flight by generating a resulting aerodynamic force, which is countered by the mass of the device and the tension force in the tether"* [8].

By using kites that resemble the tips of a HAWT, AWESs require less material for the same power generation (see Fig. 1.1) [39]. Another advantage of AWES is their ability to operate at greater altitudes where generally more kinetic energy is present [2]. This, in turn, increases the operational bandwidth and reduces the turbulence experienced by the AWES.

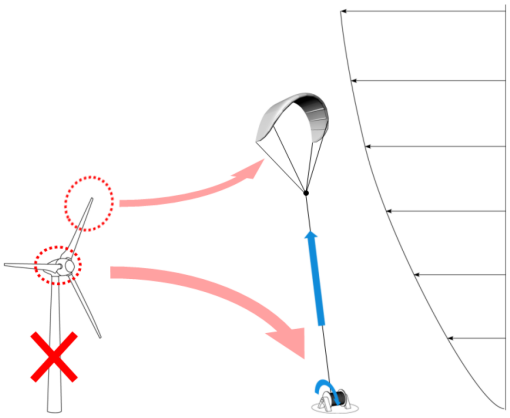

Figure 1.1: How an AWES uses only the essential parts of an HAWT [58].

Figure 1.2: An illustration of Kitepower B.V. its AWES, used for the PostNL Innovation Stamp series [29].

The combination of higher power output to required material ratio and increased operating ranges has led to an increased academic and commercial interest in AWESs over the last decade (see Fig. 1.2). The number of institutions active in this field worldwide grew from less than five in 2000 to over 60 in 2018 [59]. Considering the immaturity of the airborne wind energy sector it is not surprising that several

challenges are still present, e.g. proving safe autonomous operation over long periods. Other focus points are reducing the cost of production, installation and operating costs, reducing the environmental impact and increasing the energy yield of the system. The latter can be achieved by increasing the operational bandwidth or increasing the system efficiency. Increasing operational bandwidth is achieved through a more optimized geographical system placing or by developing a lighter system. Increasing system efficiency can be done by increasing the generator conversion efficiency and increasing the tether force, possible through flight path optimization and increased aerodynamic performance. The latter is often expressed as the lift-to-drag ratio and increasing its value can also lead to a lighter system, making its effect on the energy yield twofold.

1.1. Types of AWESs

In 1980, Loyd analytically showed the large potential of a cross-wind flying kite generation system by quantifying the tether force and comparing it to a regular flying kite. A part of the potential arises from the difference in kite velocity. Force generation scales with the observed apparent velocity ($\vec{v_a}$) squared, increasing the kite velocity is, therefore, an effective way of increasing the force. Loyd also proposed two different operating modes called the lift- and drag power mode which covers all variants of AWESs existent today [39]. In the lift power mode, electricity is generated on the ground by a drum connected to a generator and thus varying the airborne tether length. In the drag power mode electricity is generated on the kite itself and then transported to the ground through a tether of constant length. Loyd concluded that the theoretical performance of the two modes is roughly the same and that one should maximize the lift-to-drag ratio to maximize the energy extraction. As of today no obvious winner has been identified and in both lift- and drag power modes multiple institutions are actively working on implementation solutions (see Fig. 1.3). [41]

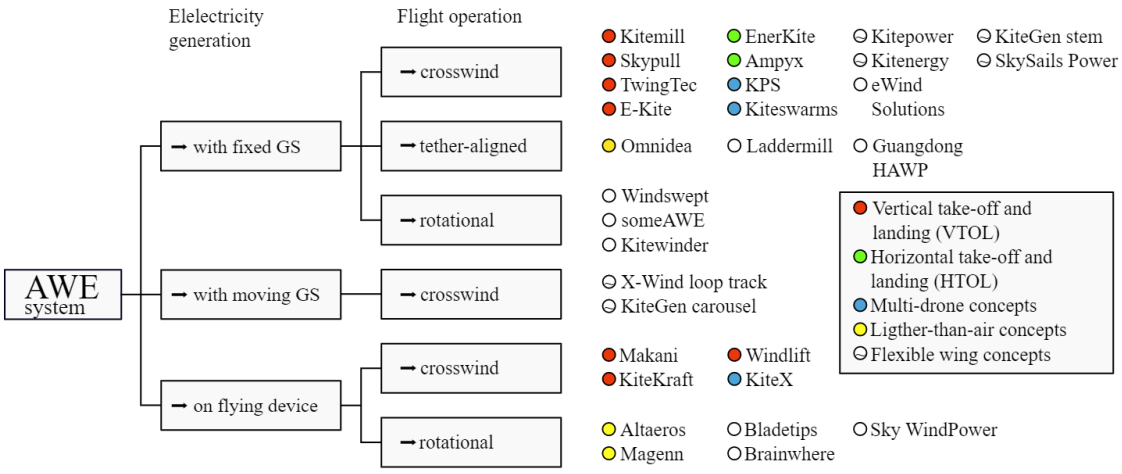

Figure 1.3: Overview of the AWESs [59].

The different kite wings can be categorized into soft-wings and fixed-wings. Soft-wings are generally lighter in comparison to fixed-wings allowing them to operate at lower wind speeds. Another benefit is that the damage of a crash is generally less severe, to both the system and its surroundings. The aerodynamics of the fixed-wing AWES is comparable to aircraft aerodynamics and therefore currently better understood. Soft wing membrane AWES has been shown to have the potential for higher lift-to-drag ratios compared to fixed-wings and the prime reason is the flexibility of the membrane [4]. Maughmer was more conservative in his statements and concluded that flexible sail wings have very competitive lift-to-drag ratios compared to fixed wings [42]. The lift-to-drag ratio is relevant because it determines the speed a kite can obtain which relates to the tether force it can generate [61].

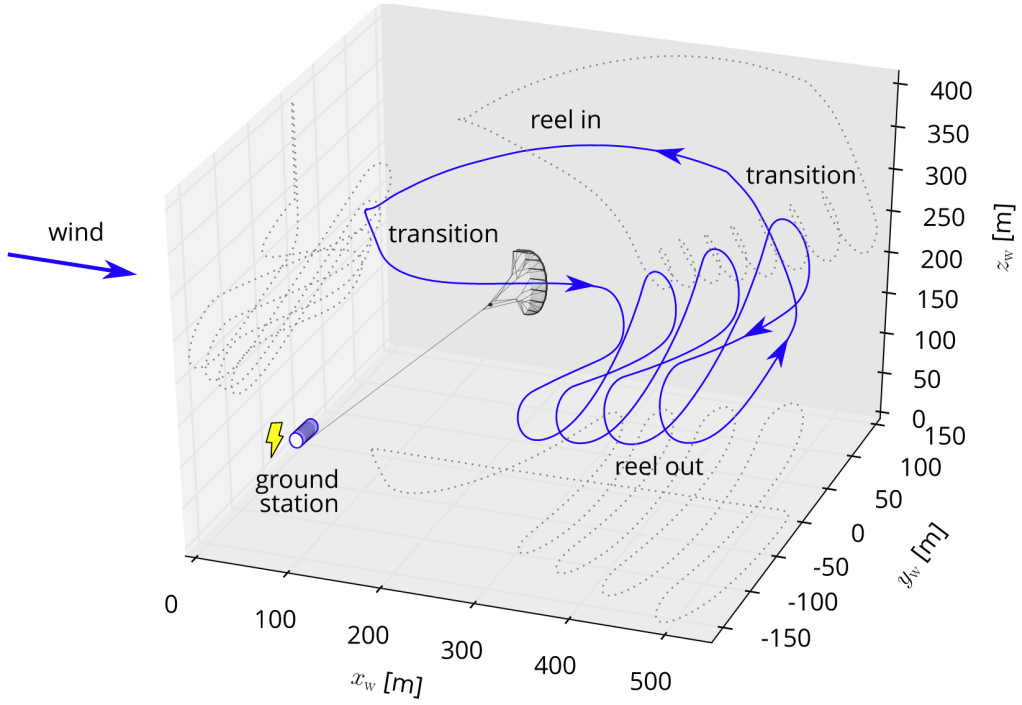

Figure 1.4: Visualisation of the pumping cycle operation with the different phases identified [59].

Within the soft wing category, there is a soft wing membrane leading edge inflatable (LEI) kite. Kitepower B.V. (`https://thekitepower.com/`) amongst other airborne wind energy companies use a LEI kite to generate energy. Kitepower B.V. is a commercial spin-off from the Delft University of Technology that operates in the lift power mode where it flies pumping cycle operations (see Fig. 1.4). The operations go in cycles, first the kite reels out the tether with figure of eight movements and once a certain distance is reached the reel-in phase begins and the generator starts reeling in the tether [47]. Power is needed to do so, therefore the pumping cycle operation does not continuously deliver power. This is a downside that can be resolved by operating multiple kites simultaneously off-phase.

1.2. The V3 LEI kite

The design of the V3 LEI kite is based on the surf-kite, in particular the Generatrix Hydra V7 kite. Oehler and Schmehl amongst others have previously performed research on the V3 and identified the need for further research efforts [47]. Research into LEI kite behavior would benefit Kitepower B.V. and other relevant AWES companies because it could help them improve overall system efficiency. The V3 is furthermore selected as a research subject because of the existing and available experimental data. Another reason is the existence of simulation results thanks to the work of other researchers [14, 38, 53].

The V3 kite consists of a leading-edge (LE) tube in spanwise direction and strut tubes in chordwise direction, which both are pressurized with air (see Fig. 1.5). This tubular frame is connected by a membrane called the canopy and together they form a LEI kite. The rear end is generally referred to as the trailing edge (TE). The control pod used for automatic control in flight, also called the kite control unit (KCU), is placed in between the tether and the bridle line system. The bridles attached to the LE are often referred to as the power lines and those attached to the TE as the steering lines. Most force is namely carried by the power lines and actuation is done using the rear steering lines.

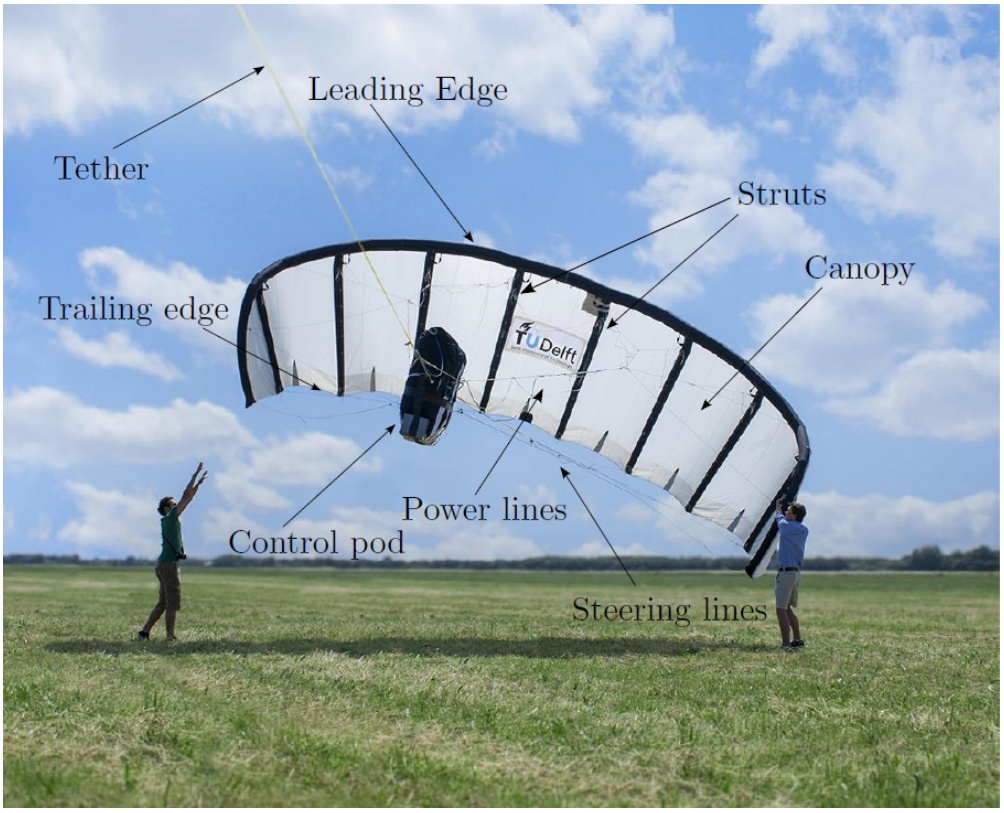

Figure 1.5: Video still of the V3, indicating the different components [3].

To assess how much and where there is room for improvement one could determine the theoretical maximal power output and on what it is dependent on. Fechner and Schmehl calculated the theoretical total efficiency for the V3 and found estimates around 50% to 60% [20]. The importance of the generator efficiency was stressed and due to its increase for increasing kite sizes, larger kites are expected to be able to have higher total efficiencies. Besides the generator efficiency, the lift-to-drag ratio is considered another area where improvement possibilities lie. Costello et al. developed a different framework with which one can assess the maximum average power a general LEI AWES kite can generate [11]. In this framework, the lift-to-drag ratio comes out as the most effective way to increase power production.

1.3. Aeroleastic effects

For high pumping cycle efficiency, one wants to maximize the generated force during the reel-out phase and minimize during the reel-in phase. Force generation of any body in a fluid is a function of the fluid properties, the fluid velocity, the shape of the body, the body's velocity and the angle of attack (α), i.e. the orientation it has towards the incoming fluid. Kitepower B.V. achieves force control by changing the kite body its: velocity, shape and orientation. A change in kite velocity is achieved by not flying figures of eight during the reel-in phase. The lift-to-drag (C_L/C_D) ratio is controlled by changing the power setting and is a function of the shape and angle of attack. The power setting affects the angle of attack by pitching the kite (see Fig. 1.6) and it affects the shape, mainly through inducing a bending deformation that changes the anhedral angle. Another relevant deformation mode is the asymmetric twist of the kite, which is needed, together with roll, for turning maneuvers [8].

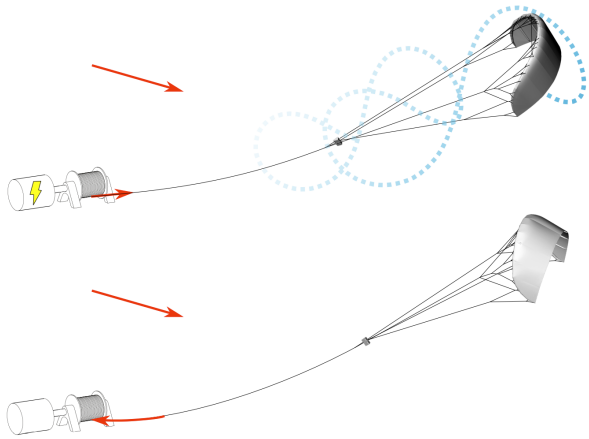

Figure 1.6: Reel-in and reel-out phase of a pumping cycle operation where the change in kite orientation with respect to the wind becomes clear [68].

Figure 1.7: Deformation of a LEI surf-kite during a left-turning maneuver [17].

The deformations are the result of the interaction between aerodynamic force dependent on the shape and the structural force, arising from resisting the aerodynamic force-induced shape deformation (see Fig. 1.7). The result is a complex aeroelastic problem, which is generally solved using Fluid-structure interaction (FSI) models. As stated by Bosch et al. incorporating the relevant macro-scale deformations, bending and asymmetric twist that is, into a strongly coupled FSI model is required to get accurate results [6]. Problematic for existing FSI models is that they either have too high computational cost or don't include sufficient details to remain realistic and relevant. The latter flaw most often has arisen from models using rigid body assumptions, which considering the relevance of the discussed deformations is not representative of the in-flight behavior. Without including deformations one can therefore not study the aerodynamic performance of kites accurately, thereby also not efficiently develop designs that increase it.

The objective of this thesis will be towards the development of a fast structural model that can take into account the relevant macro-scale deformation modes of bending and twist. The model focus will be on accuracy, computational cost and modularity. The latter is key for the model its potential as a building block since it must be able to deal with other kites. The low computational cost requirements have led to a low-fidelity model scope. The V3 kite of Kitepower B.V. will be used as a research subject. The work will contribute to the scientific community by providing insights into the deformation phenomena and by developing a building block for a kite design tool. The latter will furthermore contribute to the airborne wind energy (AWE) community and hence towards the energy transition.

2

Literature review

This research deals with using modelling procedures to improve aerodynamic performance. Alternatively, one could determine the performance of the kite by physically producing it and testing it. This 'Darwinian process' as Breukels calls it, is the most common approach in surf-kite development today and is far from ideal [8]. One reason is that performance is generally assessed subjectively by professional athletes, most likely due to a lack of quality measurement instruments. Another reason is that producing and testing a kite is a time and resource-intensive endeavour, i.e. surf-kite designers need about a month per design iteration [35]. Therefore, one can't use design optimization procedures, which are generally considered ideal for finding an optimal shape.

Modelling the kite gives one the possibility of assessing the performance without flying it. This drastically decreases the time needed for an iteration, making design optimisation iterations viable for fast models. Design models generally achieve the required low computational cost by reducing the overall complexity. Robin van de Putte, the founder of a relatively new player in the surf-kite industry called Vantage (`https://www.vantagekites.com/`), identified this modelling procedure as necessary and highly beneficial.

Developing a LEI kite model is a complex task, especially when one wants to assess its performance. One reason is that it does not only require a model of the kite but also a simulation framework. Developing such a framework is difficult partly due to it relying on flight condition measurements for an accurate real-world representation and partly due to the deformations. Increasing aerodynamic performance could for a surf-kite producer like Vantage lead to more sales and for an operating AWES, it could lead to higher power output.

Deformations are considered the key factor for making modelling soft wing membrane kites, like the V3, so difficult (see Sec. 2.1 and 2.2). The best insights into the physical behaviour are currently found from studying experimental data rather than through modelling alone (see Sec. 2.3). The relevant research opportunities found in the gaps of the literature are addressed as research questions (see Sec. 2.4).

2.1. Deformations

A kite will only fly if the lift is greater than its weight. AWES LEI kites are, therefore, designed to have a high lift-to-weight ratio enabling operation at low wind speeds. Using little material comes at the cost of low structural strength, hence the flexible nature of LEI kites. Most of the structural strength a LEI kite has, comes from the pressure distribution in the canopy resisted by the tensile force in the connecting bridle lines. Due to its flexible nature, the kite deforms during operation, e.g. the body shows clear deformation during a turn (see Fig. 2.1c). Modelling deformation is considered highly important because the deformation itself is what allows the kite to turn according to Breukels's widely accepted turning theory [8]. It states that an asymmetric steering input leads to asymmetric deformation. This asymmetric deformation creates an arm for the aerodynamic forces generated on the outer section of the kite, which combined provide the moment that turns the kite. One might expect the rear tip

to counteract the moment, but due to the deformation, the inflow angle is less optimal meaning less force is produced. Another observed effect contributing to turning is the rolling motion of the kite. Both the twisting and rolling motion happen simultaneously and their effects are hard to separate. Bosch amongst others has validated the described turning behaviour of Breukels in simulations [5].

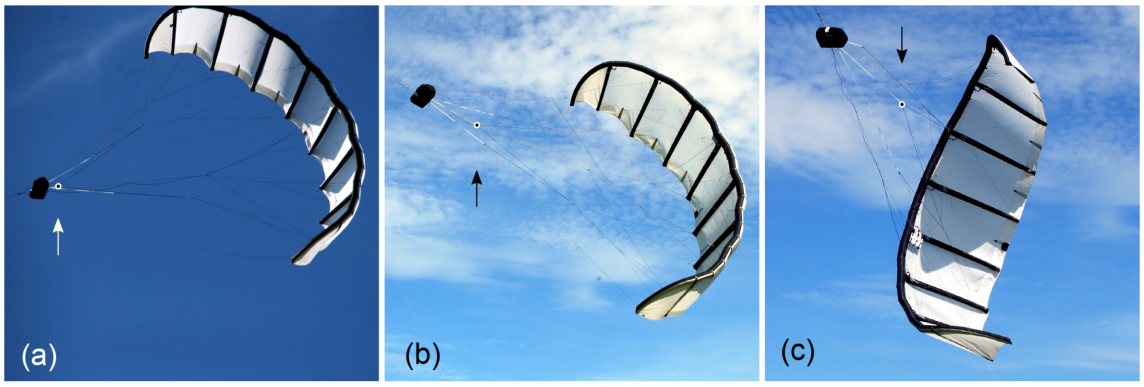

Figure 2.1: Deformation of the V3 LEI kite, with the arrow indicating the position of pulley that controls the amount of depower. Figure (a) shows a powered kite during the reel-out phase, (b) a depowered kite and (c) demonstrates the asymmetric deformation during a turn [47].

The difference in kite shape during the reel-out phase where it is 'powered' and during the reel-in phase in which it is 'depowered' is another form of deformation (see Fig. 2.1a and 2.1b) . In the powered mode, the kite is flatter and the canopy billows more compared to the depowered mode where the shape is more arc-like and less billowing is present. The kite has a different lift-to-drag ratio in both modes, which is key for the pumping cycle operation's efficiency because during the retraction phase one wants to spend as little energy as possible.

Bosch states that due to the sensitivity of the aerodynamic forces the change of external force upon deformation is substantial [7]. For the North Rhino $16\,\mathrm{m}^2$ kite Bosch found a 24% change in tip-to-tip distance upon comparing the maximum and minimum deformation [7]. The change in width is caused by a change in anhedral angle affecting many parameters like the projected surface area that affect the aerodynamic load [47]. That aeroelastic deformation changes the aerodynamic performance has been demonstrated from analyzing experimental data (see Sec. 2.3) [33, 51, 68].

The most pronounced differences are found between the reel-in and reel-out phases and during turning. During a steering manoeuvre, the lift-to-drag ratio is reduced as a result of the additional drag component induced by the tip's side force [23, 47]. Roullier found an average reduction of 5% in lift-to-drag ratio during a turn for the V3 kite [53]. The differences between the reel-in and reel-out phases are so pronounced that separate lift-to-drag ratios are used in models that exclude deformation [57, 68]. As Oehler et al. put it: "only after understanding the influence of kite shape and deformation its design can be optimized for aerodynamic performance" [48]. The importance and relevance of modelling deformation become clear from an example case. Suppose one would be able to predict which aspects of the kite affect the required steering input for a certain turn rate one could design for lower steering needs using this information. Lower steering needs would mean one could use a smaller KCU resulting in less system weight, i.e. higher efficiency and larger operational bandwidth.

2.1.1. Vibrations

Besides actuation induced deformations, there are other deformations that occur due to vibrations. Leuthold split up the frequency modes, making a distinction between larger-scale and sub-scale deformations (see Fig. 2.2).

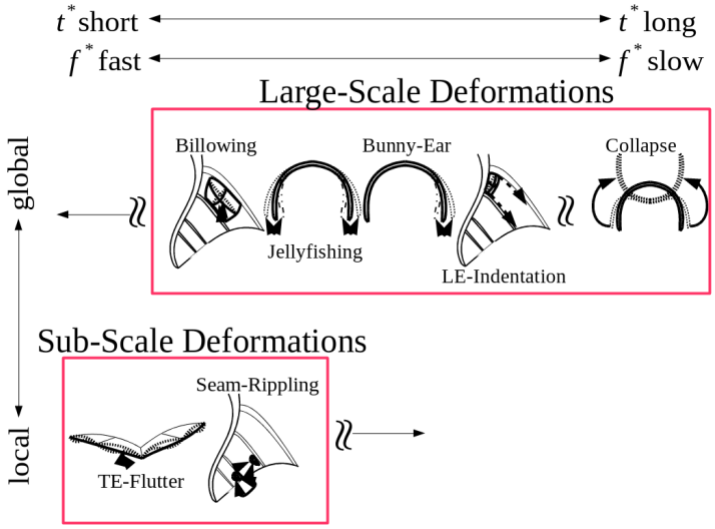

Figure 2.2: LEI kite deformation modes ranked on time-scale [40].

Relating the deformation modes to operation manoeuvres, one finds that the bunny-ear flapping mode is the same deformation as used for turning and the collapse deformation mode the same as used for changing the power setting. The latter is achieved by span-wise bending and the resulting change in anhedral angle is considered the main contribution enabling one to differ the lift-to-drag ratio settings. Operational manoeuvres are inferred by the actuation input, which changes the bridle line system layout. An example of a deformation mode that is not actuation induced, is TE fluttering. Vortex shedding from the TE of the canopy membrane causes the TE to flutter, which results in a local oscillatory motion with relatively high-frequency [40].

For a complete picture of the frequency modes, one should also consider the following flight path frequencies: figures of eight (f_8), general flight dynamics (f_{FD}) and typical characteristic aerodynamic frequency (f_a). Leuthold estimated a frequency band for the deformation modes and flight path frequencies, which were then visualized using a frequency spectrum (see Fig. 2.3). The identified deformation modes are: trailing edge fluttering (f_{TEF}), seam-rippling (f_{SR}), canopy buckling (f_{CB}), jelly-fishing (f_{JF}), bunny-ear (f_{BE}), leading-edge indentation (f_{IDM}) and collapse ($f_{Collapse}$).

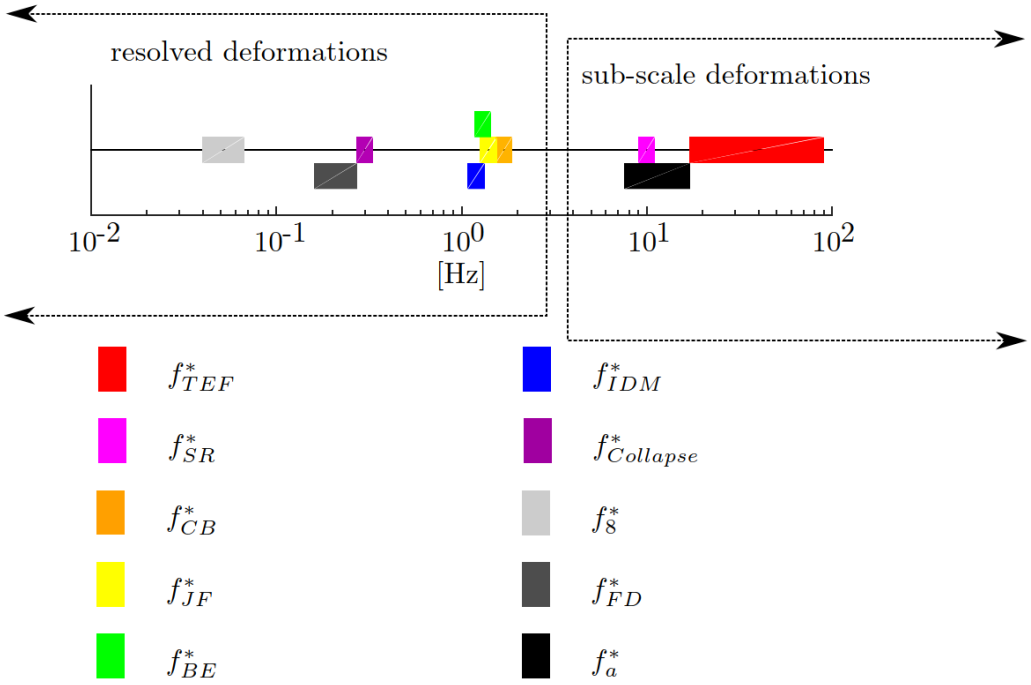

Figure 2.3: The rainbow-colors show the deformation mode frequencies where as the grey-tones show the flight-path frequencies. When estimating the frequencies from flight data, 10% extra was added on both sides of the spectrum [40].

When the goal is to dynamically simulate the precise shape of the kite, all the deformation modes are relevant. In practice, it is possible to neglect some while still getting accurate results. Why this is possible is best explained by thinking about the aerodynamic load. A deformation mode causes a shape alteration, which changes the aerodynamic load. If this change is present for a substantial time duration, the effects can't be neglected. However, if the modes are periodic and occur for a small duration they can be neglected [8]. Because the higher-order TE canopy vibrations occur periodically and are dominated by the lower frequency modes, their effects can be neglected [70]. Compared to the TE, the rest of the canopy is subject to higher tension loads. Higher tension loads, lead to lower frequency vibration modes. Neglecting sub-scale deformations for the rest of the canopy is, therefore, deemed valid [40].

Neglecting the sub-scale frequencies one finds a reduced-order frequency range, which for a quasi-steady flow assumption holds [40]. Van Kappel neglected the sub-scale frequency modes, therefore, decided to use a quasi-steady flow assumption [35]. Van Kappel's model showed reasonable results compared to experiments, thereby providing evidence for the validity of the quasi-steady state assumption. Within the aeroelasticity domain, one can have a static, quasi-steady or dynamic model. The quasi-steady model is generally assumed valid when the inertial forces are small compared to the aerodynamic and elastic forces, which for the V3 kite holds [53]. Furthermore, assuming a quasi-steady state is useful because it reduces the computational cost needs [5].

2.1.2. Fluid-structure interaction

The occurring deformations of the kite during flight are caused by the fluid interacting with the kite structure. This effect can be modelled using fluid-structure interaction (FSI) models. FSI models must be solved numerically and often an aeroelastic solver is used. FSI models can be subdivided into partitioned and monolithic solvers. The difference lies in that with a partitioned solver one formulates the aerodynamic and structural model separately. Partitioned solvers are used more frequently because they allow the use of already existing structural and aerodynamic models.

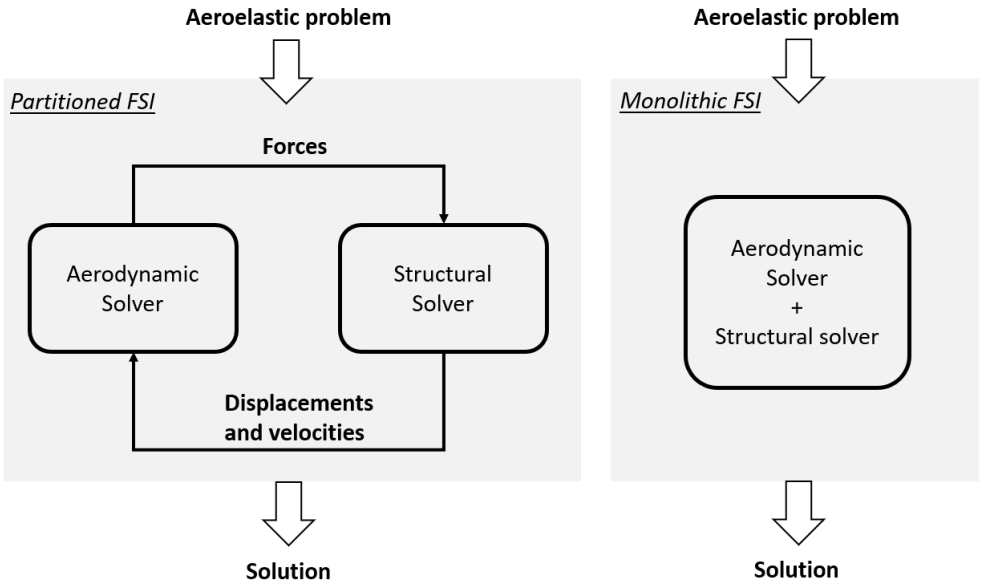

Figure 2.4: Altered visualization of the FSI model types their conceptual differences [40].

There are one way and two way coupled partitioned solvers. In a two way coupled partitioned solver, iterations occur between a structural model that calculates the shape deformations based on the exerted forces and an aerodynamic model that calculates the aerodynamic forces based on the shape. Because the mesh is prone to change throughout the iteration, the aerodynamic and structural mesh must be coupled and formulated dynamically [49]. Partitioned solver models can either be strongly coupled or loosely coupled. Loosely coupled FSI models are more efficient, but also more prone to numerical instability [73]. Strongly coupled models are more robust but require higher computational costs.

In 2020 Folkersma et al. build a two way coupled partitioned aeroelastic solver to model the deformation of another type of soft wing membrane kite, called a ram-air kite [25]. Nobody has been successful in setting up an accurate FSI model for the LEI kite, however, due to its complexity and computational cost. To illustrate this point, some example studies will be discussed. Schwoll devoted a master (MSc) thesis to develop only a structural model using a finite element (FE) approach with commercial software. The complexity was of such level, that within a year of research not all phenomena of interest could be modelled [62]. Lebesque devoted a MSc thesis to set up only an aerodynamic model for the V3 [38]. The run-time of Lebesque's computational fluid dynamics (CFD) model was in the order of hours. Because iterations are needed, this makes using CFD in FSI too computationally expensive. Another reason why FSI modelling of LEI kites using CFD and FE is difficult is the attachment between the LE and canopy. This attachment results in a sharp corner in the CFD mesh, which makes the problem numerically unsolvable. Van Kappel worked around this problem in the aerodynamic analysis, by assuming it to be a corner of finite radius [35]. This solution does however not work in LEI FSI models, because a dynamic mesh formulation is required. An alternative modelling solution is to attach the canopy to the middle of the LE, as Bosch et al. did. This, however, results in overestimating the lift-to-drag ratio [6].

Geschiere extended Bosch his partitioned two way coupled FSI model using an adaptation of the work of Fechner et al. by including bridles and an extendible tether [21, 27]. An extendible tether was chosen because modelling a tether of varying length allows for power production prediction. Due to the differences in the complexity of the modelled AWES components, Geschiere decided to use different models and couple their outputs (see Fig. 2.5). By not modelling each component with the same level of detail, a reduction in computational cost was achieved. Geschiere's dynamic bridle model is coupled to the FSI kite model through the bridle constraint points. For stability, it was found best to include 0.3 m of bridle length into the FSI kite model. When comparing the modelled V3 kite with experimental data,

it was found that with the current aerodynamic model artificial damping is needed for a stable solution. Artificial damping is considered the main factor causing the underestimation of the turning rate of the kite.

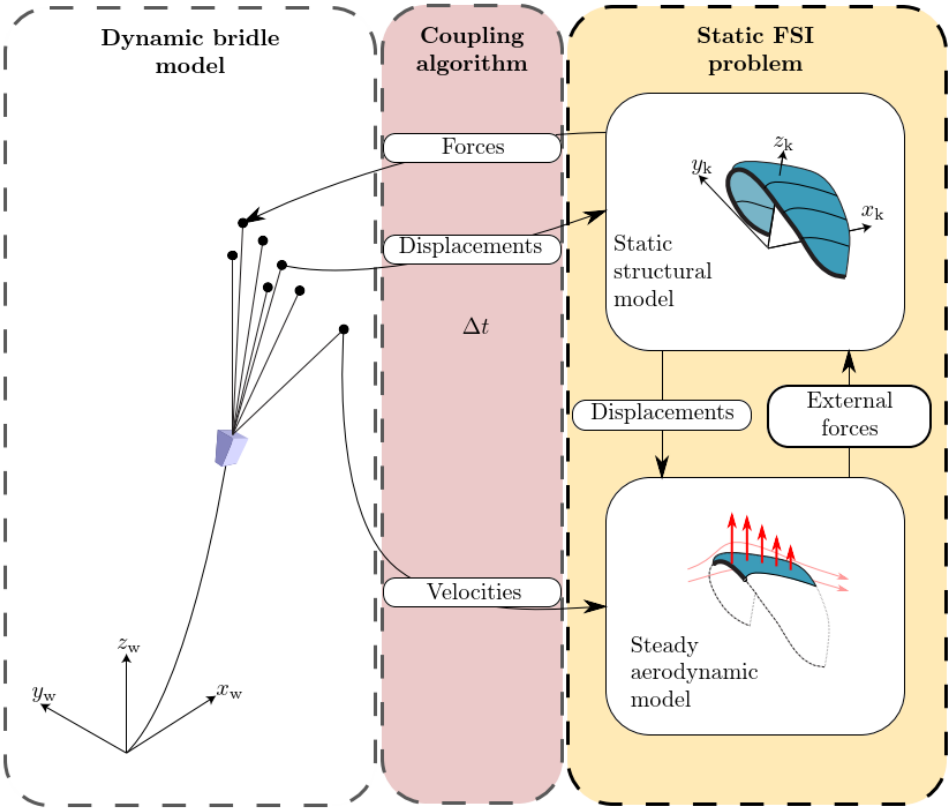

Figure 2.5: Geschiere's approach to model the V3, by coupling a dynamic particle system to a static FSI model [27].

Concluding, it is observed that a deformation model is needed to model LEI kites. A partitioned FSI model based on computational fluid dynamics (CFD) and FE is not a viable option due to its high computational cost. Besides too long run times, a mesh is required for both CFD and FE methods. Formulating a dynamic mesh for the complex shape of a LEI kite is a time- and resource-intensive procedure which makes assessing new shapes fast difficult, if not infeasible. Because accuracy and computational cost are inherently a trade-off, a less accurate but faster structural and aerodynamic model are needed. Furthermore, as Geschiere's model illustrates, besides the kite model the tether and bridle lines must also be included and formulated separately, to be able to simulate a pumping cycle operation [27].

2.2. Structural models

Structural models use material properties and forces as inputs to calculate the deformations of a body. In this section, several developed structural LEI kite models will be discussed (see Fig. 2.6), which are ranked based on computational cost and included degrees of freedom (DOF).

Black box models use experimental data to find relations between variables. This has the advantage of being able to model the behaviour of the kite as was experienced during the experiment. Noom developed a fast analytical quasi-steady model and modelled the kite as a single point ignoring inertia and deformation [45]. By introducing some mass and dropping the quasi-steady state one arrives at the point mass model. Diehl developed a point mass model in 2001, which according to Ruppert formed the basis for many studies performed since then [15, 54]. When representing the kite as a finite number of points more DOF are taken into account and these models are called particle system models. In

particle system models all points have a mass and the connections have some internal forces. A rigid body model assumes the kite to be a solid which does not deform. The main difference with the point mass and particle system models is that it incorporates an orientation allowing it to deal with attitude dynamics [54]. Attitude is referring to the heading of the kite and is a term often used when describing an aircraft flight path.

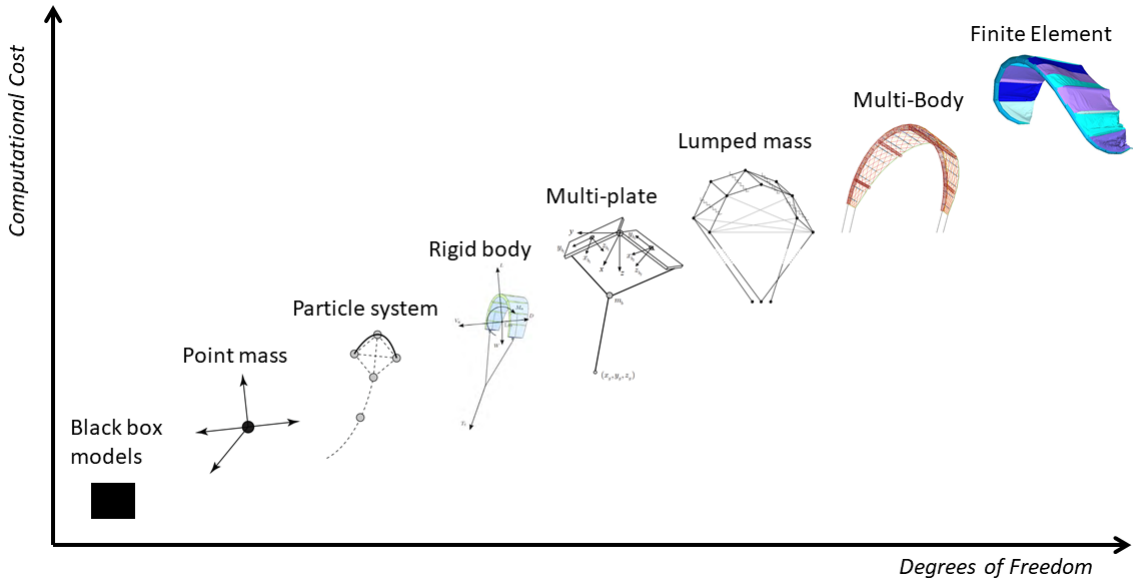

Figure 2.6: Currently available structural kite models adapted from [6, 8, 26, 54, 72].

Williams et al. as well as van Til et al. developed multi-plate models to incorporate deformations [67, 71]. In both models, a finite number of rigid plates is used which are connected with joints that are providing the necessary degrees of freedom (DOF). Furey extended the multi-plate model towards a lumped mass model. He used point masses connected with constraints to simulate the kite [26]. Breukels developed a multi-body model and the reason for doing so was to be able to model the deformation occurring due to the flexibility without needing FE methods [8]. The multi-body model is based on multi-body dynamics that connect rigid bodies with springs, dampers and hinges. The models that incorporate FE methods are those that can achieve the highest accuracy. Bosch et al. developed a FSI model that used FE method and Breukels his aerodynamic model [6].

Experimental data is needed for black-box models they, therefore, can't be used for a design model that assesses new shapes [13]. Because deformations are deemed essential for a design model the current: point mass model, particle system and rigid-body model all are not feasible options. The lumped-mass model has problems with numerical instability due to the presence of large forces acting on small masses [54]. This numerical instability is resolved by using a small time step, which unfortunately leads to high computational cost. The multi-body approach of Breukels is about 20 to 30 times slower than real-time, i.e. too computational expensive [8]. Furthermore, according to Bosch, the model does not include the real flexibility of the kite by not modelling the axial strains. On top of that, the parameters used require fitting procedures, making using them for design purposes difficult. FE methods are too computationally expensive for iterative design procedures, e.g. Bosch et al. reports run-times of 27.5 slower than real-time [6]. The best available option is, therefore, the multi-plate model.

2.2.1. Multi-plate model

The multi-plate model of Williams et al. is a flexible kite model designed to study the dynamics and control of a kite [72]. Each section determines its forces and moments using plate aerodynamics. To do so, the plate model is completely flexible about its center line for both torsional and bending mode deformations. Another DOF comes from the plates ability to hinge over the LE. In reality, this is not possible, because the plates could collide with one another. This is a non-issue according to Williams

et al. because the model is simply designed to be an abstract approximation. The connecting bridle lines are assumed straight. A constraint is set on that all plates must have the same yaw angle (see Fig. 2.7). The pitch, roll and yaw angles of the plates are determined by the bridle attachment points and the tensile and aerodynamic forces. The two-plate model (see Fig. 2.6) is easily extended to more plates as long as one uses an even number of plates.

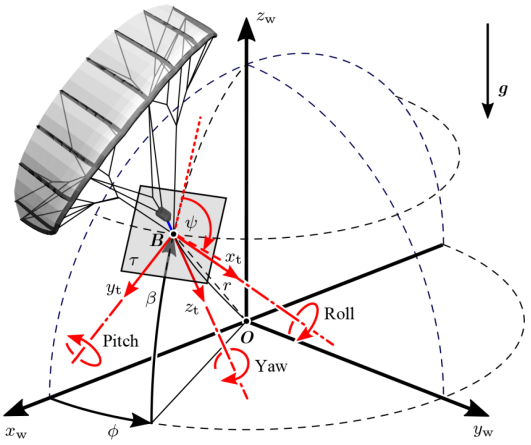

Figure 2.7: Overview of the orientation reference frame (x_w, y_w, z_w), yaw, pitch, roll, heading (ψ) and spherical coordinates (β, ϕ, r) [47].

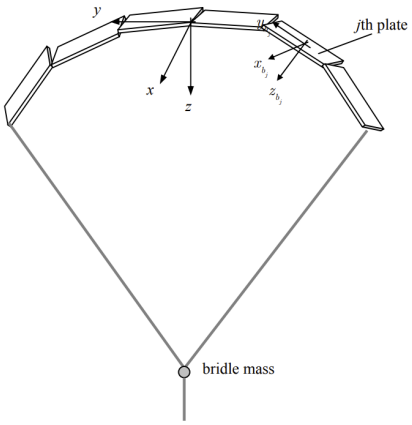

Figure 2.8: A multi-plate model with 6 plates [72].

Non-physical forces are needed for the hinges and springs with which the plates are attached. According to Deaves the inclusion of non-physical forces reduces the deformation prediction accuracy and only part of the flexibility is modelled [13]. Furthermore, according to Geschiere, the dynamics are not accurately modelled since the kite mass is modelled as a point mass, i.e. the bridle mass point (see Fig. 2.8) [27].

The multi-plate model developed by van Til et al. is designed for control purposes and runs almost real-time [67]. It is made from three plates, each connected with gimbal joints and it allows the two main deformation modes required for turning manoeuvres, i.e. spanwise bending and torsion. Van Til et al. argue that the existent non multi-plate models are either too computationally expensive, e.g. the model of Bosch et al., or do not model the phenomena accurately enough, e.g. Fechner et al.'s model [6, 23]. For future work, it is recommended to include more plates since that would improve the accuracy of the deformation modelling.

With a fast aerodynamic model and a fast accurate stable deformation model, the two way coupled FSI model has the potential to have low enough computational cost to be viable for design optimisation iterations. The existent deformation models are however not accurate, not stable or not fast enough and it is here where the author sees a possibility to contribute.

Considering the current aerodynamic models suffer from the same problems, it is likely that even with a fast accurate stable deformation model the computational cost of a two way coupled FSI model is still too large for iterative design procedures. An alternative solution for modelling the deformations could be to develop a novel one way coupled FSI model. Such a model would not require iterations nor dynamic mesh formulation, leading to less computational cost and lower lead times. The structural model needed would have to be able to calculate the shape without knowing the force output of the aerodynamic model. Another argument supporting this idea comes from the fact that both the kite material and the kites deformation modes are non-linear and modelling non-linear behaviour is complex thereby generally computationally expensive [27]. A one way coupled FSI LEI kite model has never been developed yet, because there has never been a deformation model that accurately predicts the shape without knowing the forces. Therefore, the author sees a possibility to contribute to the body of science by developing such a model.

2.3. Experimental data

Most of the previously discussed models do not use experimental data, which make them useful for design purposes but less when trying to accurately simulate the flight trajectory. Modelling difficulties arise due to deformations and their dependency on historical flight manoeuvres, which make it infeasible to use well-developed aircraft analysis techniques [7]. Most models that simulate the flight trajectory solve these issues by not modelling deformation.

Without knowing the operating conditions it is impossible to simulate in-flight behaviour accurately. To obtain operating conditions experiments are needed. Usually, for fixed-wings a wind tunnel experiment would be conducted, where a scale model would be used and flow characteristics would be made similar such that the same phenomena as during flight can be observed and studied. For soft wing membrane kites problems arise because the occurring FSI phenomena on a scale model are different [69]. Because they are different, it is hard to extrapolate information [47]. Wind tunnel tests are furthermore expensive, nonetheless, one has been done for the LEI kite plane of Breukels (see Fig. 2.9) [8].

Alternatively, one could perform experiments outside of the wind tunnel, which brings up difficulties with measuring and controlling the environment. Hummel et al. developed a tow test for measuring the dynamic properties of tethered membrane wings to eliminate some of these unknowns [33]. In the experiment and others: velocities, angles, forces and power settings were measured enabling aerodynamic identification procedures. Such procedures are deemed by Oehler and Schmehl as the most optimal way of obtaining aerodynamic coefficients [47]. The main reason is the inclusion of all effects, one of them being deformation effects. A non-exhaustive overview of the most relevant aerodynamic identification models will, therefore, be presented here.

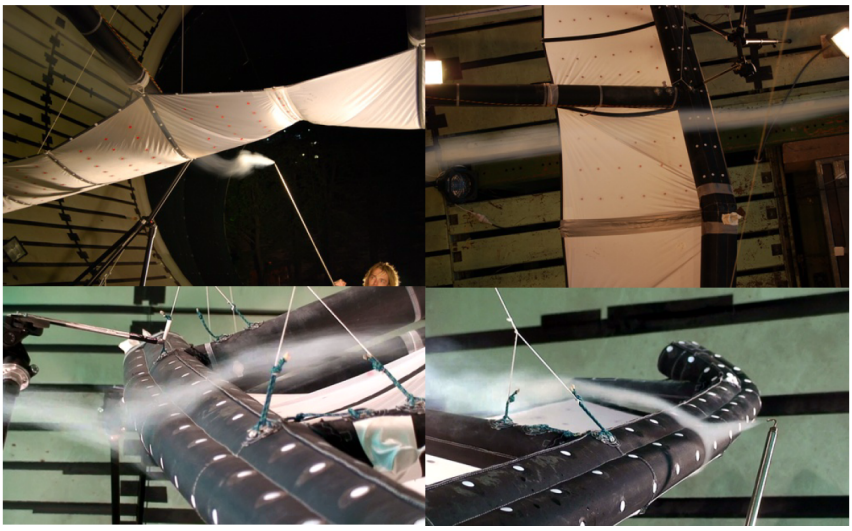

Figure 2.9: Kiteplane experiment showing the flow separation aft of the LE due to the recirculation region [8].

Van der Vlugt et al.

Van der Vlugt et al. developed a quasi-steady model (QSM) that can predict the power generation using a separate set of analytic equations for the traction, retraction and transition phase [69]. Two pumping cycles flown at different wind speeds were used for aerodynamic identification and validation. Small time scale dynamic processes, tether elasticity, variations of the aerodynamic properties within a phase and wind changes over time are all assumed negligible and not modelled. A framework with and without gravity was developed and the conclusion was drawn that including gravity is necessary to simulate the performance. Van der Vlugt et al. mention that wind measurements locally would improve identification efforts and that for studying dynamic flight behaviour a dynamic system model is needed.

Schelbergen and Schmehl performed a validation study of the QSM using experimental data with 87 pumping cycles [57]. They found that a drag coefficient correction is needed, which was partly attributed to not modelling crosswind manoeuvres. Furthermore, neglecting the vertical wind component

or assuming a straight non-slacking tether was found to cause substantial errors. The QSM under predicted the power production by -26.4%. From both studies, it can be concluded that for a performance model to make accurate predictions the simulation must include the effects of gravity, slacking tether, crosswind manoeuvres and vertical wind speeds.

Fechner et al.
Fechner et al. developed a real-time capable robust model that allows flight path optimisation and can fly a similar trajectory as during the experiments [21]. The model bases its aerodynamic coefficients on two-dimensional (2D) sail wing sections as a function of the angle of attack. Without rotational inertia, unphysical effects occur on the predicted yaw rate. Therefore, it was decided to build a four-point kite model (see Fig. 2.10) that parametrizes the shape of the kite by the width, height and distance to the KCU. Spring-damper systems are used for the connections between the four points to model the structural properties of a LEI kite. The springs were made so stiff that no flexibility of the kite is explicitly modelled, making this in essence a rigid body model. Not modelling deformations of the kite through upfront identified material properties, meant that experimental identification of the steering sensitivity parameters was needed. To clarify, steering sensitivity is the rate at which a kite turns when encountering an asymmetric steering input. The steering sensitivity can't be modelled without deformations, since a kite can't turn without deformations. The experimental identification was used to alter the kite width to make the modelled steering fit the measure steering behaviour, which resulted in less than 2% conversion error. This part of the work is revolutionary because even though he uses a rigid body model, changing the width of the kite model in steps simulates the real flexibility of the kite. By doing so the span-wise bending deformation mode is represented, which others had not been able to do while predicting the aerodynamic coefficients during flight.

To be able to validate the four-point model Fechner et al. coupled the model to a control system and a discretized particle tether model (see Fig. 2.11). Furthermore, Fechner et al. showed that the turn rate law derived for simulating turns of non-deforming body models holds for LEI kites [18, 19].

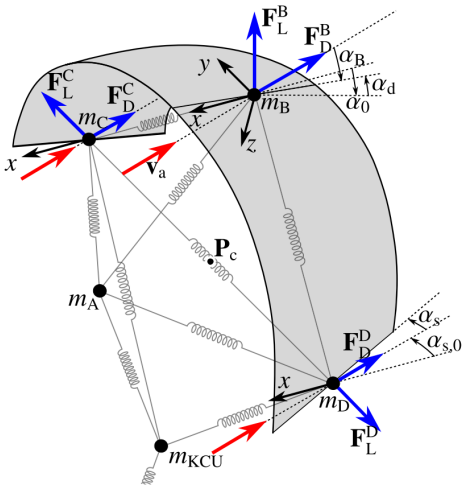

Figure 2.10: The 4-point model of Fechner et al. with the definition of the: depower angle (α_d) and the steering angle (α_s) use to steer the kite [23].

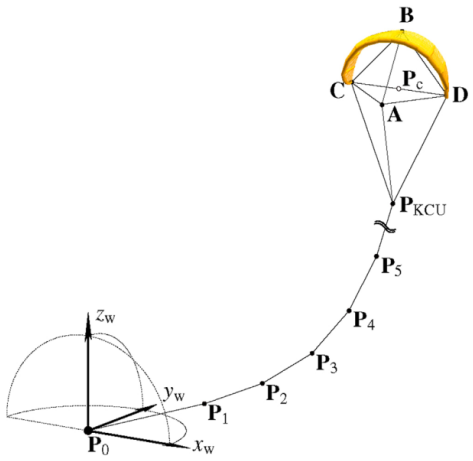

Figure 2.11: Discretized tether model connecting to the 4-point model [23].

Oehler and Schmehl
Oehler and Schmehl developed an aerodynamic characterization method for the V3 from which one can derive the aerodynamic characteristics accurately [47]. A novel experimental setup was developed, which as recommended by Hummet et al. included an in-flight wind measurement sensor [33]. The setup can measure larger-scale systems during operation. A self-aligning pitot tube is mounted in the plane of the power lines. This plane is chosen because the geometry stays relatively constant due to the lines staying straight, i.e. they only changed with 0.1° to 0.2° during the experiment. During flight the load distribution between the power and steering lines shifts when the angle of attack changes,

due to a tilting of the aerodynamic load vector [32, 48]. This effect is neglected because the bridle line force is not measured, instead, a constant distribution is assumed. The angle between the kite and the ground is called the elevation angle (β) and is often derived from the tether angle of attack measured at the ground [32]. Oehler and Schmehl however defined the elevation angle separately from the tether angle to the kite (see Fig. 2.7), which means that sagging does not have a direct impact on the measured lift-to-drag ratio.

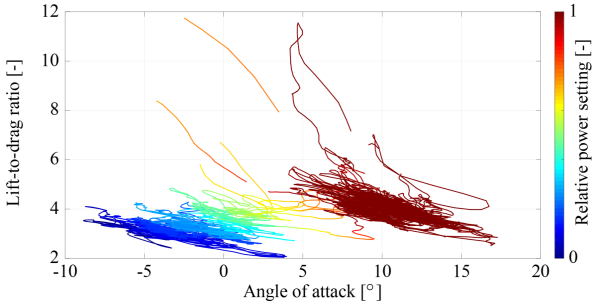

Figure 2.12: Lift-to-drag ratio vs the angle of attack with a colour coded relative power setting [47].

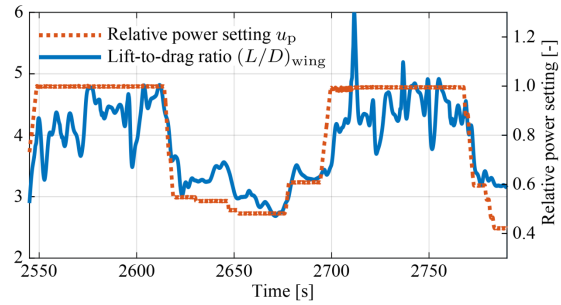

Figure 2.13: Relation between the relative power setting (u_p) and the lift-to-drag ratio [47].

A quasi-steady flight is assumed and smoothing was, therefore, applied to remove sub-scale processes. It was shown that the aerodynamic characteristic time scale of the V3 is an order of magnitude smaller than the turning timescale, which is a positive indication of the validity of the used quasi-steady flight assumption. The lift-to-drag ratio was related to the relative power setting instead of only to the angle of attack, which increased the accuracy compared to the models of Fechner et al. and Ruppert, who reported needing major adjustment to fit the trajectories [21, 54].

Roullier

Roullier [53] used experimental data of the V3 to perform an analysis on the effects of the KCU, the relation between model complexity, aerodynamic parameter identifications and more. Roullier found that the KCU drag and inertial effects are substantial. Furthermore, the KCU swings because of the inability of the tether to resist bending, the effort required to compensate for the effects are, however, only 1% to 2% of the lift. Roullier developed a more complex model than Oehler et al. did, by including additional orientation angle and the contributions of weight, drag and inertia [47]. This was partly achieved by using a three-plate model. Each plate has an aerodynamic centre that generates lift and drag, which are defined as functions of the: angle of attack, power input and steering input. Roullier compared his three-plate model results, to Oehler et al.'s model and the work of Demkowicz who performed rigid wing CFD analysis (see Fig. 2.14 and 2.15) [14, 47]. The lift coefficient (C_L) predictions of Roullier and Oehler et al. were in good agreement whereas the drag coefficient (C_D) was less so, which is attributed to the added inclusion of pitch and roll. Differences with respect to the CFD results are present for both slope and magnitude and arise due to not taking into account deformations of the kite. These differences are most pronounced in the drag polar, which is caused by not modelling the frontal area increase and with it the increase in drag. Roullier tried to model turning using the moment caused by the difference in force creation of the side plates. This force was however found not sufficient, therefore, turning was modelled using a turning rate law.

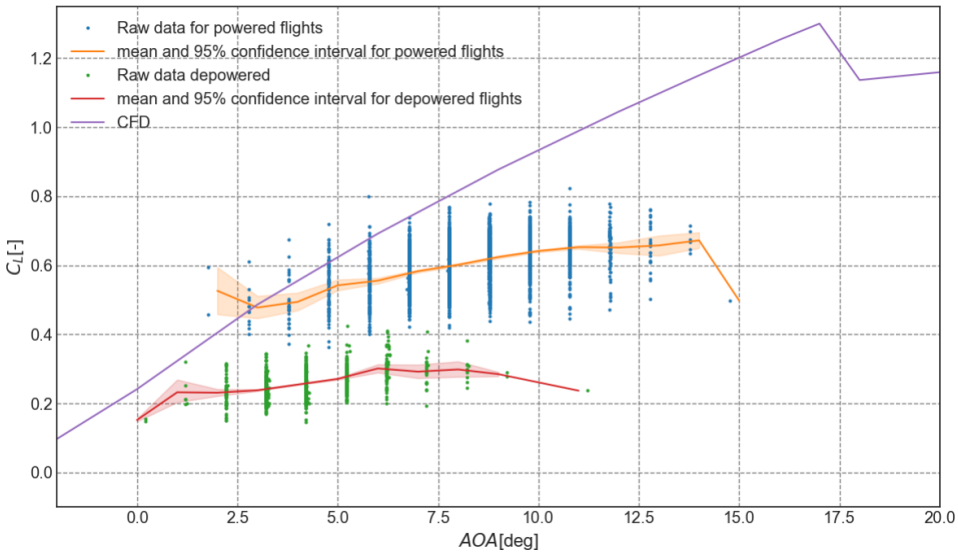

Figure 2.14: C_L plotted against the angle of attack (AOA). Where the experimental values of the powered and depowered mode are compared against CFD results [53].

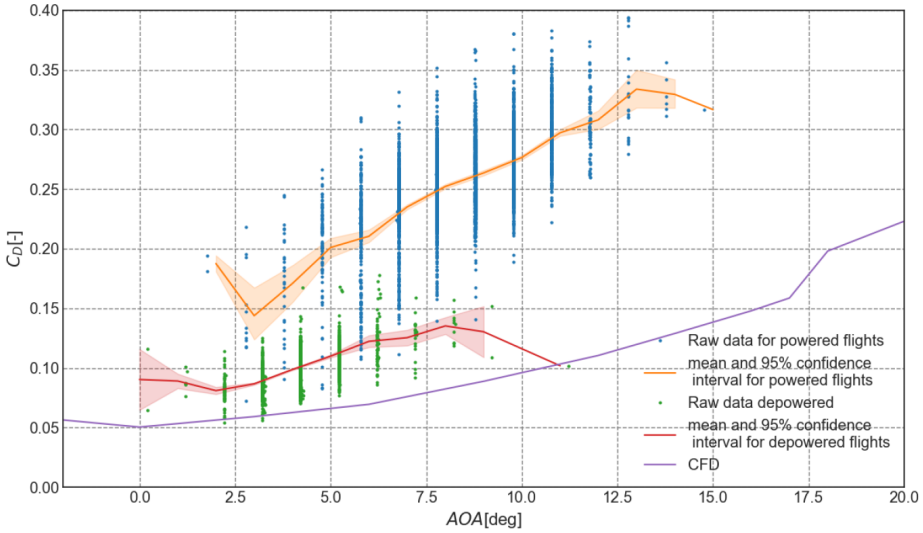

Figure 2.15: C_D plotted against the angle of attack (AOA). Where the experimental values of the powered and depowered mode are compared against CFD results [53].

2.4. Research questions

This literature review covered an exploration of relevant structural modelling approaches of a soft-wing membrane kite, in particular the V3. It was decided that developing a model that could be used in iterative procedures would be ideal, because it could enable kite designers to increase their aerodynamic performance. The design model itself would, besides the fast structural model, consists of a fast aerodynamic model, a FSI coupling algorithm and a simulation framework. The focus of this research is towards the development of a structural model. Due to the low computational cost requirement, a high fidelity model will not be developed.

Deformation modelling was found essential, to accurately model the aerodynamics and the in flight behaviour. Most current structural LEI models do not include deformations and those that do, have too high computational costs to be useful for iterative design purposes. According to the reviewed literature, a model that predicts deformation without force input has never been developed. Such a model would drastically reduce computational cost by alleviating the necessity of iterations between the aerodynamic

and structural model. The author, therefore, sees potential to contribute to the scientific community by developing a structural model that does not need a force input. Another option, is a faster yet stable and accurate structural model. The work of Geschiere is considered the current state of the art, since the model was able to take into account deformations by using a spring representation of the bridle line system [27]. The multi-plate models are also considered, due to their ability of representing the shape deformation for low computational cost.

Several discussions with other airborne-wind energy researchers, this literature review and with it the identified gaps in the scientific body of knowledge has let to the following research objective:

> *Assess the aeroelastic deformation effects on a soft wing membrane kite by developing a fast structural model.*

Based on the research objective and literature review, several research questions came up each with their own sub questions.

I *Can a fast deformation model be developed that could be used in a FSI module of a design tool?*

- Is formulating a geometric model possible?
- Can the model predict both symmetric bending and asymmetric twist?
- Can the model run real-time?
- Does including empirical relations increase model accuracy?

II *Can one perform a photogrammetry analysis of the V3 during flight using footage shot from the KCU?*

- Can both straight and turning flight be analyzed?
- Can one extract empirical ballooning relations?

3

Research approach

The literature was reviewed, scientific gaps were identified and research questions were formulated (see Ch. 2). The main body of the rest of the research can be divided into three parts.

The first part is focused on data acquisition (see Ch. 4). Experimental data, empirical relations and the best representation of the flown version during the analyzed measured campaign are extracted. The latter comes in the form of geometry specifications of the V3 kite wing and its accompanying bridle line system. The data acquisition efforts form the first building block of the research, by providing the input data (see Fig. 3.1).

The second part covers the development of a representation of the kite wing (see Ch. 5). Using insights from literature, kite designers, experimental experiences and common engineering knowledge a novel wireframe representation of the V3 was developed in Python (see Fig. 3.1) [50]. Python is selected as the programming language because it enables the possibility of open-sourcing the solution and it is an efficient code enabling low computational costs [67]. The author has, furthermore, several years of experience using Python, using it will therefore accelerate the research process.

The third part governs the bridle line system, due to the key role it plays in determining the shape deformations (see Ch. 6). Three different algorithms were developed and coupled to wing models (see Fig. 3.1).

With all the components in place, the results can be analyzed and compared (see Ch. 7). The comparison serves to verify and validate the developed models, thereby indicating the accuracy of the developed models. Based on the accuracy, modularity and computational cost the best models will be selected. This step forms the last block and the research output. Based on these results, conclusions will be made and recommendations for future research can be provided (see Sec. 8.1 and 8.2).

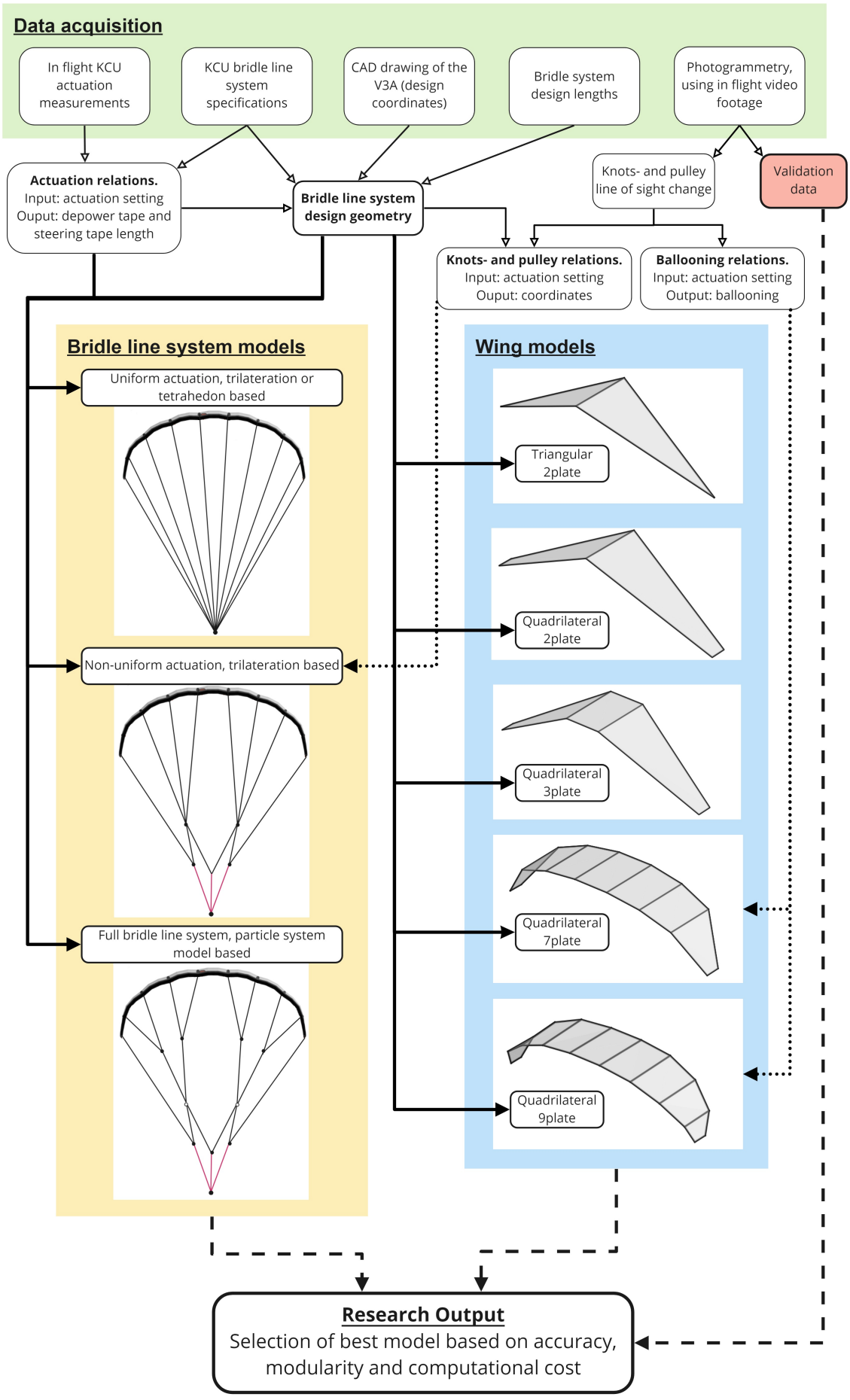

Figure 3.1: Research workflow.

4

Data acquisition

To develop the desired models, data is needed. Kitepower B.V. has provided experimental data containing both footage and measurements as well as several answers to specific geometric layout questions. The experimental data can be used to verify whether deformation is indeed the key to closing the gap between the experiments and simulations. The experimental data is from tests done in 2017, the period in which the V3 was called the V3.A. Having both measurements and footage of the same flight would allow one to assess relationships between measured variables and the deforming shape for each time step. From analyzing the footage, it was observed that no measurement rack was present, the conclusion was therefore made that the measurement and footage were obtained during different flights. Therefore, the deformation needed to be determined using only the footage. Achieved by using a one camera-based photogrammetry analysis. One camera-based photogrammetry is possible because distances to certain objects are known upfront [34]. The photogrammetry procedures are explained in detail in section 4.1.

The V3 is Kitepower B.V.'s 'workhorse' kite and its bridle line system layout has been continuously subject to change to improve its performance. The changes were mainly done during experimental campaigns in the field, leaving one with many undefined parameters. For the validation to be useful, it is key to obtain the closest approximation of the bridle line system that the V3.A kite was flying with during the experiments in 2017. This is in part because the developed bridle line system models operate using geometrical input, i.e. bridle line length changes (see Ch. 6).

Besides uncertainties in the bridle line system, there are also uncertainties regarding the precise kite wing shape. These are partly caused by the differences between drawings send to the kite manufacturer and the physical kite wing that one receives back [5]. Measuring the shape in hindsight is not trivial either because the unloaded geometry is subject to change due to the high flexibility [5]. Therefore, one would ideally measure the shape in flight to ensure the same design is analyzed as is flown [38]. Experimental efforts that use inertial measurements units for this purpose have recently been developed, but not yet fully worked out nor tested on an AWES [34]. The specifications of the design geometry of the V3 kite are relevant for the AWE field because the kite has the potential to serve as a benchmark model. The V3 could serve as a benchmark model, because Kitepower B.V. no longer restricts data access of the V3 to protect IP. Another reason is the relatively large, i.e. relative considering that the AWE research field is a novel, body of research that has been done on the V3 which enables the use of previously determined relationships and values. The steps and assumptions leading to a specification of the design geometry of the V3 kite are presented in section 4.2.

4.1. Photogrammetry

On the 24th and the 30th of March 2017, Kitepower B.V. performed experiments with the V3.A kite at Valkenburg Airport in the Netherlands. Several of these flights were filmed by attaching a camera to the KCU (see Fig. 4.1). This footage will be used to track how the width and the amount of TE ballooning change during flight. The models will predict the width change based on the bridle line attachment

points. Therefore, the distance between the bridle line attachment points at the tip will be determined instead of the kite width. In the remainder of the report, width should be interpreted as the width between the bridle line attachment points at the tip. The width is chosen as a parameter to compare the experiments and simulations, because it represents a global measure of the anhedral change. The anhedral angle is important because it has a direct effect on the generated force by altering several aerodynamic parameters, one of them being the projected surface area. Ballooning is studied experimentally because it scales with aerodynamic force and the development of an accurate aerodynamic model does not fall within the identified aim of this research. It will, however, be considered because the expectation is that the combination of local changes in TE strut distance affects the global shape of the kite.

Since no measurements of the same flight are present, it is difficult to couple the measured parameters to certain states of the kite, e.g. the obtained deformation can't be formulated as a function of the wind speed. A solution was found by identifying extreme states and linearizing the behavior in between the states.

Figure 4.1: Video still from the KCU of the V3 during a launch on the 24th of March 2017 [1].

For straight flight, the maximum and minimum powered state, also called depowered state, will be identified. The powered state occurs in the reel-out phase, whereas the depowered state occurs in the reel-in phase. In straight flight, a symmetrical deformation is assumed, with its symmetry line lying parallel to the struts crossing the middle canopy piece. Furthermore, the powered state is chosen because it corresponds to the kite its reported computer-aided design (CAD) design (see Sec. 4.2). The only difference is that the CAD displays no ballooning. B. van Ostheim, who is the kite designer for Kitepower B.V., confirmed that the kite is designed such that with ballooning in powered flight the tubular frame has the same orientation as the CAD shape, i.e. the tubes are aligned in the same direction and under the same angle with respect to one another. In other words; the distance between the TE tips of the struts is not that of a fully stretched canopy, but rather the distance designed for the expected ballooning during powered flight.

For turning flight, three states are identified: the apex of a powered left turn, the apex of a powered right turn and straight powered flight. All these states occur during the reel-out phase, as the ideal flight path contains no turning maneuvers during the reel-in phase (see Fig. 1.4).

4.1.1. Analysis setup

Two videos, one from each measurement day were selected of sufficient quality to be used for the photogrammetry. From each video, for each state, several time stamps were identified that corresponded best to the respective description. The sampling type is non-probability purposive full sampling be-

cause each sample is selected based on knowledge of the desired sample. The sampling selection is made using visual and audible input. The velocity is visually assessed by comparing the respective surrounding velocity. Other input was obtained from estimating the position of the kite within the known ideal flight path and for turning by studying the full movement and estimating the middle point within that movement. The audible input was useful to identify the amount of loading, because the noise scales with velocity, which in turn scales with the amount of loading.

From each selected time stamp a video still was extracted. Before one can extract the desired lengths out of the resulting images one must deal with the distortion of these images. The camera uses a wide-angle lens creating a so called 'fisheye' effect that distorts the image. A software called GIMP is used since it allows one to manually remove the distortion by adding an opposite 'lens distortion' [30]. This procedure is done under the assumption that a straight horizon corresponds to an image without camera-induced distortion. A main distortion setting of -25% and an edge distortion setting of -10% was needed to straighten the horizon.

The video footage images appear in perspective view. Perspective view is how one normally sees the world, i.e. objects further away appear smaller than they are. For taking three-dimensional (3D) measurements out of a 2D collection of images this is a problem. To resolve this issue, one must transform the image to an orthographic view or correct the extracted lengths based on their distance to the camera. The latter approach is used by comparing the relative change in line-of-sight and angle in comparison to the powered state in straight flight. The powered state in straight flight is used as the baseline because it corresponds to the design state. The changes are caused by the KCU swing, kite pitching motion and the deformation of the kite.

Figure 4.2: KCU swing demonstration of an $25\,\mathrm{m}^2$ LEI kite during flight on the 24th of November 2010. It was filmed from a camera attached to the KCU, which at the time was located lower down the tether [22]. The left image shows the KCU swinging to the right during a turn. Upon comparison of the middle and right image, a 'vertical' difference is noticed, also indicating a KCU swing.

KCU swing

With KCU swing, the change of position of the KCU with respect to the kite is meant (see Fig. 4.2). This swing is caused partly by the relatively large mass of the KCU that carries momentum. The KCU swing differs between turning and straight flight, its effect is so large, it even induces a roll effect on the kite [53]. In the powered and depowered state, the distribution of forces between the LE and TE shifts, due to a chord-wise tilting of the lift vector [47]. This is another contribution towards the KCU swing. A comparable effect is found between turning and straight flight, but now in the span-wise direction. The span-wise tilting causes the bridle line system to be asymmetrically loaded, which induces the KCU swing effects. All of the discussed types of KCU swings cause changes in the line-of-sight and angle at which the kite is observed, which due to the perspective view must be taken into account.

Interesting to notice is the relative inward folding movement of the tip when the kite is depowered (see Fig. 4.3). This effect will be further discussed in chapter 6. A quick qualitative assessment between

powered and depowered reveals an inwards motion of the pulley points, an outward motion of the knots and two slacking bridles on each side of the depowered wing. The knot and pulley positional changes will be measured by drawing an imaginary line from the KCU through the points. This imaginary line crosses the canopy of the kite wing at the TE and this location will be used as calculation input for a particular bridle line system model (see Sec. 6.2.3).

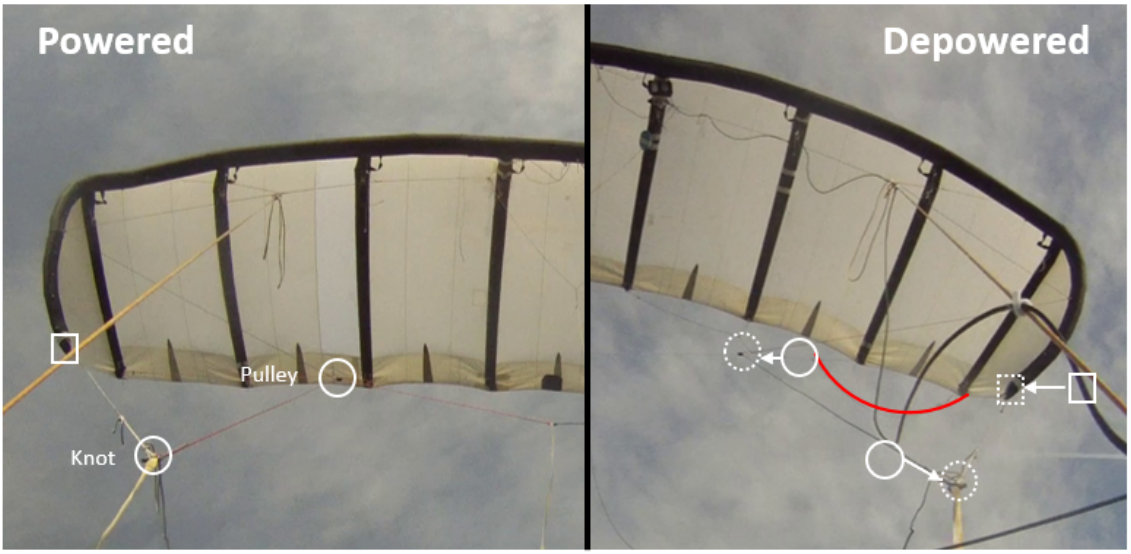

Figure 4.3: Video stills indicating the height difference of the kite within the image frame [1]. The pulley point, knot point and kite bridle tip movements from powered to the depowered state are identified. Furthermore, the red line indicates the present slacking bridle in the depowered state.

Kite pitching

The pitching of the kite is controlled by changing the power setting (u_p). The power setting is found constant during the reel-in and reel-out phases. The same observation was made by Oehler and Schmehl, who studied other measurement data of the V3 [47]. The angle of the chord-wise direction of the kite with respect to the KCU will change, as an effect of the pitching. For elements roughly perpendicular to the change in angle, e.g. the TE of the middle plate, this mainly causes a general increase in the length of the line-of-sight. For elements parallel to the angle, however, e.g. the struts, this causes both a varying change in the line-of-sight length as well as in observed object size.

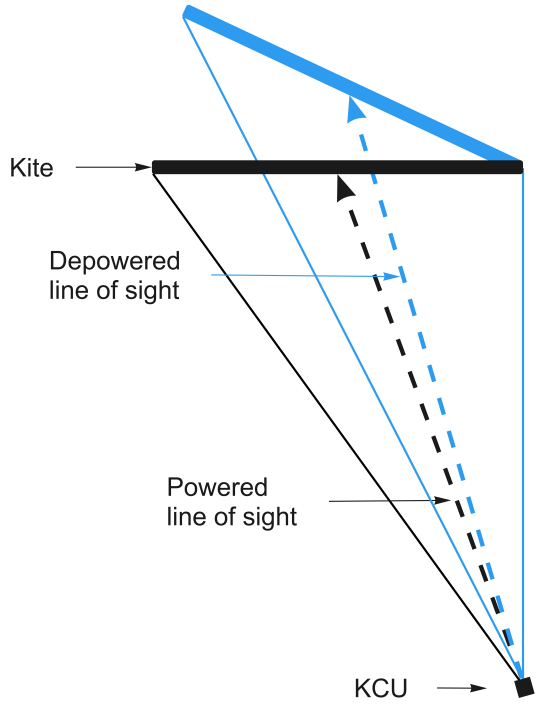

Figure 4.4: Effect of the kite pitching on the line-of-sight.

Kite deformation

Kite deformation is caused by a change in the loading conditions. An apparent velocity change, either in direction or magnitude, affects the loading conditions and could be caused by a change in the wind velocity, a different flight direction of the kite or a different kite velocity. Another factor contributing to a changing loading condition, and hence deformation, is the shape deformation itself. This is the result of the effect of the shape on the forces and the effect of the force on the shape, i.e. the FSI loop (see Sec. 2.1.2). The deformation of the kite changes the lengths of the line-of-sight to different kite elements and can also affect the angle between the video still and the object (see Fig. 4.5).

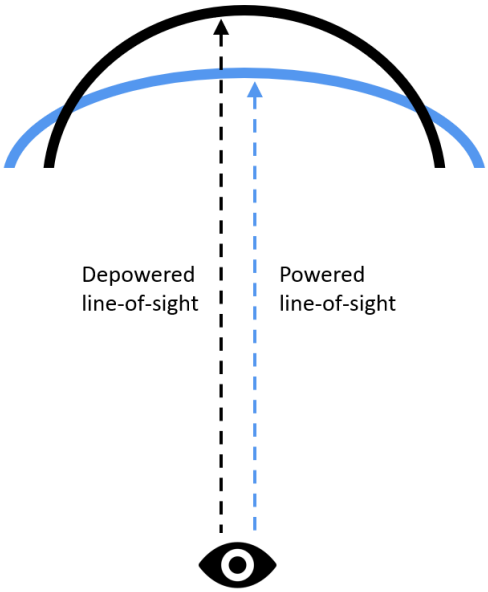

Figure 4.5: Simplified 2D representation of how deformation can affect the length of the line-of-sight. The anhedral angle change is taken here as example.

The changes in the length of line-of-sight and angle effects are taken into account by comparing the strut lengths. By assuming that the strut lengths remain constant one can compare the measured pixels between extreme states. Under the constant length assumption, the relative difference can only be attributed to a change in line-of-sight and angle. Therefore, the difference is formulated as a ratio and used to filter out the line-of-sight and angle-induced distortion. For measuring the TE lengths, it is assumed that the inferred distortion will be the same as it is for the accompanying struts. For each plate, the effect must be determined separately because a different angle and line-of-sight with respect to the KCU could be present. For the width of the kite, the averaged relative distortion of all the struts is used.

4.1.2. Results

In both videos, several stills were selected which represent the extreme states in straight and turning flight. The distortions were measured and removed, leaving one with pixel lengths that can be compared based on their relative differences expressed as percentages. The knot and pulley positions were also measured in percentage change, based on the relative distance they are in between two neighboring struts. An expression in percentages was chosen because the required output is the respective change and not the number of meters. Another argument for leaving it as a percentage is that the transformation step could cause additional uncertainty.

To remove random measurement errors, the resulting percentages are averaged for each video, i.e. the mean of the found samples is used to reduce the variation induced by errors. Random measurements errors could arise from an incorrect selection of the number of pixels by hand, the wrong timestamp selection and due to vibrations of the system as a whole. The KCU, tether, bridle lines and kite wing together are prone to vibrate causing a continuous change in distortion and shape. An indication of the reliability of the measurements comes from the standard deviation (σ) (see Eq. 4.1). Where μ represents the mean and N the number of samples. More samples would reduce the random error, thereby increasing the accuracy, commonly represented using the standard error (SE) (see Eq. 4.2).

$$\sigma = \sqrt{\frac{1}{N}\sum_{i=1}^{N}(x_i - \mu)^2} \tag{4.1}$$

$$SE = \frac{\sigma}{\sqrt{N}} \tag{4.2}$$

The results of both videos are averaged to decrease the existing systematic errors. Potential systematic errors could arise from how the camera distortion is removed, how a constant strut assumption is used to deal with the distortion changes between states and due to a camera misalignment. The latter can be reduced by averaging the measurements for the left and right parts of the straight flight. For turning flight, one must average the results of both left and right turns, which only works if the assumption of similarity in the turns holds. Regarding reliability, both test-retest and Intra-observer reliability could be treated by doing multiple analyses. For the latter, the analysis must be done by different researchers. It is decided to leave the quantitative assessment of the systematic errors for another study due to the non-optimal experimental setup, a too-small sample size and time constraints.

The struts and panels have been numbered to enable reporting of the measurements (see Fig. 4.6). The 'strut' length is indicated in quotation marks because the distance between the bridle line attachment point was taken and not the true strut length. This is in order to be consistent with the developed models, similarly as why the bridle line tip-to-tip width is measured and not the maximum width.

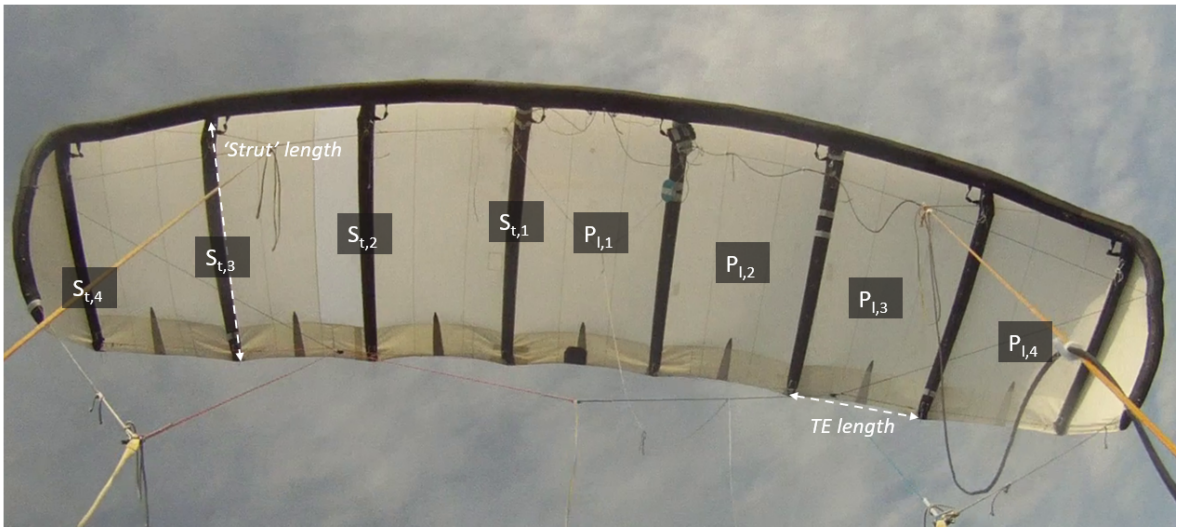

Figure 4.6: Video still indicating the numbered struts ($S_{t,i}$), plates ($P_{l,i}$) and the measured lengths [1].

Straight flight

A 5% decrease in width was found going from the powered to the depowered state (see Table 4.1). Physically, this makes sense since, upon an increase in force, one would expect a flatter shape [46]. The TE lengths of the plates were found to decrease when powering the wing. The change is present due to the ability of the canopy to balloon. Since ballooning scales with the force acting on the canopy, a decrease in length is as expected. An effect that counteracts the decrease in length is a global one and is caused by an increase in the sideways component of the local force vectors. These forces stretch the kite out, i.e. they pull the struts outwards hence reducing the ballooning. Because the observed behavior is a decrease in TE length, the force component that causes ballooning can be concluded stronger. The underestimation of the angle change due to an increase in anhedral angle causes a respective underestimation of the width of the TE of $P_{l,4}$. Therefore, the relatively large measured ballooning for the TE of $P_{l,4}$ is considered a faulty measurement. The averaged distortion effect used for the total width is, therefore, based on $S_{t,1}$, $S_{t,2}$ and $S_{t,3}$.

Table 4.1: Photogrammetry results of the relative length changes.

	Width	**TE $P_{l,1}$**	**TE $P_{l,2}$**	**TE $P_{l,3}$**	**TE $P_{l,4}$**
Difference	-5.0%	1.9%	2.0%	3.4%	-14.2%

The pulley positional and knot positional values match the qualitatively observed trend (see Table 4.2). The pulley points move inward when depowering, whereas the knot points move outwards.

Table 4.2: Photogrammetry results governing the changes of the pulley and knot line-of-sight canopy crossing position.

	Pulley	**Knot**
Powered	80% inwards from $S_{t,3}$	72% inwards from $S_{t,4}$
Depowered	3% inwards from $S_{t,2}$	17% inwards from $S_{t,4}$

The sampling distribution of the width measurements shows some degree of variation as expected (see Fig. 4.7). The measured pixel values have been scaled such that the mean of the powered measurements equals the design width. The behavior has been linearized in between the powered and depowered state, to obtain estimates for the width at power settings (u_p) between zero and one. The variation is represented by the standard deviation which is equal to $0.23\,$m. The standard error (SE) was found equal to $0.73\,$m and is used to plot a confidence band around the linearized behavior. This is done by adding half the SE above and below the mean.

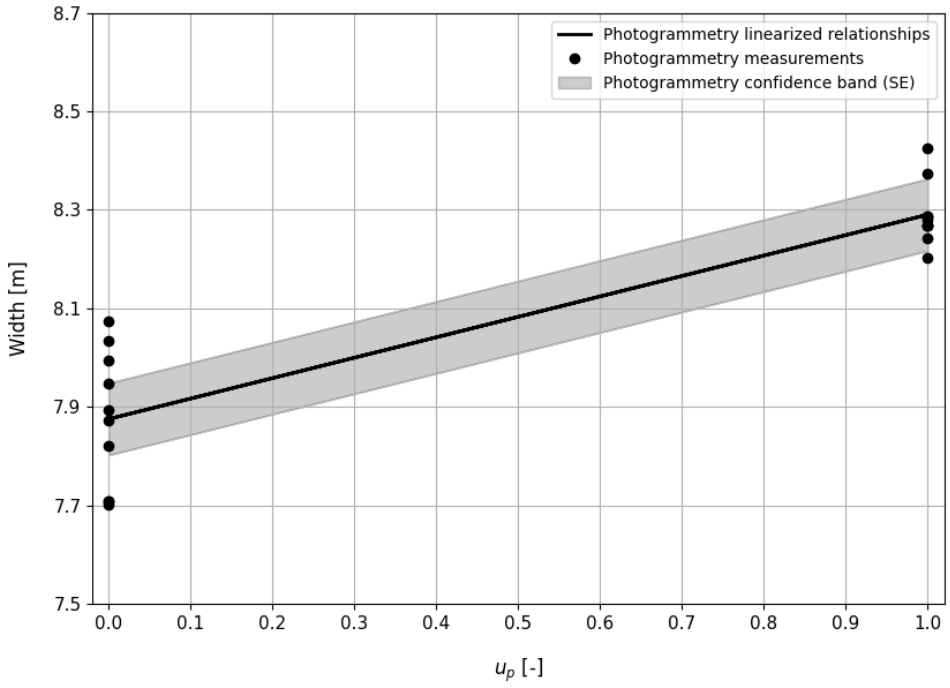

Figure 4.7: Sampling distribution of the width. Where the grey band indicates the standard error (SE) and each dot represents an individual measurement.

Turning flight

The increased number of effects causing uncertainty has led to the conclusion that the overall inaccuracy of the resulting data coming out of the turning analysis is too low. One of the effects comes from the difficulty of identifying the precise timestamp of the turning apex. Another effect is the increase in

distortion due to larger shape differences. The asymmetric deformation of the kite is one reason for the increase in magnitude, another is the increased relevance of the KCU swing during turning maneuvers (see Fig. 4.2).

A qualitative comparison of the experienced asymmetric deformation and the predicted deformation is, however, still possible. From several video stills the expected asymmetric deformation was found (see Fig. 4.8). Another relevant finding is the slacking of two bridle lines, different than those found in the depowered state.

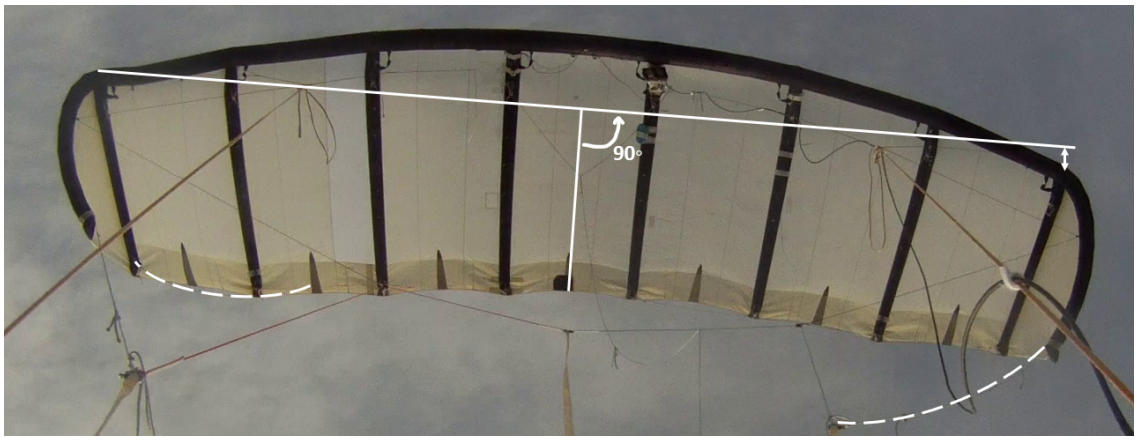

Figure 4.8: Video still of a left turn [1]. Where the white dotted lines indicate the slacking bridles and the full white lines qualitatively show the expected asymmetric deformation.

4.2. Design geometry

The required inputs for the developed models are the 3D design shape specified through the bridle line attachment coordinates, an estimate of the initial positions of the knots and pulleys in the bridle line system, the extension of the depower and steering tape and the lengths of all the bridle lines.

A 3D CAD file of the V3 in 2012, i.e. one that is not equal to the V3.A used during the analyzed experiments was provided by Kitepower B.V. (see Fig. 4.9). The 3D coordinates of the bridle line attachment points were extracted (see App. A). The bridle fan connections attached near the LE are simplified by representing them with one line. The struts are all parallel to each other, the measurement errors between the LE and TE point were therefore removed by making its span-wise coordinate match. Hereafter, the coordinates are scaled such that the kite bridle line attachment tip width matches the design width of $8.3\,\mathrm{m}$. Finally, a transformation of the coordinates is made to place the KCU at the origin.

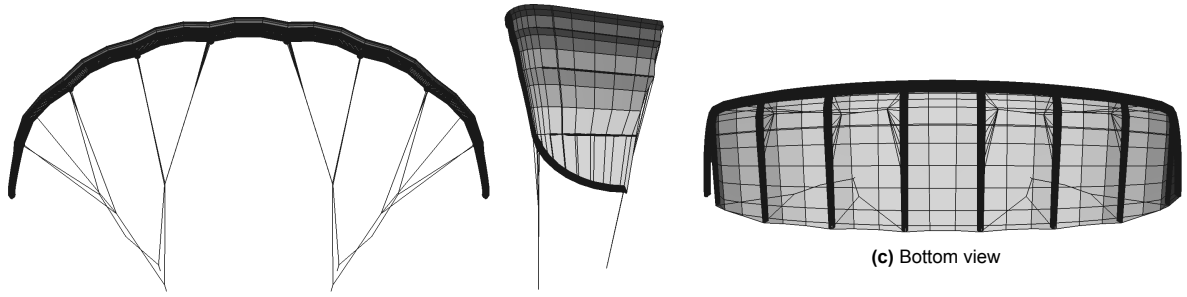

(a) Front view

(b) Side view

(c) Bottom view

Figure 4.9: CAD drawing of the initial design of the V3 [1].

In 2018 a document of the kite development at Kitepower B.V. was made which contained specifications of certain design aspects of the V3 [60]. Of particular interest are the provided specified bridle

line system lengths measured on 30 July 2017, which is five months after the measurements campaign.

The specification of the KCU bridle line system is still missing, which is a critical subset of the bridle line system present at the TE (see Fig. 4.10). The KCU bridle line system is critical because it is used to actuate the kite. Asymmetric actuation is done by changing the steering tape lengths and symmetric actuation by changing the depower tape length. The bridle line system starts from where the tether ends, which is a point generally referred to as the bridle point. The model is, however, build starting from the KCU. This is possible because J. Breuer, who is CTO at Kitepower B.V., identified that all bridles of the LE and TE were attached to the KCU. This modeling decision was taken because it ensures that the models have the same viewpoint as the photogrammetry. The only difference between modeling from the KCU or the bridle point is a straight line connecting the two. For future research that would also model the tether, one would only have to add a straight line. Furthermore, J. Breuer was so kind as to provide the KCU bridle line lengths that were flown with in 2017 (see App. A).

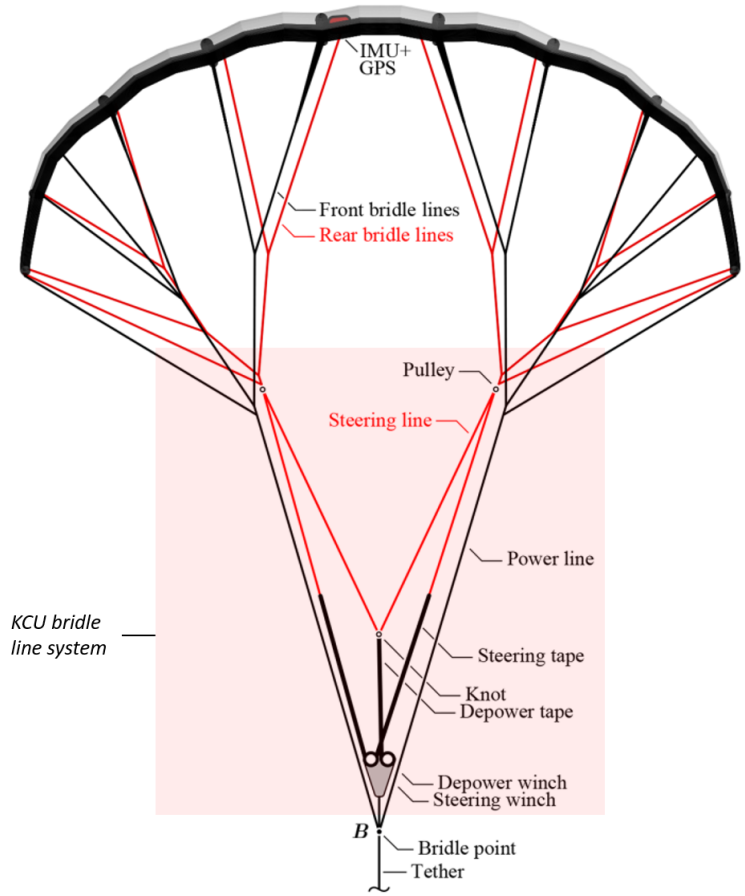

Figure 4.10: Adjusted bridle line system representation, with the red square roughly outlying the KCU bridle line system [47].

The goal is to compare the model predictions with the photogrammetry results, which means the steering settings and the maximum line lengths must be known. To do so, the measurements made by the potentiometers of the KCU, during the same day as the footage, were analyzed. The values of multiple pumping cycles were averaged. The depower tape was found to differ with 628 mm between minimal and maximal power settings. The minimal length of the depower tape (l_d) is 1098 mm, which is observed during the powered state. The power setting (u_p) scale has been adjusted such that the maximum and minimum values correspond with those observed during flight. For the steering tape, maximal steering of 40% of the total length was found. With a neutral state of 1600 mm, this leads to a steering tape of 1040 mm on one side and 2160 mm. M. Schelbergen a Ph.D. researcher at the TU

Delft, found an average depower tape length difference (Δl_d) of 8% between powered and depowered state from investigating a larger data set of the V3 out of 2019. This is smaller than the $\Delta l_d = 13\%$ observed from analyzing just two samples, the difference could come due to the less extreme settings used during the larger data set collection in 2019 [56]. To check the sensitivity of the models to Δl_d, the two most advanced models will be tested using both $\Delta l_d = 8\%$ and $\Delta l_d = 13\%$.

Upon comparing the found bridle line system lengths with the footage, it was found that additional lines were present. Two of those lines attach the tip to the line from the KCU to the pulley, somewhere on the steering lines or the line above it. This results in a kink in this line and an additional knot (see Fig. 4.11). This is one reason why a reversed engineering process was used to find the 'correct' bridle line lengths. Another reason was to ensure that the powered state result matches the design CAD state. This required changing the line lengths of several bridles (see App. A). This approach has its shortcomings and ideally one would measure all bridle line lengths on the day of the test to ensure that the proper input is used.

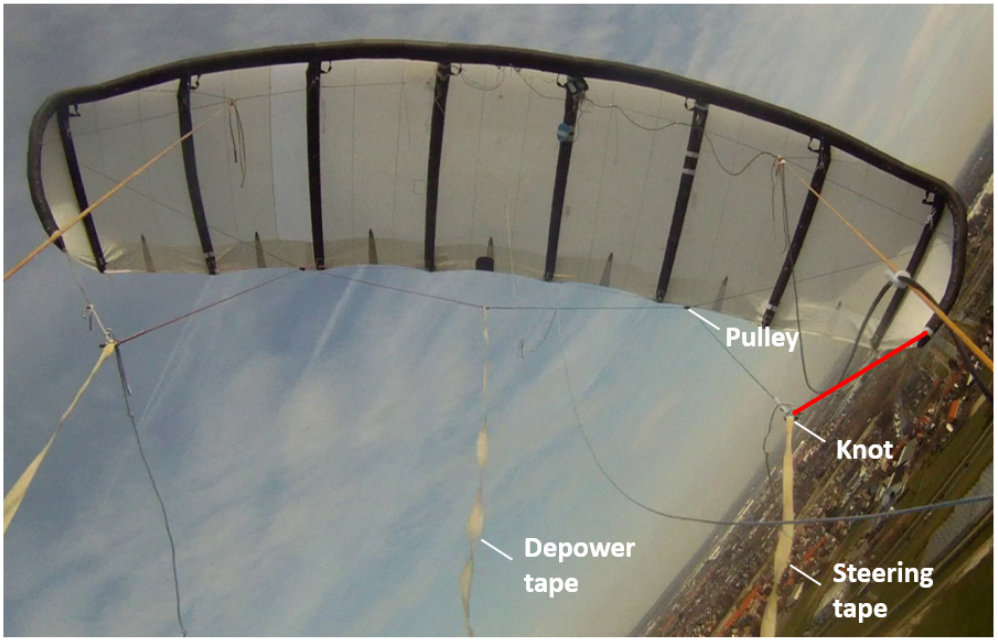

Figure 4.11: A video still indicating the positions of the knots and pulleys [1]. Where the red line indicates the 'new' line.

5

Wing models

For developing a model of the kite wing, a numerical representation is needed. To ensure the accuracy of this representation, one must consider what the main contributing structural elements of the wing are. From this analysis, a modelling hypothesis is formed (see Sec. 5.1). The hypothesis leads to a wireframe representation of the kite wing (see Sec. 5.2). The goal is to develop a novel structural model with an ideal balance between accuracy and computational cost. Several wing models with differing fidelity levels have, therefore, been developed (see Sec. 5.3).

5.1. Modelling hypothesis

Airborne wind energy companies are aiming for a design that produces the most load because that leads to more energy production. The parts of the canopy that produce lift parallel to the longitudinal tether axis produce more energy compared to those that are less aligned. This is attributed partly to that the latter parts of the canopy produce a local lift vector pointing outward, i.e. part of the load produced is counteracted by the other side of the kite and is thus not as effective towards the energy production. Another reason why the middle, more flatter parts, contribute more towards the energy production is that they generate more force compared to the outer parts of the kite. The flatter parts have more optimal flow angles and larger projected surface areas. The kites of Kitepower B.V. have likely been becoming flatter with each evolution because of this increased useful load potential (see Fig. 5.1).

Figure 5.1: Kitepower B.V.'s kite evolution from left to right one sees the: V2, the Hydra and the V3 [60].

At the same time, the kites have also been getting more bridle lines, most likely to be able to handle the increased wing loading. Adding bridles also has negative effects: it increases drag, adds weight and it decreases the depowering ability of the kite. The depowering ability is reduced by restricting the pitch movement, which depending on the design makes either the reel-in or reel-out phase less efficient.

If the kite wing were to be a ram-air kite, the contribution of the kite wing to the structural strength resisting rotational deformation would be close to zero. With rotational deformation, the main deformation modes, i.e. bending and twisting, are referred to. The LEI kite and ram-air are quite close in terms of

structure. One of the differences is that the ram-air kite has open holes at the front making the pressures depend on the amount of air coming into the kite. The LEI kite on the other hand has a closed tubular frame that is pressurized upfront, which enables higher pressures. Therefore, the structural strength contribution of the tubular frame of the LEI generally contributes more than the pressurized air of the ram-air. The shape of any kite is determined by the force balance between lift and its counterpart, which for the ram-air kite is carried mainly by the bridle line system. This is only possible because of the elongation resisting properties of the membrane canopy. Without substantial elongation resistance, large local ballooning effects would become possible resulting in a different less-optimal shape (see Fig. 5.2a and 5.2b). This illustrates the importance of bridles and membrane towards resisting deformation of the ram-air kite.

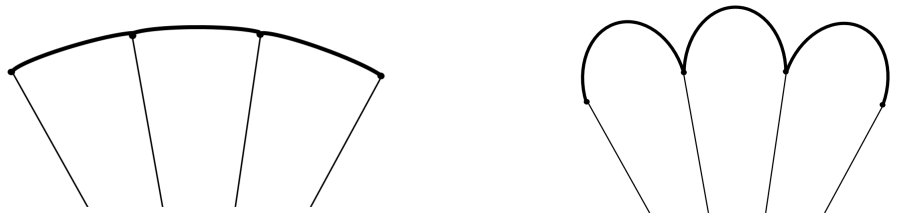

(a) 'Normal' elongation resistance properties. **(b)** Low elongation resistance properties.

Figure 5.2: Schematic illustration of a kite with three segments.

Furthermore, ballooning is a relevant factor for the aerodynamics of the kite, because it changes the aerodynamic force production by altering the chamber. Kitepower B.V. has put a wire at the TE of the V3 to reduce these deformations, for LEI kites this generally leads to higher efficiency [5].

The V3 kite has the entire tubular frame supported, i.e. on all struts on both the LE and TE bridle line attachment points are present. Assuming that the contribution of the tubular frame towards the structural strength resisting rotational deformation is low compared to the bridle line system, the same conclusion as drawn for the ram-air kite can be made. This leads to the main hypothesis under which the deformation models operate: *one can describe the shape of the V3 using a wireframe wing model represented by the bridle line attachment points, whose coordinate changes are modeled using a bridle line system model and ballooning relations.*

Modeling the kite deformation based on this key hypothesis is a novel idea, making the developed models the first of their kind. The first point supporting the assumption is that the LEI kite wing structure without aerodynamic loading is so flexible that it bends under its weight [5]. Another argument comes from Kitepower B.V., who mentioned that during one of their experiments the tubular frame lost its air pressure and thereby the structural properties arising from that pressure. The fully-bridled LEI kite that they were flying did, however, not visually appear to change its shape as a result. In other words, while the LEI kite structure was reduced to only bridle lines and a membrane canopy, the same shape remained. The shape must thus have been dominated by these two components. Another qualitative argument comes from several discussions had with kite designers, whom all identified that the main role of the tubular frame is to resist compression and not bending.

5.2. wireframe representation

The kite wing can be represented by spanwise segments, where each segment consists of a LE tube, two struts and the TE membrane (see Fig. 5.3). These segments are supported on the LE by a bridle fan and at the TE by a single bridle, which together are modeled as four bridle line attachment points placed in each corner of the respective kite segment.

Figure 5.3: Two images of the V3.A kite, where the red quadrilateral indicates one of the spanwise segments and the red dotted circles indicate the bridle fan [60]. The curved lines of the membrane canopy TE in between the strut tips demonstrate the ballooning.

The kite wing is discretized into N panels, where each panel represents a kite segment. The corners of the panels are the bridle line attachment points and the edges, representing the LE tube and struts, are assumed of constant length. The TE represents the canopy membrane and can vary in length due to ballooning, which is modeled using empirically obtained relations (see Sec. 4.1). Furthermore, it is assumed that the panel itself does not bend, meaning that the lines describing the edges stay straight. This leads to a wireframe representation of the kite (see Fig. 5.4) The deformation degrees of freedom (DOF) of the plate representation of the kite are a possible twist deformation of the LE tube elements and the rotations of the plates at their connections. The latter LE connections can be interpreted as gimbal joints. An alternative way to describe this is that one approximates the continuous bending of the tube by the rotational DOF of a multi-body model of the tubular frame. No structural properties are modeled using this approach, meaning that when excluding ballooning effects the shape deformation can be simulated based on pure geometrical inputs. These models become constraint-based, where the shape deformation is induced by bridles and not by forces overcoming the structural resistance of the kite wing and bridles.

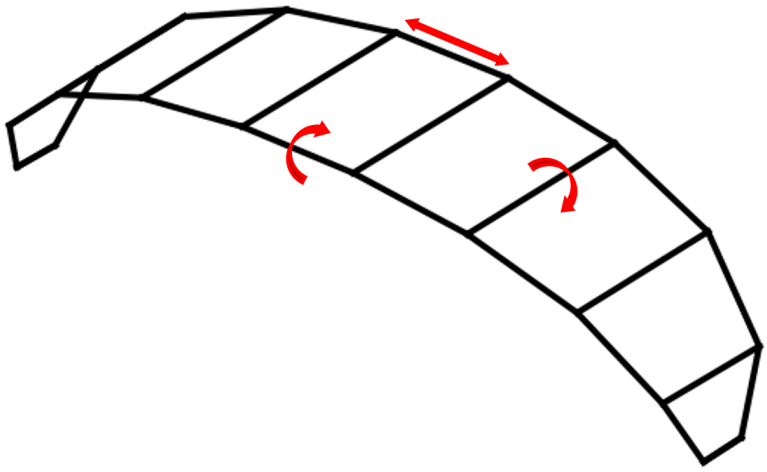

Figure 5.4: wireframe representation of the kite wing, where each kite segment is represented by a plate. The red arrows indicate the DOF of the plates.

5.3. Discretisation levels

The kite wing is represented by N panels, where each is supposed to represent one of the nine segments enclosed by the tubular frame. Therefore, the most accurate representation is to use nine panels, since each panel edge than corresponds to the tubular frame edge, excluding the TE that is. This makes the constant length assumption more likely to be an accurate representation considering the compression resisting properties of the tubular frame.

In some modeling efforts, including more detail results in an enlargement of the errors. This is caused by the additional assumptions that increase the discrepancy with reality, i.e. sometimes the accuracy is higher when including fewer details. Models using less than nine panels will be developed to study this particular effect and for studying the mechanistics of the model, for verification and because lower-fidelity models generally have low computational cost. The following wing models are developed: a triangular two plate model (see Sec. 5.3.1), a quadrilateral 2-plate model (see Sec. 5.3.2), a quadrilateral 3-plate model (see Sec. 5.3.3), a quadrilateral 7-plate model (see Sec. 5.3.4) and a quadrilateral 9-plate model (see Sec. 5.3.5). Arguments for selecting some of these particular kite wing representations have arisen from how the bridle line system is modeled (see Ch. 6).

5.3.1. Triangular 2-plate model

The smallest functional substitute model of the kite model is a rigid rod. One can extend this 2D model of a rigid rod to a 3D model with triangular faces. one can assume that the triangular face is of constant shape, by excluding the ballooning of the trailing edge. For this model, two such triangular faces are used, which can fold with respect to one another over the middle hinge line (see Fig. 5.5a).

Under the assumption that the edges remain of constant length, the angles of the triangular plates remain constant. Because the plates must remain in contact over the middle line, this means that the triangular 2-plate model can't simulate asymmetric deformation. This would only be possible if the plates collapse into one another or separate at the middle line. The model can simulate symmetrical deformation, through the folding motion.

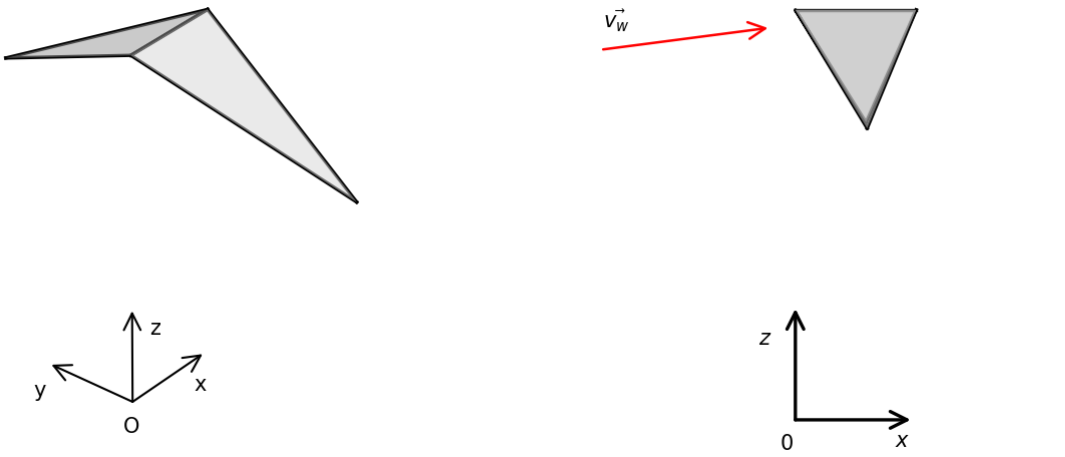

(a) Orthographic view of the wing model.

(b) Side view, demonstrating the wind velocity vector at an angle of attack.

Figure 5.5: Triangular 2-plate wing model.

A Cartesian reference frame (x, y, z) is defined with the KCU as the origin. The z-coordinate is defined positively upwards, the x-coordinate positive in the downstream direction and the y-coordinate is defined positive to the left. The triangular 2-plate representation in this reference frame has the middle chord parallel to the (x, y) plane, which is how the design powered state will be represented throughout

this research. The apparent wind velocity vector ($\vec{v_a}$) determines the angle of attack and is itself not parallel to the (x, y). It is drawn to illustrate this point, from which it becomes clear that the angle of attack of the middle chord is not zero in the design powered state (see Fig. 5.5b). The angle of attack in the powered state is assumed equal to $10\,°$ [47, 53].

5.3.2. Quadrilateral 2-plate model

The quadrilateral 2-plate model is almost the same as the triangular 2-plate model. The difference arises from the two additional points that turn the triangular faces into quadrilaterals (see Fig. 5.6). By excluding ballooning, all the edges are of constant length. Asymmetric actuation is not possible because it would require the two plates to fold into one another or to separate the connection. Symmetric actuation will be modeled and compared to the triangular 2-plate model, to see the effect of different calculation methods and the effect of the additional two points.

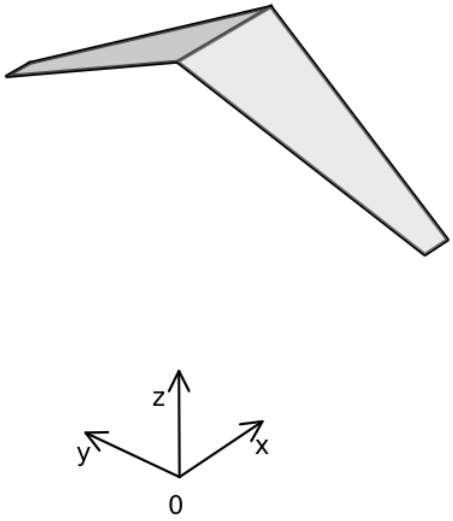

Figure 5.6: Quadrilateral 2-plate model.

5.3.3. Quadrilateral 3-plate model

The quadrilateral 3-plate model is different from the quadrilateral 2-plate model since it has a center plate, which represents the center canopy piece in between the two off-center center struts (see Fig. 5.7). Ballooning is excluded, the edges are therefore of constant length. Because there is an additional plate there are now two hinge lines over which the kite can bend.

The middle plate TE points are free to move, which allows for twisting of the center plate. This twisting enables asymmetric actuation, a similar process happens physically when the kite wing deforms. The model allowing asymmetric actuation is important because it causes asymmetrical deformation which enables the kite to turn. Symmetrical actuation is also possible and will be compared to the other models, to study the effect of adding a plate.

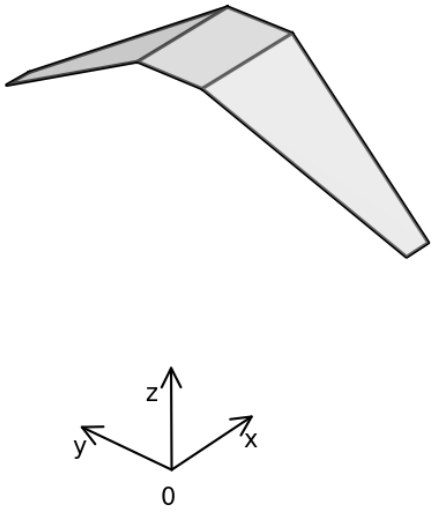

Figure 5.7: Quadrilateral 3-plate model.

5.3.4. Quadrilateral 7-plate model

The quadrilateral 7-plate model is the same as the quadrilateral 3-plate model, only with more panels (see Fig. 5.8). The outer two panels are modeled as one, due to slacking bridle lines observed during the photogrammetry study (see Fig. 4.3). This model is developed with and without ballooning, meaning that the plate TE edges can now vary as a function of the power setting. Lastly, both asymmetric and symmetrical actuation can be simulated.

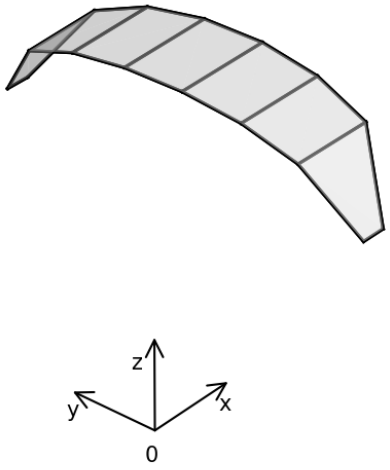

Figure 5.8: Quadrilateral 7-plate model

5.3.5. Quadrilateral 9-plate model

In the quadrilateral 9-plate, now all the plates represent a kite wing segment with at the LE and sides the tubular frame and at the TE a ballooning canopy (see Fig. 5.9). This is the most detailed representation of the kite wing that will be presented in this research and it follows the assumption that each kite wing segment can be represented by a plate. The 9-plate model is developed with and without ballooning, both are used to allow one to assess the effect including ballooning has. The bridle line system model used to calculate the deformations of the 9-plate model can include the outer plates, because it can deal with slacking lines (see Sec. 6.3).

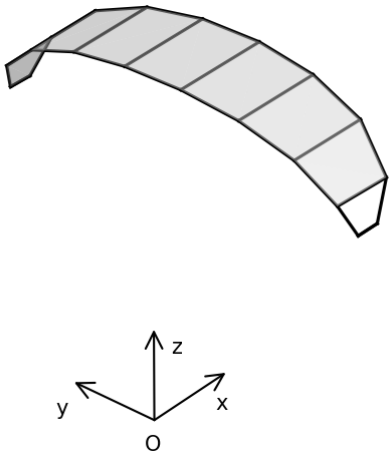

Figure 5.9: Quadrilateral 9-plate model.

6

Bridle line system models

The bridle line system is relevant because its job is to distribute the load onto the kite wing, provide stability and enable control. If control could be achieved through minimal actuation one could reduce the KCU mass. If one could minimize the number of bridles, both mass and drag would be reduced. A drag reduction causes an increase in aerodynamic performance and a mass reduction would increase the operating wind range. The argument was made that bridles dominate the kite shape (see Ch. 5), therefore, the bridle line system will be used to predict the deformation. Furthermore, because part of the goal of this research is to develop insights that can increase aerodynamic performance, understanding the bridle line system mechanics is key.

The bridle line system models use symmetric and asymmetric actuation as input. The input values are found using the empirically determined relationship between the power setting (u_p), the steering setting (u_s) and the amount of line length change (see Sec. 4.2). Changes in the power setting cause the kite to pitch. Previously, this has been modelled by Oehler and Schmehl using the extension of an imaginary line (l_{im}) connecting the KCU to the middle of the TE canopy of the V3 [47]. An imaginary line is used in some bridle line models whereas the perpendicular assumption is used in all developed models. For their model Oehler and Schmehl had to develop a relationship between depower tape extension and imaginary line extension. Because the depower tape splits into two lines (see Fig. 4.10), the extension of the imaginary line was modelled as half of the depower tape extension [47]. This approach is considered correct and is therefore incorporated in all discussed bridle line system models, that use an imaginary line. The KCU is defined as a point, therefore, both steering tape and depower tape are attached to the same point in space, i.e. the origin. In the models, the middle LE points are assumed to remain in place. The assumption is necessary for some of the algorithms to work and to enable consistent visualizations. The latter is achieved by not having a continuously changing image, which otherwise occurs due to the rotation with respect to the wind of the whole KCU, bridle and kite wing reference frame. By using this reference frame, the frame rotations with respect to the wind do not appear.

Multiple models differing in their fidelity have been developed, which will enable verification procedures and assessing if including more detail makes the prediction better or worse. Except for the particle system model, all developed models operate under the assumption that all bridle lines are straight. For the LE this is a valid assumption considering that the power lines of the V3 have been found to only change by $0.1\,^\circ$ to $0.2\,^\circ$ during operation [47]. In the existing literature, there is no proof for the lines going towards the TE. Straight TE bridle lines are, however, still assumed to allow a constraint-based geometric approach. Qualitative observations made during the photogrammetry analysis in straight flight affirm the validity of these assumptions, except for two slacking bridle lines. This problem is resolved by not modelling these lines, possible by formulating a 7-plate model (see Sec. 6.2.3). For turning flight, however, several lines did display slack. Because slack can't be modelled using a constraint-based geometric approach, most bridle line models are not able to accurately simulate asymmetric deformation.

The tetrahedron-based model is the simplest of the developed model (see Sec. 6.1). The trilateration-based model can deal with coordinate changes, hence able to predict more than only the change in width (see Sec. 6.2). Finally, the particle system model is developed that operates without a straight line assumption (see Sec. 6.3).

6.1. Tetrahedon model

The tetrahedron relations applied onto the triangular 2-plate wing make for the most simple representation of the relationship between change in anhedral and the power setting. The bridle line system is simplified to four straight lines all coming from the KCU (see Fig. 6.1). Pitching is the only possible motion and is controlled through a change in the imaginary line l_{im} connecting the KCU to the middle of the TE canopy.

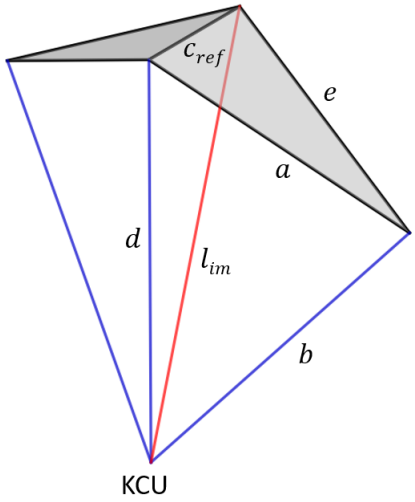

Figure 6.1: Schematic representation of the triangular 2-plate model. The blue lines indicate the lines attached to the LE and the red line the line attached to the TE (l_{im}).

The shape change can be calculated using tetrahedron relationships, possible since lines: b, d, a, e, c_{ref} are assumed of constant length. First the volume of the tetrahedron (V_T) spanned by lines: b, d, a, e, c_{ref} and l_{im} is calculated (see Eq. 6.1).

$$\begin{aligned} X &= d^2 + l_{im}^2 - c_{ref}^2 \\ Y &= b^2 + l_{im}^2 - e^2 \\ Z &= b^2 + d^2 - a^2 \\ V_T &= \frac{1}{12}\sqrt{4b^2d^2l_{im}^2 - b^2X^2 - d^2Y^2 - l_{im}^2Z^2 + XYZ} \end{aligned} \tag{6.1}$$

The second step is to calculated the area of the triangle (A_t) spanned by lines: d, l_{im} and c_{ref}. Lastly, the length of the line from point 1 that is perpendicular to the face of this triangle is calculated and multiplied by two, to obtain the width (W) of the kite (see Eq. 6.2). Due to symmetry multiplication by two is possible, as the other side will give the same result.

$$\begin{aligned} A_t &= \frac{1}{4}\sqrt{(l_{im}+d+c_{ref})(-l_{im}+d+c_{ref})(l_{im}-d+c_{ref})(l_{im}+d-c_{ref})} \\ \mathrm{W} &= 2\left(3\frac{V_T}{A_t}\right) \end{aligned} \tag{6.2}$$

6.2. Trilateration

The next calculation technique is based on a mathematical algorithm called trilateration. Trilateration in general is a geometric technique to find the position of a point based on distances to other points [28]. In this context, trilateration is the technique of solving the intersection problem of three spheres. Spheres and their respective centres and radii form the input and the result, if present, are their two intersection points. Because line lengths can change, one can take into account the ballooning of the TE canopy. The trilateration algorithm calculates coordinate changes and not width changes, therefore it can describe the whole shape of the kite. Another advantage over the tetrahedron algorithm is that besides triangular plates, this algorithm can calculate a kite representation of quadrilateral plates.

The problem trilateration solves is best illustrated in 2D, where it becomes the intersection problem of three circles (see Fig. 6.2). The resulting intersection point in 2D is in 3D a line connecting the two intersection points, one being in front of the paper and the other behind the paper.

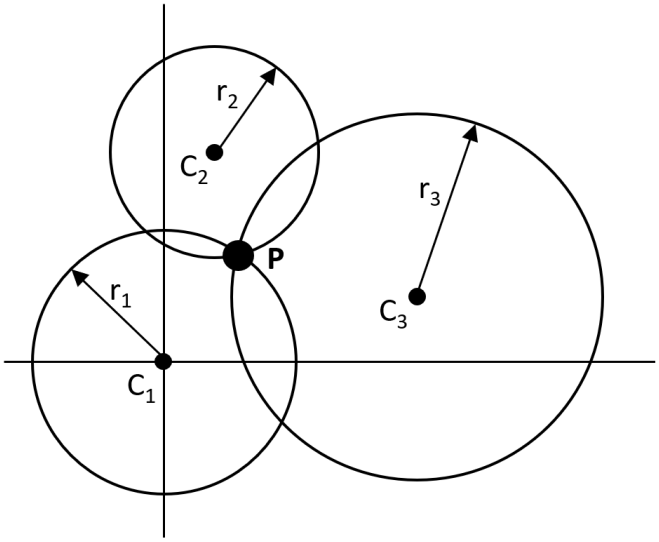

Figure 6.2: 2D representation of the 3D sphere intersection problem, with P representing the intersection point in 2D.

6.2.1. Model workflow

The best way to explain how trilateration works is by walking through an example calculation. The triangular 2-plate model is taken as a reference, where its change is caused by a symmetrical actuation. Applying another technique on the same wing model is useful because it enables a verification procedure.

Where the line length change of l_{im} was sufficient input for the tetrahedon algorithm to calculate the amount of pitching, trilateration also requires the coordinate change of point 4 (P_4) (see Fig. 6.3). The cos-law is used to calculate the depower angle (α_d) based on the extension of line l_{im}. Next step is to calculate the new coordinate of P_4 using α_d (see Eq. 6.3). The depowering of the kite is represented by the rotation around the front suspension point, not around the actual LE because the bridle line attachment points are located at about $0.5\,$m behind the real LE [47].

$$\begin{aligned} \alpha_d &= \arccos\left(\frac{d^2 + c_{ref}^2 - l^2}{2dc_{ref}}\right) - \frac{\pi}{2} \\ P_{4_x} &= c_{ref}\cos\left(\alpha_d\right) \\ P_{4_y} &= 0 \\ P_{4_z} &= P_{4z,old} + c_{ref}\sin\left(\alpha_d\right) \end{aligned} \tag{6.3}$$

With the new location of P_4 known, point 1 (P_1) and point 3 (P_3) can be calculated using trilateration.

The trilateration algorithm will be illustrated for the calculation of P_1. The calculation of P_1 is done similarly, only mirrored over the symmetry (x, z) plane. It is verified that the output of the model is indeed the same for P_3 and P_1 with only the y-value switched. The input into the trilateration algorithm for the calculation of P_3 are the initial coordinates of the powered state ($u_p = 1$) and the new location of P_4.

Calculating point 1

The first step is to define the spheres and radii. The radii are either known from lines of constant lengths or calculated using the norm of the vector, i.e. Pythagoras theorem applied in 3D. Sphere 1 has its center at the KCU (P_0) and its radius equal to line b (see Fig. 6.3). Sphere 2 has its centre at P_2 and its radius equal to line a. Sphere 3 has its centre at P_4 and its radius equal to line e. The intersection points of these spheres lie at either side of the plane spanned by the three spheres, looking solely at this plane the 2D representation of the 3D intersection is found again (see Fig. 6.2). By selecting the intersection points in a systematic order, the negative z' direction (see Eq. 6.5) is present on the right side. Meaning that when one wants to find the location of P_3 there can be only 1 solution.

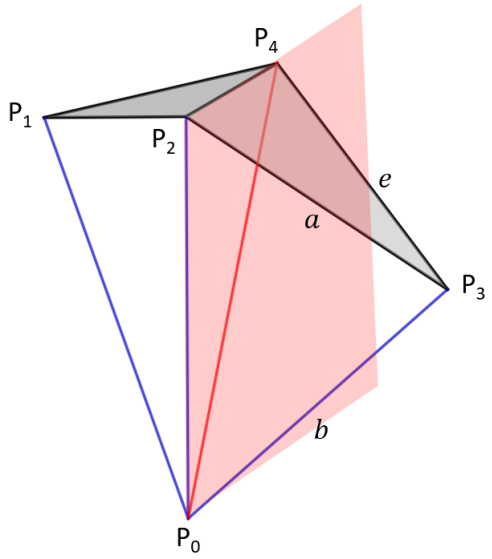

Figure 6.3: Illustration of the 2D plane spanned by P_0, P_2 and P_4, shown in red.

The second step is to transform the reference frame (x, y, z) to (x', y', z') such that point P_0 remains on the origin, point P_2 lies on the new x'-axis and point P_4 on the (x', y') plane. The transformation is defined by the unit vectors: $\vec{u}_{x'}$, $\vec{u}_{y'}$ and $\vec{u}_{z'}$ (see Eq. 6.4) [28].

$$\begin{aligned} \vec{u}_{x'} &= \frac{P_0 - P_2}{|P_0 - P_2|} \\ \vec{u}_{y'} &= \frac{(P_4 - P_0) - \vec{u}_{x'}^2 (P_4 - P_0)}{|P_4 - P_0|} \\ \vec{u}_{z'} &= \vec{u}_{x'} \times \vec{u}_{y'} \end{aligned} \tag{6.4}$$

Within this new reference frame the intersections points $(P_{3_{x'}}, P_{3_{y'}}, P_{3_{z'}})$ are found using the trilateration algorithm (see Eq. 6.5) [28]. The unit vectors are used to transform the intersection points their coordinates in the (x', y', z') frame back to the original (x, y, z) frame to find the coordinate of P_3. As mentioned previously, since P_3 is on the right side of the plane spanned by the three centres of the spheres, the solution will have the addition of the negative z-term $(P_{3_{z'}} \vec{u}_{z'})$.

$$
\begin{aligned}
P_{3_{x'}} &= \frac{|P_0 - P_3|^2 - |P_2 - P_3|^2 + |P_0 - P_2|^2}{2|P_0 - P_2|} \\
P_{3_{y'}} &= \frac{|P_0 - P_3|^2 - |P_4 - P_3|^2 + \vec{u}_{x'}(P_4 - P_0)^2 + \vec{u}_{y'}(P_3 - P_0)^2 - 2\vec{u}_{x'}(P_4 - P_0)P_{3_{x'}}}{2\vec{u}_{y'}(P_3 - P_0)} \\
P_{3_{z'}} &= \sqrt{|P_0 - P_3|^2 - P_{3_{x'}}^2 + P_{3_{y'}}^2} \\
P_3 &= P_0 + P_{3_{x'}}\vec{u}_{x'} + P_{3_{y'}}\vec{u}_{y'} \pm P_{3_{z'}}\vec{u}_{z'}
\end{aligned}
\tag{6.5}
$$

6.2.2. Uniform actuation

All bridle line system models that actuate the TE lines by the same amount, fall under the uniform actuation category. For both the triangular 2-plate model and the quadrilateral 2-plate model, this holds. For the quadrilateral 2-plate model the same cos-law (see Eq. 6.3) as was used for the triangular 2-plate model is used. The cos-law is necessary because the coordinate of the point on the TE of the middle chord is needed as input for the trilateration algorithm. The bridle system is modelled as six straight lines coming from the KCU to each corner point (see Fig. 6.4). Only symmetric actuation can be modelled and is done by actuating all TE bridle lines uniformly, i.e. all by the same line extension equal to half of the depower tape extension.

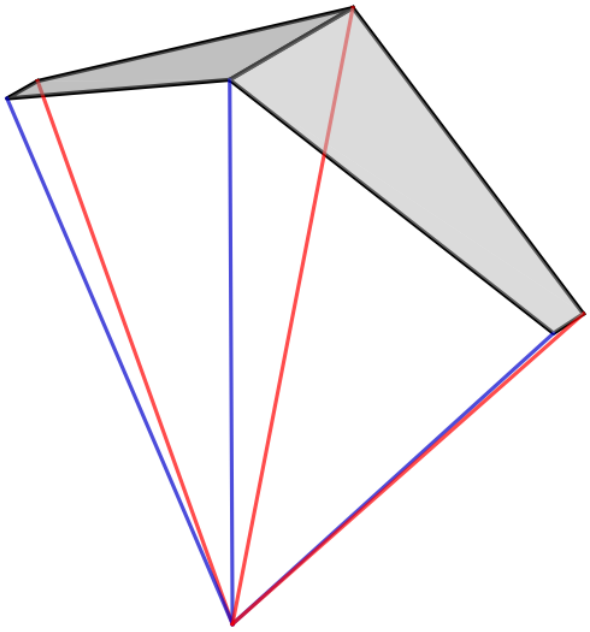

Figure 6.4: Quadrilateral 2-plate model. The blue lines indicate the lines attached to the LE and the red lines those that are actuated and attached to the TE.

The last uniformly actuated model is the quadrilateral 3-plate which does not require the cos-law. To illustrate why it does not, a brief description of how one goes about calculating the location of a tip TE point follows (see Fig. 6.5). Three points are needed as input for the trilateration algorithm, but now two LE points and the KCU can be used as input and a known TE point is thus not required. This is possible because both LE points were assumed to remain in place. The bridle line system is again represented by straight lines that connect the KCU to the corner plate. Symmetric actuation is done uniformly by all four TE bridles. Modelling asymmetric actuation is possible but will not be done due to the existence of slacking bridles.

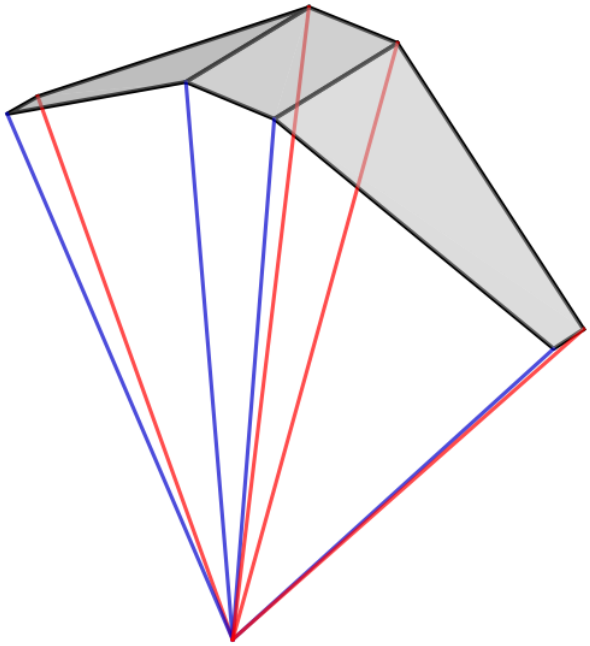

Figure 6.5: Quadrilateral 3-plate model. The blue lines indicate the lines attached to the LE and the red lines those that are actuated and attached to the TE.

6.2.3. Non-uniform actuation

A change in depower tape length, resulting from symmetrical actuation, is likely to not result in a uniform change in line length between the attachment points and the KCU. The first argument for why uniform might not be correct, is that the actual bridle line system does not consist of uniform straight lines. In reality, many other independent lines exist, which are connected by two pulleys and several knots. The positions of the pulleys and two of the lowest knots have been identified to lie on a different line-of-sight in the powered state compared to the depowered state (see Fig. 4.3). This horizontal shift is caused by a change in loading conditions, supporting the non-uniformly loaded hypothesis. From an aerodynamic perspective, the generated lifting force is known to be a function of the surface area and inflow angle. The surface area of the middle plates is larger and the inflow angle of the outer plates is less optimal with respect to the incoming flow, meaning more force is produced in the middle compared to the outer parts. Tip vortices caused by the pressure difference between the top and the bottom surface further decrease the lift force at the outer sections. In short, from an aerodynamic perspective, the loading can be concluded as non-uniform. Because the loading determines the bridle line layout it, therefore, provides another argument for why uniform actuation could not suffice. The last indication is that it was found that a 7-plate or 9-plate quadrilateral model with uniform symmetric actuation can't predict the shape for low-powered settings. For these cases, errors were caused due to the inability of the trilateration algorithm to find all sphere intersection points.

To achieve non-uniform actuation the level of detail of the bridle line system representation must be increased (see Fig. 6.6). The lowest knots and the pulleys will be modelled to do so, thereby representing part of the KCU bridle line system. The knots and pulley positional change must be calculated, using as input the empirically obtained relationships between the power setting and the line-of-sight of the knots and pulleys (see Sec. 4.1). The rest of the bridle lines are modelled as straight lines in between the KCU, knots, pulleys and bridle line attachment points. A non-uniform actuation of the bridle line attachment point is achieved because the actuation length and direction depends on the distance each point has to the moving knot and pulley points. Only symmetric actuation is modelled because for asymmetric actuation the lines attached to the tips slack and slack can't be taken into account.

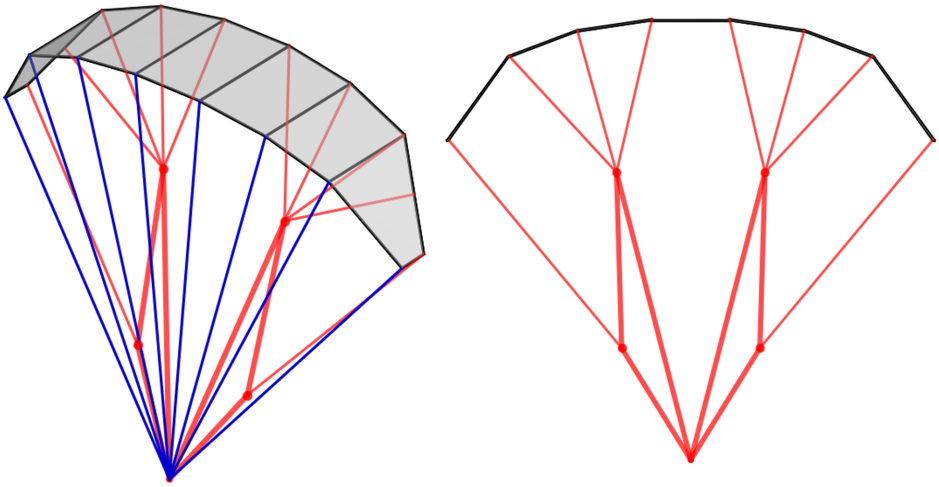

Figure 6.6: Quadrilateral 7-plate model. The blue lines indicate the lines attached to the LE and the red lines those that are actuated and attached to the TE. On the right a front view is shown with only the TE bridles visible, the thick red lines indicate the KCU bridle line system representation and the dots the knots and pulleys.

Once the knot and pulley position for a certain symmetrical actuation are known, all the coordinates of the bridle line attachment points can be calculated using the trilateration algorithm. The main change is that instead of the KCU, the knots and pulleys are now used as inputs forming the first sphere. Obtaining the knot and pulley position is, however, not trivial.

Calculating knot and pulley point positions

By thinking of the problem as a circle intersection problem, a solution can be found. The circles are in a 2D plane spanned by a line from the KCU to the LE mid point (LE_{mp}), a line from LE_{mp} to the line-of-sight its crossing point at the TE (P_{cross}), and from P_{cross} to the KCU (see Fig. 6.7). The first circle centre is placed at the KCU and its radius is equal to the length from the KCU to P_{cross} (R). The second circle is centered at the LE_{mp}, which is a distance d away from the KCU and its radius is equal to the length from LE_{mp} to P_{cross} (r). Rewriting the two circle equations into one equation one can solve for the z-coordinate of P_{cross} ($z_{P_{cross}}$) (see Eq. 6.6).

$$z_{P_{cross}} = \frac{d^2 - r^2 + (R + \Delta L)^2}{2d} \tag{6.6}$$

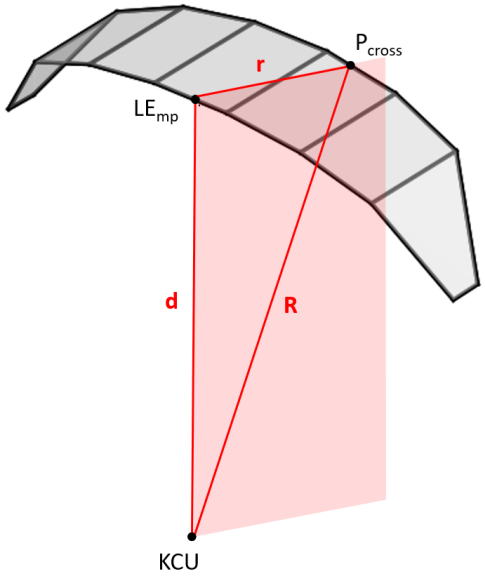

Figure 6.7: 7-plate wing model, with 2D plane spanned by LE_{mp}, P_{cross} and the KCU.

This described procedure is only possible by assuming that line r remains of constant length. The parameter d also remains constant, because the LE bridles do not change length. The actuation input is taken into account by adding a quarter of the depower tape extension (ΔL) to R. A quarter of the value is taken because at the pulley the lines have split twice, each time dividing the extension effects in half. The parameters for the powered state can be obtained from the known geometry and the empirically determined crossing point. Using the powered state as the initial state, the depowered state can be calculated since all other required parameters are known.

Using similar triangles $z_{P_{cross}}$ can be used to calculate the z-coordinate of the pulley point (z_p) (see Eq. 6.7). The first triangle consists of: R, d and the distance along the new x^*-axis and the second triangle of: the line from the KCU to the new pulley location ($L_p + \Delta L$) parallel to R, z_p parallel to $z_{P_{cross}}$ and distance along the same x^*-axis (x_p^*) (see Fig. 6.8a). With z_p known one can calculate the pulley its position along the x^*-axis (x_p^*).

$$
\begin{aligned}
L_p &= \sqrt{(L_{p,x} - KCU_x)^2 + (L_{p,y} - KCU_y)^2 + (L_{p,z} - KCU_z)^2} \\
z_p &= \left(\frac{L_p + \Delta L}{R + \Delta L}\right) z_{P_{cross}} \\
x_p^* &= \sqrt{(L_p + \Delta L)^2 - z_p^2}
\end{aligned}
\tag{6.7}
$$

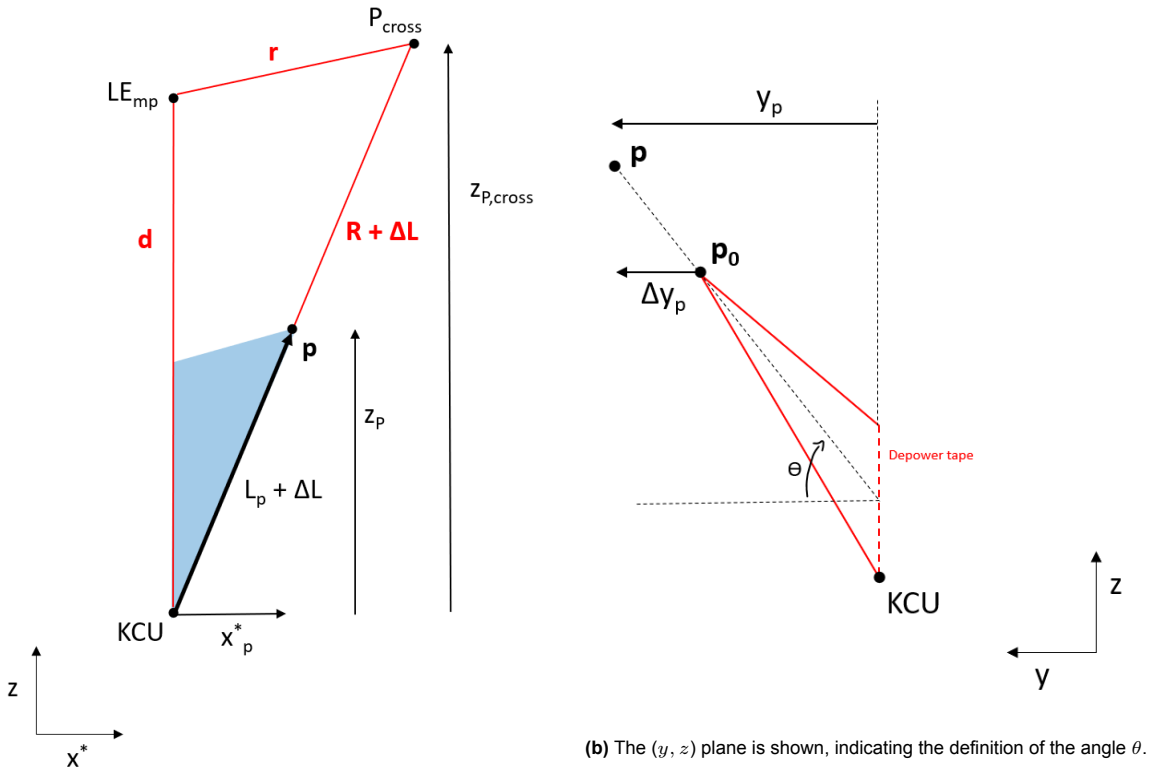

(a) The (z, x^*) plane is shown. Where the blue triangle illustrates the similar triangle to its larger brother, which is indicated by the red lines.

(b) The (y, z) plane is shown, indicating the definition of the angle θ.

Figure 6.8: Illustrations of the non-uniform calculation method.

The y-coordinate of the pulley (y_p) can be found by looking at the (y, z) frame and calculating the angle of the line R (θ) (see Fig. 6.8b). Using θ and ΔL the change in y-direction of the pulley (Δy_p) is calculated. This is only possible by assuming that θ does not change. By adding Δy_p to the old y-position ($y_{p,0}$) the y-coordinate of the pulley is found (y_p).

$$\begin{aligned} \theta &= \arccos\left(\frac{y_{p,0}}{\sqrt{(x_{p,0}^2 + y_{p,0}^2 + z_{p,0}^2)}}\right) \\ \Delta y_p &= \Delta L \cos(\theta) \\ y_p &= y_{p,0} + \Delta y_p \end{aligned} \tag{6.8}$$

With y_p and x_p^* one can use Pythagoras theorem to calculate the x-coordinate of the pulley (x_p) (see Eq. 6.9).

$$x_p = \sqrt{x_p^{*2} - y_p^2} \tag{6.9}$$

The same procedure as described above is applied to calculate the coordinate of the knot point.

Ballooning

Another version of the quadrilateral 7-plate model is developed incorporating ballooning, both with and without is modelled to allow verification procedures through comparison. Ballooning is taken into account using the experimentally obtained relations between TE plate length and power setting (see Sec. 4.1). Since not all nine kite wing segments are represented by 7-plates, the outer plates their TE change will be the percentage change of the outer segments. As a consequence of ballooning, the diagonal length within each plate also changes. As the distance between points is a necessary input for the

trilateration algorithm, the diagonal length between the inner TE point and outer LE point is assumed constant for the outer plates (see Fig. 6.9). The assumption is only needed one way because when calculating the outer TE points of a plate three sphere's can be selected that are connected through the edges of the plate and thus do not lie at unknown distances.

An alternative to assuming that the diagonal line lengths are constant is to formulate a system of equations for each plate. With the two inner point locations known, one can write the location of both outer points as a function of the edge length, the locations of the inner points, KCU and the outer points themselves. One ends up with a system of six nonlinear equations with six unknowns, the latter are the x, y and z location of each outer plate point. Solving this system of equations is not trivial and was found to take too much computational time to be useful.

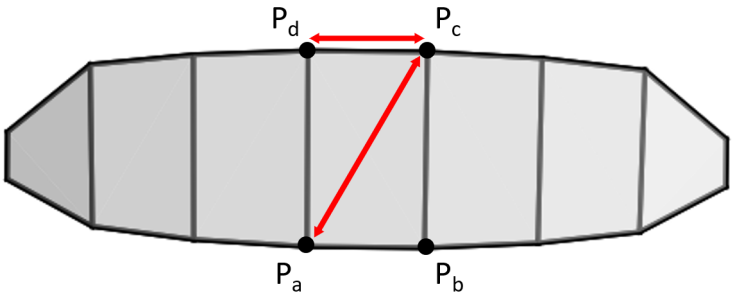

Figure 6.9: Top view of the quadrilateral 7-plate. The red arrows indicate the ballooning causing the TE length to differ, which alters the diagonal distance.

The middle plate is the exception to the rule and does not require the constant diagonal length assumptions. Because the struts of this plate are of equal length the middle plate is a special kind of quadrilateral, called an 'isosceles trapezoid'. For an isosceles trapezoid the Ptolemy's theorem holds which relates edge lengths ($E_{i,j}$) to the diagonal length ($D_{i,j}$) (see Eq. 6.10) [12].

$$
\begin{aligned}
E_{a,b} &= \sqrt{(P_{a,x} - P_{b,x})^2 + (P_{a,y} - P_{b,y})^2 + (P_{a,z} - P_{b,z})^2} \\
E_{c,d} &= \sqrt{(P_{c,x} - P_{d,x})^2 + (P_{c,y} - P_{d,y})^2 + (P_{c,z} - P_{d,z})^2} \\
E_{a,d} &= \sqrt{(P_{a,x} - P_{d,x})^2 + (P_{a,y} - P_{d,y})^2 + (P_{a,z} - P_{d,z})^2} \\
D_{a,c} &= \sqrt{E_{a,c}E_{c,d} + E_{a,d}^2}
\end{aligned}
\tag{6.10}
$$

6.3. Particle system model

The limitations of the trilateration based models arose in part from not being able to deal with slacking bridles. Representing the bridles by straight lines of constant length does not allow one to accurately model all nine kite wing segments nor asymmetric actuation. The latter is a must as it allows the kite to turn, without which a kite can't fly pumping cycles. Furthermore, to incorporate non-uniform steering additional empirical relations were needed for the 7-plate model. These empirical relations stand in the way of the potential of the model because needing upfront information makes applying it to other kites or bridle line system configurations impossible without a test flight. Therefore, infeasible to use as the basis for the desired design model.

The particle system model (PSM) overcomes these problems and is developed both with and without ballooning (see Fig. 6.10). Because ballooning is a force-based phenomenon, there are extrapolation problems, which are expected to be resolved when incorporating the PSM into a FSI framework.

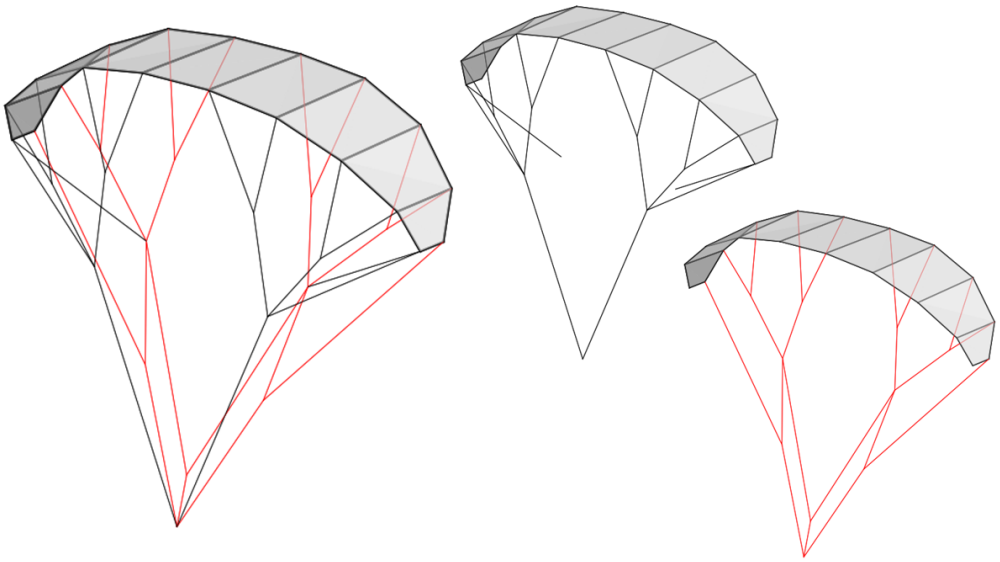

Figure 6.10: Orthographic view of the PSM on the left. On the top right top the bridles attached to the LE are shown, whereas on the bottom right those attached to the TE.

Solving the bridle line system with more detail to achieve the desired non-uniform actuation, was only possible by using empirical relations. Without the relations, the free angles of the middle part of the bridle line system cause infinitely many solutions, i.e. an under constraint problem. Thinking of 2D geometric shapes explains best why the free angles exist. A triangle with fixed edge lengths has a 'rigid' shape and can not move its angles freely. A quadrilateral with fixed edge lengths on the other hand, or any other shape with more than three lines, does not have a rigid shape. As the middle part of the LE bridles forms a pentagon the problem, therefore, thus has free angles. By incorporating a force input, the PSM can deal with the full bridle line system, allowing for an accurate representation of the occurring non-uniform actuation.

AWES tether elements are often dynamically modelled as springs with a spring stiffness, this enables dynamic models to reach a stable solution [23]. Modelling bridles as spring elements is generally not done due to their short lengths in comparison to the tether elements [9, 66]. An exception is the work of Geschiere, who extended the FSI model of Bosch et al. using the PSM of Fechner et al. to model an extendible tether and more bridle lines (see Sec. 2.1.1) [5, 23, 27]. The model was developed using a different approach that achieves less utility by not including the actuation system. To be more precise, the described dynamic PSM differs from the one developed here in: how the kite wing is represented (see Fig. 6.11a and 6.11b), which forces it takes into account, the numeric values, the addition of non-physical elements (compliant element) necessary for stability and not modelling the KCU bridle line system.

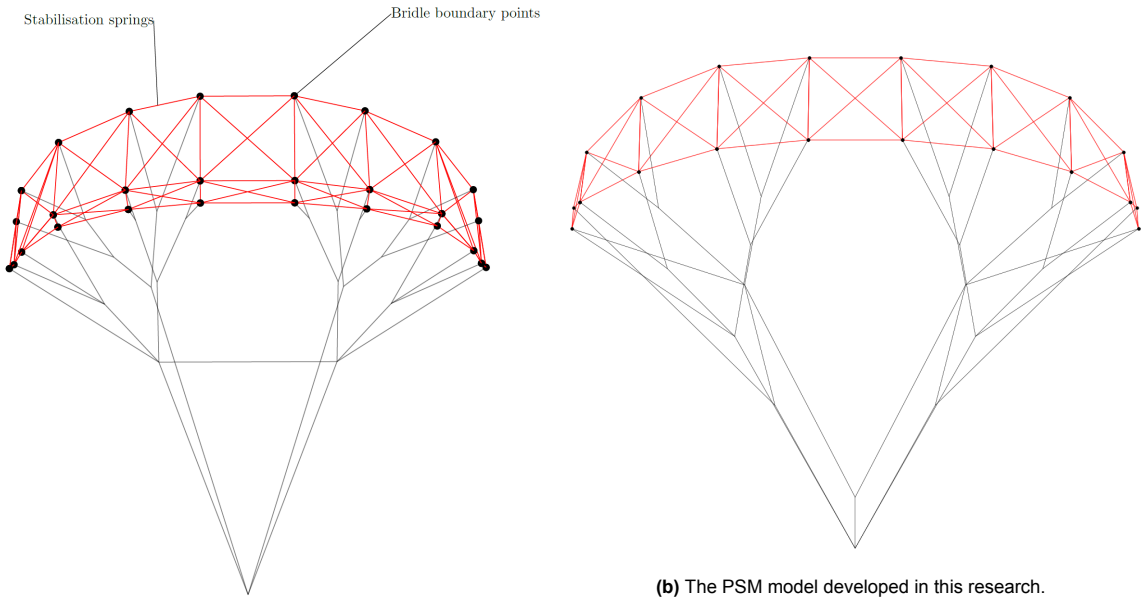

(a) Geschiere his model, where the horizontal line represents the compliant element [27].

(b) The PSM model developed in this research.

Figure 6.11: Dynamic PSMs, depicted in the same colours for ease of comparison.

All particles are attributed a unit mass. Furthermore, a damping term is added because the dynamic simulation must lose energy to reach a stable solution. The drag of the considered elements is neglected, based on its relative minor size compared to the force generated by the kite wing [10].

The incorporated spring stiffness and damping terms are non-physical making the PSM pseudo-physical. Non-physical parameters are needed for the dynamic simulation to remain stable during the transient phase, e.g. a lower than real spring stiffness is selected. As only the steady-state is of interest, transient phase effects are neglected, e.g. the friction of a line rolling over the pulley. The actual spring stiffness is of such magnitude that substantial stretching is unlikely. The solution criteria that the maximum stretching of the bridle must be below 0.25% in the powered CAD state is, therefore, adopted. The non-relevance of the unphysical transient phase combined with strict solution criteria, make that the pseudo-physical PSM its steady-state solution is considered physical.

The elements making up the particles (see Sec. 6.3.1), their new position is an outcome of a force equilibrium (see Sec. 6.3.2). The forces that together reach an equilibrium are the damping force (see Sec. 6.3.3), spring force (see Sec. 6.3.4) and lift force (see Sec. 6.3.5).

6.3.1. The particles

The vector $\vec{x}$ represents the location of all the particles in the PSM, which are the knots, pulleys and bridle attachments points to the kite wing (see Fig. 6.12). The latter represents the kite shape, where the kite wing segments edges are represented by elements with spring stiffness and a damping constant. This makes for the discussed wireframe 9-plate representation of the kite wing (see Sec. 5.2). Because the quadrilateral shape is not ‘stiff’, i.e. free to change its angles, additional diagonal elements are added to prevent shear (see Fig. 6.13). As a side note, the trilateration based models that have a wireframe without diagonals, hold their validity since one of the diagonals is used in the calculation and is assumed constant.

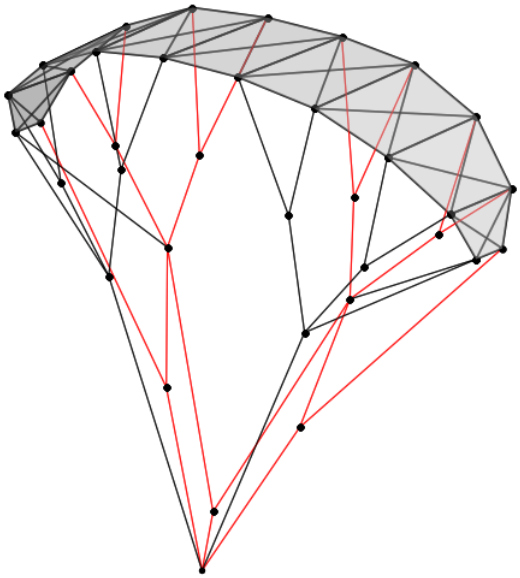

Figure 6.12: Orthogonal view of the PSM, where each dot represent a particle.

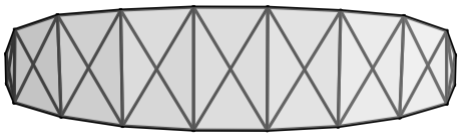

Figure 6.13: Top view of the PSM, where the diagonal kite wing plate elements are clearly shown.

6.3.2. Equations of motion

The dynamic simulation solves a force equilibrium for each particle in the system. The force equilibrium is based on Newton's 2^{nd} law and takes the general form of $\vec{F_r} = m\vec{\ddot{x}}$, where $\vec{F_r}$ is the resultant force, m the mass and $\vec{\ddot{x}}$ the acceleration. Because the particles have unit mass the form is reduced to $\vec{F_r} = \vec{\ddot{x}}$. Taken into account all the force components: spring stiffness ($\vec{F_s}$), damping force ($\vec{F_d}$) and lift force vector ($\vec{L}$) the equation of motion (EOM) becomes a 2nd order non-homogeneous differential equation (see Eq. 6.11).

$$\vec{\ddot{x}} = \vec{F_s} + \vec{F_d} + \vec{L} \tag{6.11}$$

The 2^{nd} order non-homogeneous differential equation can be reduced to a system of 1^{st} order coupled non-homogeneous differential equations. This reduction is achieved by introducing a parameter $\vec{q}$ representing the positions equal to $\vec{x}$ and $\vec{u}$ representing the velocities equal to $\dot{\vec{x}}$. One can represent the acceleration term ($\ddot{\vec{x}}$) by the two equations formed by the derivative of $\vec{q}$ and $\vec{u}$ (see Eq. 6.12).

$$\begin{aligned} \dot{\vec{q}} &= \vec{\dot{x}} \\ \dot{\vec{u}} &= \vec{F_s} + \vec{F_d} + \vec{L} \end{aligned} \tag{6.12}$$

The remaining system of 1^{st} order coupled non-homogeneous differential equations are so called 'stiff', i.e. difficult to numerically solve. An explicit solver known as the 'leap-frog method' was used but found too unstable when incorporating all particles. It was decided that an implicit solver method is needed for numerical stability reasons.

Implicit solvers generally require more computational cost per iteration compared to explicit solvers. The benefit is however that they are stable at much larger time steps. Leaving one with a trade-off decision, where for the PSM problem an implicit method was found best. The problem is solved using a module of Python called 'SciPy', in which the PSM is formulated as an initial value problem [63]. The selected solver is the 'Radau' solver, which implements an implicit Runge-Kutta method of the fifth-order [31].

6.3.3. Damping force

The linear viscous damping force term ($\vec{F_d}$) is a function of the velocity ($\vec{\dot{x}}$) and the damping constant (C) (see Eq. 6.13). Because the transient phase is not relevant the damping constant is not selected

through experiments, rather through a trial and error procedure. Its magnitude was set high enough to provide stability and low enough to allow movement of the points.

$$\vec{F_d} = -C\vec{\dot{x}} \tag{6.13}$$

6.3.4. Spring force

The spring force $\vec{F_s}$ is equal to the sum of all attached bridle lines and kite elements that are extended. The generated force is based on the spring stiffness (K) and the amount of extension ($\vec{\Delta l}$). The latter is represented by vectors because all particles are connected by multiple elements, each in their own direction (see Fig. 6.14). The amount of extension is calculated by taking the difference between two particles and subtracting the restitution length (l_0) (see Eq. 6.14). The spring stiffness is set equal for all bridles and selected through trial and error. This process was done while ensuring that the maximum line stretch in the design state ($u_p = 1$) is below 0.25% making its effect negligible.

To decrease numerical instability the spring force ($\vec{F_s}$) is modelled slightly different than merely a linear decrease for positive extensions. The function is translated to reach a value of one at $\vec{\Delta l}$ = 0 and when $\vec{\Delta l} < 0$ the spring stiffness approaches zero asymptotically (see Eq. 6.14). This makes the function smooth, hence decreasing numerical instability problems.

$$\begin{aligned} \vec{\Delta l} &= (l_{A,B} - l_{A,B_0}) \\ \vec{F_s} &= \begin{cases} -K\vec{\Delta l} + 1 & \text{if } \vec{\Delta l} \geq 0 \\ -1/(\vec{\Delta l} - 1) & \text{if } \vec{\Delta l} < 0 \end{cases} \end{aligned} \tag{6.14}$$

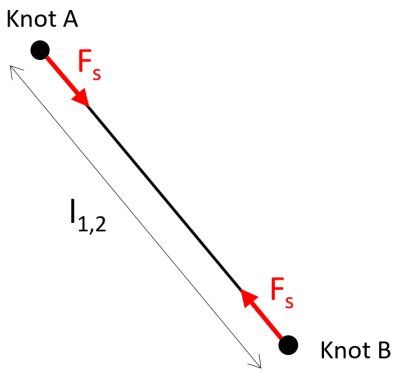

Figure 6.14: Spring force due to a line extension between two knots.

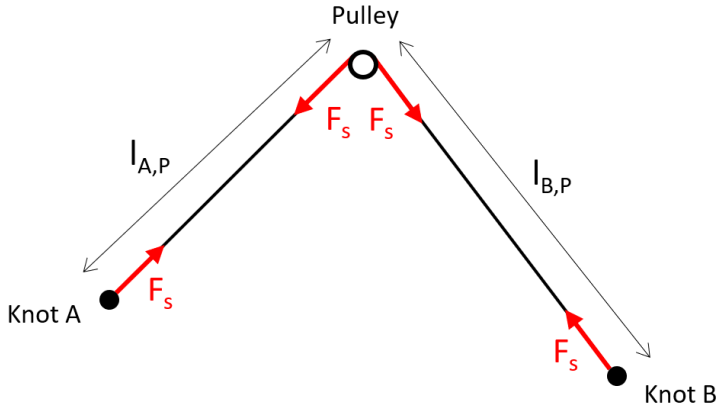

Figure 6.15: Spring force due to a line extending between two knots, that goes over a pulley.

Figure 6.16: Free body diagrams of the spring force (F_s).

The particles representing the pulleys are modelled separate from those that represent the knots because the line extension must be calculated differently. The bridle line is namely attached at knots and not at the pulley itself (see Fig. 6.15). The line extension determining the spring force is, therefore, calculated with respect to the total difference in distance, i.e. the sum of the current lengths ($[l_{A,P} + l_{B,P}]$) minus the sum of the restitution lengths ($[l_{A,P_0} + l_{B,P_0}]$) (see Eq. 6.15).

$$\vec{\Delta l} = \frac{[l_{A,P} + l_{B,P}] - [l_{A,P_0} + l_{B,P_0}]}{[l_{A,P_0} + l_{B,P_0}]} \tag{6.15}$$

6.3.5. Lift force

The vector $\vec{L}$ represents the lift force and is filled with zeros for all the entries representing the knots and pulleys. Only the particles representing the bridle line attachment points, i.e. the corners of the

9-plate representation of the kite wing, are given a non-zero plate lift ($\vec{L_p}$). $\vec{L_p}$ is calculated per plate and is applied to each relevant particle in the outwards perpendicular direction (see Fig. 6.17). This is achieved by multiplying $\vec{L_p}$ with the unit vector normal to the plate, calculated by taking the cross product of the two diagonals of the respective plate. Updating the orientation of $\vec{L_p}$ with each iteration ensures that the effect of panel rotations are taken into account. $\vec{L_p}$ is assumed to act in the middle of the plate. The distribution of $\vec{L}$ on each corner point is therefore assumed uniform locally in both chord-wise and span-wise, hence each corner point is attributed 25% of $\vec{L_p}$ of the respective panel.

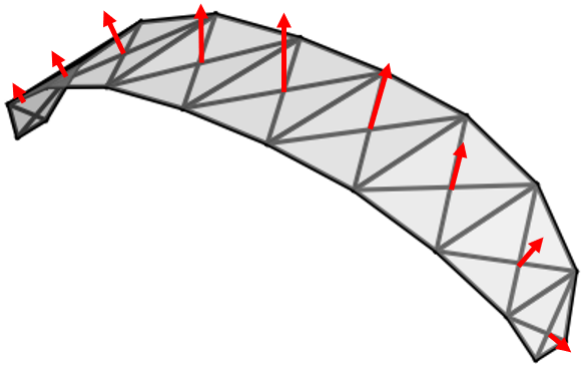

Figure 6.17: 9-plate wing model, where the red arrows indicate each lift vector ($\vec{L_p}$) perpendicular to its respective panel.

$\vec{L_p}$ is multiplied by a factor to simulate a more accurate non-uniform spanwise loading condition. The factor should represent the lifting conditions of the kite wing, which therefore should follow the general lift-force equation (see Eq. 6.16). The general lift-force equation is based on the density (ρ), the surface area (S), the apparent velocity ($\vec{v_a}$) and the lift coefficient (C_L). From these parameters, the relevant change per kite wing segment is governed by: S, C_L and $\vec{v_a}$.

$$\vec{L} = \frac{1}{2}\rho S \vec{v_a}^2 C_L \tag{6.16}$$

The change in $\vec{v_a}$ is dependent on the current flight direction of the kite with respect to the wind velocity vector ($\vec{v_w}$). Because the flight path is not simulated, the change can't be taken into account. The change in S can be used as a factor and is calculated using Brahmagupta's formula (see Eq. 6.17) [43]. The edge lengths of the plate ($l_{edge,i}$) are used to calculate the semi-perimeter (s), which is used to calculate S. To not alter the order of magnitude of $\vec{L}$, S is non-dimensionalized.

$$\begin{aligned} s &= \frac{1}{2}\sum_{i=1}^{4} l_{edge,i} \\ S &= \sqrt{(s-l_{edge,1})(s-l_{edge,2})(s-l_{edge,3})(s-l_{edge,4})} \end{aligned} \tag{6.17}$$

The wind velocity vector $\vec{v_w}$ is assumed to stay constant and parallel to the (x, z) plane hitting the middle chord of the kite wing at an angle of $10\,°$ (see Fig. 5.5b). This enables the formulation of the change of effective inflow angle for each plate, calculated with respect to a vector representing the middle chord of each plate ($\vec{c_{m,i}}$). By assuming that C_L scales as a flat plate would do in its linear part of the lift-polar, i.e. by $2\pi \sin(\alpha)$, the change of C_L can be taken into account. Because the kite wing is subject to an anhedral angle, the effective inflow angle is calculated in both the (x, z) and (x, y) plane. The lift scaling factor (L^*), therefore, becomes a function of both the angle of attack (α) and the side-slip angle (α_s). The respective effects of both angles are multiplied by the orientation of the LE of the plate (see Eq. 6.18), expressed as unit vector ($\vec{LE_i}$). To not change the order of magnitude of $\vec{L}$, the lift scaling factor (L^*) is non-dimensionalized before multiplying.

$$L^* = |\vec{LE_{i,y}} \sin(\alpha)| + |\vec{LE_{i,z}} \sin(\alpha_s)| \tag{6.18}$$

Including the scaling of $\vec{L_p}$ based on the effective inflow angle has an additional benefit when actuating the wing asymmetrically. The resultant lift vector namely tilts to the side upon experiencing the turning input, both in flight and within the simulation environment. The result of the tilt is a change in panel orientation, meaning that in the next time step the lift-vector will tilt even more. Without a counteracting force, the result is a kite wing that keeps rotating around the origin. Leaving one with a simulation that would never reach a stable solution. By including orientation based scaling the $\vec{L_p}$ of the panels tilting to the side reduces, causing a dynamic stabilisation of the kite wing.

7

Results

Several wing models and bridle line system representations have been developed. To assess the accuracy the models will be compared based on the width change for different power settings. The comparisons with other models serve as verification and the comparisons with the photogrammetry results as validation. Besides accuracy, the computational cost of the models is compared based on run times. The run times were obtained using code that is not optimised and a laptop with a single processor, that has a processor base frequency of 2.7 GHz.

First, the triangular 2-plate model, used mainly for verification shall be discussed (see Sec. 7.1) followed by the effect of adding TE bridles and an additional plate (see Sec. 7.2). Furthermore, the effect of including more plates and using non-uniform actuation is discussed (see Sec. 7.3). The results for the 9-plate kite wing representation, modelled using the PSM, are discussed last (see Sec. 7.4).

7.1. Triangular 2-plate model

The 2-plate triangular wing model is simulated using the tetrahedron algorithm, trilateration algorithm and the PSM. The output of the three models is plotted together with the photogrammetry results showing the predicted kite width for different power settings (u_p) (see Fig. 7.1). The same behaviour of increasing width for increasing power setting is observed, but the steepness of the slope and magnitude of the width differs. This could be caused by the extension of the imaginary line and the simplified representation of the kite, which combined seem to overpredict the amount of deformation. Other factors contributing to the discrepancy could be caused by not including ballooning, incorrect geometric input and incorrect actuation relations. In the powered state ($u_p = 1$) all lines end at the same point, which they should because that is the design width upon which the models are built.

Comparing the models, one observes that both tetrahedron and trilateration predict the exact same output. Considering their purely geometric nature this should be the case, thereby verifying both models. The tetrahedron and trilateration algorithm both show a run time below 1 ms, whereas the PSM runs in 2.5 s. The large difference in run time is attributed to the non-geometric nature of the PSM. It should, for small convergence criteria, still give roughly the same results as the geometric models do. That all three models predict about the same width, therefore verifies the correct working of each code. The only relevant difference is observed for u_p < 0.1, where the width prediction of the PSM is slightly higher. This is attributed to several reasons, discussed along with the rest of the PSM its results (see Sec. 7.4).

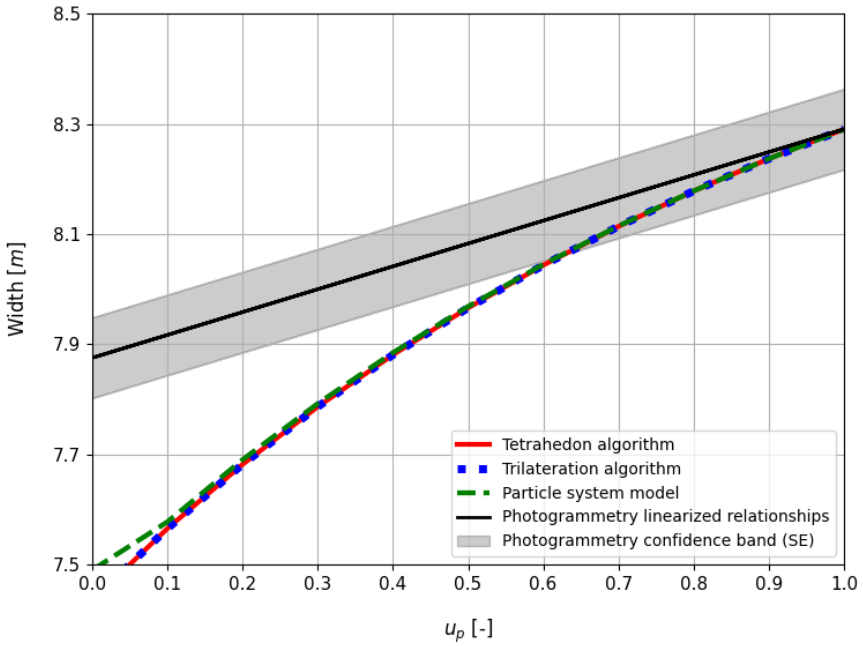

Figure 7.1: Photogrammetry results for the width changes, plotted together with the simulation results of the 2-plate triangular model calculated using the trilateration and tetrahedon algorithms.

The trilateration algorithm calculates coordinate changes, allowing one to compare a 3D render of the shape in the depowered state to the shape in the powered state (see Fig. 7.2). Upon a symmetrical actuation input, the plates hinge over the middle LE point. The angle of the middle chord line with respect to $\vec{v_w}$ decreases, i.e. the angle of attack decreases. With a lower angle of attack, less force is produced, which matches the depowering goal of a depower tape extension.

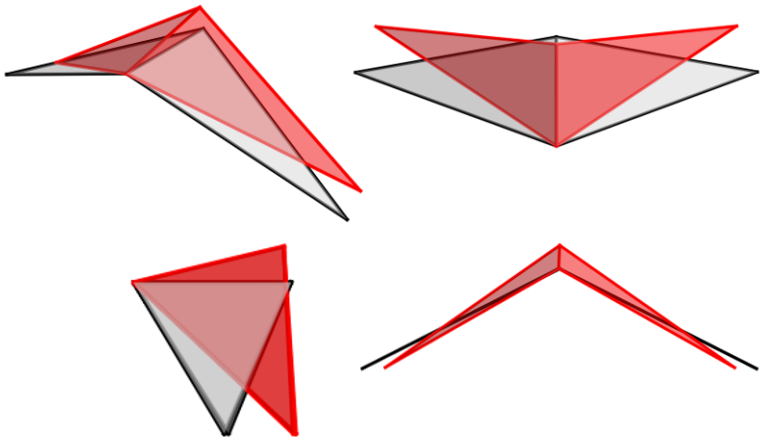

Figure 7.2: 2-plate triangular subject to a symmetrical deformation, calculated using the trilateration algorithm. In black the shape for u_p = 1 and in red the shape for u_p = 0. The figure shows an orthographic view in the top left, a top view in the top right, a side view in the bottom left and a front view in the bottom right.

7.2. Quadrilateral 2-plate and 3-plate model

The uniformly actuated 2-plate and 3-plate quadrilateral wing models their shape changes are calculated using the trilateration algorithm. They differ in the detail they include and in that the 3-plate model does not require the use of an imaginary line attached to the middle TE point. The resulting width predictions of both models are close in terms of behaviour and magnitude (see Fig. 7.3). The inclusion

of an additional panel does thus not seem to have a large effect on the predicted deformation. Furthermore, both models have run times below 1 ms.

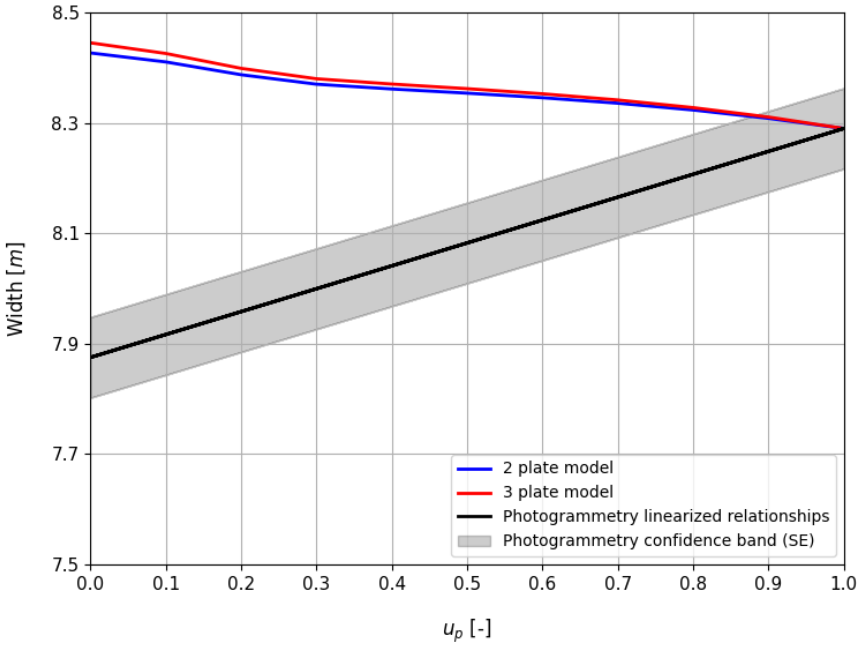

Figure 7.3: Photogrammetry results for the width changes, plotted together with the simulation results of the 2-plate and 3-plate quadrilateral model calculated using the trilateration algorithm.

The simulated behaviour is the opposite of the observed photogrammetry behaviour. The most likely cause is the uniformly actuated TE. Because when using the same line length extension for the bridle lines of different lengths, the relative difference of the lines differs. As the outer points are closer to the KCU than the middle points are, the outer points are actuated relatively more (see Fig. 7.4 and 7.5). The predicted kite width, therefore, increases rather than decreases. This indicates a major deficiency of the uniformly actuated models and that this modelling procedure is inaccurate.

The shape deformation in 3D confirms the inaccuracy, by displaying nonphysical behaviour. The upward rotations of the tips tilt the outer plates into the wind direction, whereas in reality, one expect the plates to rotate back due to the pressure force.

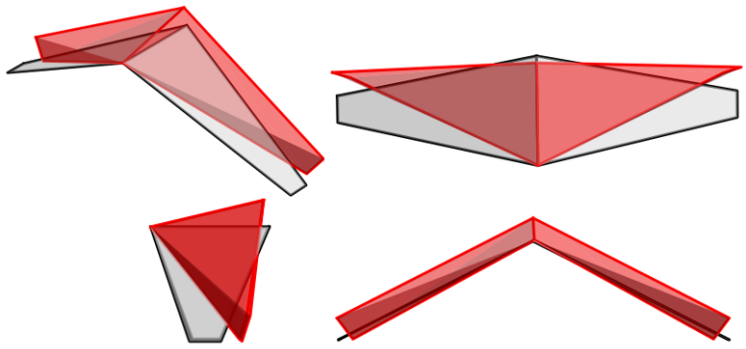

Figure 7.4: 2-plate quadrilateral subject to a symmetrical deformation, calculated using the trilateration algorithm. In black the shape for u_p = 1 and in red the shape for u_p = 0. The figure shows an orthographic view in the top left, a top view in the top right, a side view in the bottom left and a front view in the bottom right.

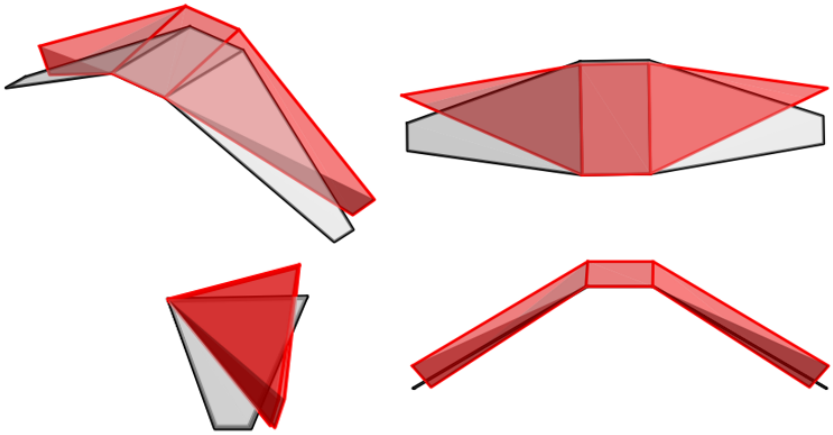

Figure 7.5: 3-plate quadrilateral subject to a symmetrical deformation, calculated using the trilateration algorithm. In black the shape for u_p = 1 and in red the shape for u_p = 0. The figure shows an orthographic view in the top left, a top view in the top right, a side view in the bottom left and a front view in the bottom right.

7.3. Quadrilateral 7-plate model

The quadrilateral 7-plate model is actuated non-uniformly using empirical relations for the pulley and knot positional change as a function of the power setting. The trilateration algorithm is used to calculate the positions of the bridle line attachment points from the modelled knots and pulleys. Furthermore, the model has been developed with and without ballooning, both for $\Delta l_d = 8\%$ depower tape difference between the powered and depowered state and for $\Delta l_d = 13\%$. All four models show the same increase in kite width when increasing u_p (see Fig. 7.6), a similar trend as was observed in the photogrammetry analysis. Furthermore, all four models have a run time of about $2\,\text{ms}$ they are, therefore, the slowest of the developed geometric models.

The slope and depower width of both models without ballooning are slightly lower than those including ballooning, indicating the global effect in width the sum of local changes in TE length has. The model that shows the smallest discrepancy between linearized photogrammetry results and model prediction is the model with $\Delta l_d = 13\%$ that includes ballooning. The results based on $\Delta l_d = 8\%$ are included to demonstrate the sensitivity of the minimal and maximal states of the depower tape. Looking at the results it becomes evident that clear differences are present, i.e. the model is sensitive to the amount of depower tape change. When assuming that the photogrammetry results are correct, it can be concluded that using the differences obtained from the measurements done in 2017, leads to more accurate results.

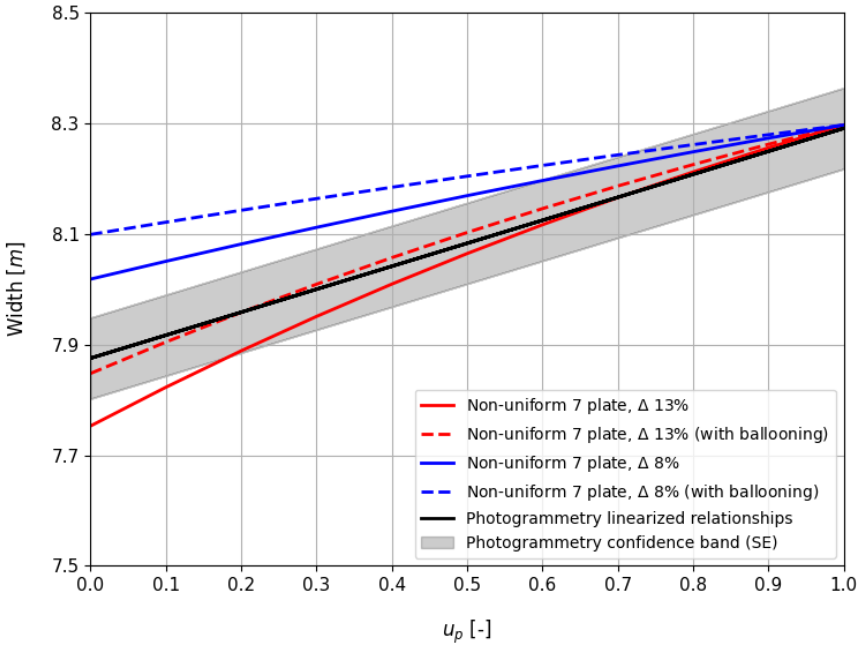

Figure 7.6: Photogrammetry results for the width changes, plotted together with the simulation results of the 7 quadrilateral plate model calculated using the non-uniform trilateration algorithm.

The large increase in prediction accuracy compared to the previously described models can not be attributed to the included number of plates. A uniform actuated quadrilateral 9-plate model was namely developed, which for u_p > 0.4 indicates the opposite of the desired behaviour and for u_p < 0.4 finds no solution. The conclusion is drawn that modelling the actuation input non-uniformly must be the reason for the increased accuracy. Including more physical details, by taking into account ballooning, also brings the solution closer to the photogrammetry results for the $\Delta l_d = 13\%$ model. Providing arguments for the correctness of both the photogrammetry results and the model results, because including more empirical data should bring the simulation closer to the experiments.

Flaws of the non-uniform PSM arose mainly from its inability to deal with slacking bridles. It therefore can not predict asymmetric deformation, model an accurate 9-plate wing model representation or non-uniform actuation without additional empirical relations. These limitations cause problems for the modularity and accuracy and hence the potential of the model as a building block.

The deformations of the 7-plate model look more natural (see Fig. 7.7) than the uniformly actuated models did. The tips of the outer plates don't rotate far upwards, the deformation seems gradual and most pronounced in the middle section, which is as expected considering the most force is produced there.

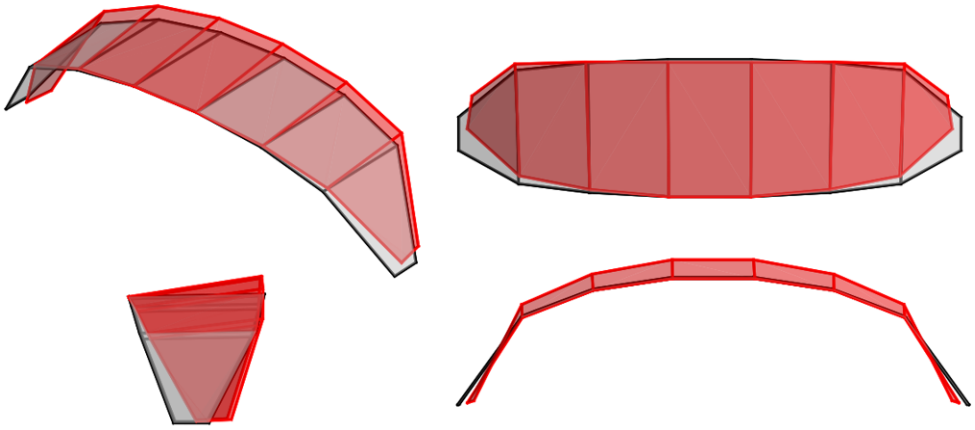

Figure 7.7: 7-plate quadrilateral subject to a symmetrical deformation, calculated using the non-uniform trilateration algorithm and $\Delta l_d = 13\%$. In black the shape for u_p = 1 and in red the shape for u_p = 0. The figure shows an orthographic view in the top left, a top view in the top right, a side view in the bottom left and a front view in the bottom right.

7.4. Quadrilateral 9-plate model

The quadrilateral 9-plate wing model connected to all bridle lines and actuated both symmetrically and asymmetrically using the PSM is the most complex model developed in this research. The model has been developed with and without ballooning, both for $\Delta l_d = 8\%$ difference between the powered and depowered state and for $\Delta l_d = 13\%$. All four models their results display the correct behaviour (see Fig. 7.8). The PSM models have a run time of about $40\,\text{s}$, which is on the slow side for the desired optimisation purposes. Slow because one wants to be faster than real-time, which for actuation induced deformations is roughly $10\,\text{s}$ (see Sec. 2.1.1) [40]. The expectation is however that one could drastically reduce the run time by using more efficient coding and more processing power.

Both $\Delta l_d = 8\%$ and $\Delta l_d = 13\%$ are included to illustrate the sensitivity of the model to the amount of depower tape length change. Including ballooning has roughly the same effect on both. For higher power settings, ballooning reduces the predicted width and for lower power settings it increases the predicted width. The geometric non-uniform 7-plate model displayed a steady increase in predicted width when including ballooning. The difference with the PSM is attributed to it being a force-based method, which introduces all kinds of non-linear effects that could cause the initial decrease in width.

Assuming that the photogrammetry results are correct, the best PSM results are found for $\Delta l_d = 8\%$ instead of the $\Delta l_d = 13\%$ that was found for the non-uniform 7-plate model. Regarding the including or excluding of ballooning, the model including ballooning is considered slightly better. The difference is, on average, 0.27% away from the photogrammetry results and always within 0.7%. The fact that the non-uniform 7-plate model displays more accurate results for $\Delta l_d = 13\%$ whereas the PSM does for $\Delta l_d = 8\%$, indicates errors must be present in either one of the models.

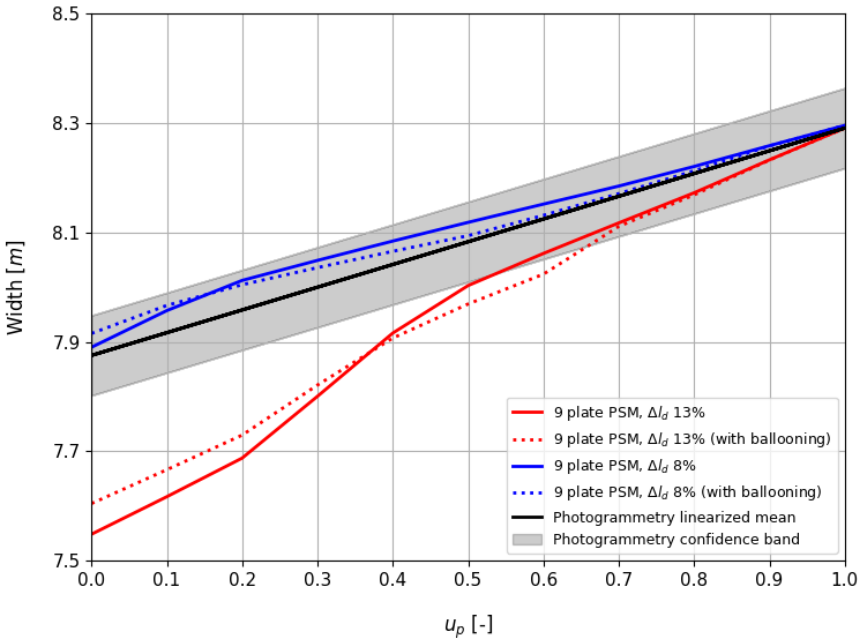

Figure 7.8: Photogrammetry results for the width changes, plotted together with the simulation results of the 9 quadrilateral plate model calculated using a PSM.

The symmetrical actuated PSM prediction of the shape deformations (see Fig. 7.9) look similar to the quadrilateral non-uniform 7-plate outcome. The observed slacking lines, which made it infeasible to model more bridles geometrically, do not necessarily show in the results. The maximum amount of slack in the depowered state is namely below 0.1%. It was furthermore confirmed that the maximum stretched bridle was below the upfront set parameter of 0.25%.

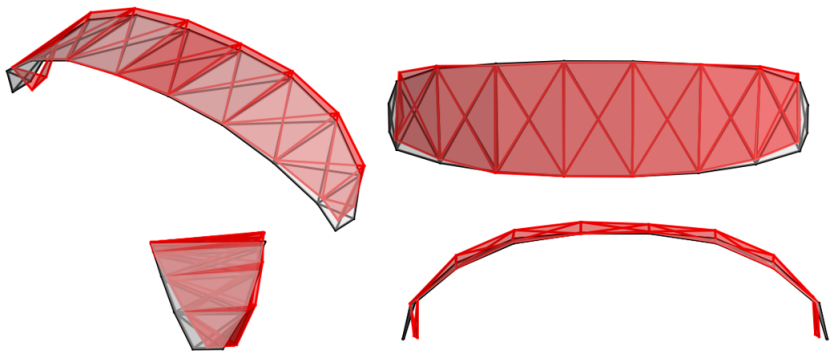

Figure 7.9: 9-plate quadrilateral subject to a symmetrical deformation, calculated using the PSM and $\Delta l_d = 8\%$. In black the shape for u_p = 1 and in red the shape for u_p = 0. The figure shows an orthographic view in the top left, a top view in the top right, a side view in the bottom left and a front view in the bottom right.

A qualitative observation, confirming the model its validity, comes from the similarity between the simulated inward bending of the tips and that observed during the photogrammetry analysis (see Fig. 4.3 and 7.10).

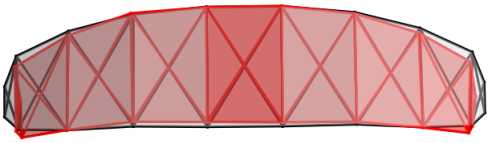

Figure 7.10: 9-plate quadrilateral subject to a symmetrical deformation, calculated using the PSM and $\Delta l_d = 8\%$. In black the shape for u_p = 1 and in red the shape for u_p = 0. A bottom view is shown, from a similar angle as the footage was shot, which shows the inward bending of the tips.

Asymmetric deformation can not be validated without proper validation data, therefore, a qualitative assessment is made. The expected twist is present, the steered kite tip (right side) has moved forwards and the non-steered side has moved aft (see Fig. 7.11). The forwards moving side has increased its angle of attack, whereas the backwards tilting side has decreased its angle of attack. This will lead to more force generation for the forward side, leading to the desired moment that enables turning. The photogrammetry analysis showed slack, therefore, the expectation was that the PSM find slack as well. A similar amount of slack is, however not present. The maximum observed slack is below 0.1%, hence indicating that some aspect of this representation is incorrect.

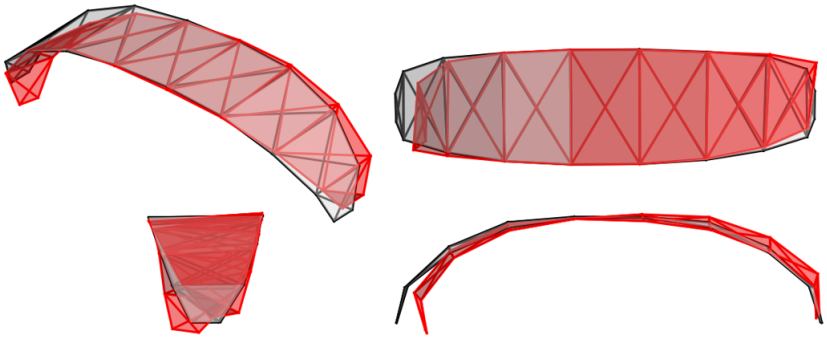

Figure 7.11: 9-plate quadrilateral particle system based asymmetrical deformation. In black the shape for u_s = 0 and in red the shape for u_s = 0.5. The figure shows an orthographic view in the top left, a top view in the top right, a side view in the bottom left and a front view in the bottom right.

7.4.1. Discussion

The discrepancies between the kite wing plate representations calculated using the particle system algorithm and the photogrammetry observed behaviour under actuation input could be caused by a multitude of reasons.

Because the bridle line lengths have been obtained using a reversed engineering process, errors are likely to be present. Furthermore, the initial coordinates likely do not correspond closely to the shape in the powered state during the measurement campaign in 2017 [38].

The relations between actuated bridle line length and actuation settings have been obtained from analyzing experiments. For $\Delta l_d = 13\%$ data sets were used that should correspond to the flight days of the footage this, however, has not been confirmed. Therefore, it is not unlikely that the obtained actuation relations are incorrect. To study the potential effect of errors, the sensitivity was analyzed by performing simulations with $\Delta l_d = 8\%$.

The spring stiffness (K) and damping term (C) have been selected by trial and error. This was done under the assumption that for strict stretching conditions, they should only impact the transient phase. As with all assumptions, this might be incorrect and could, therefore, introduce errors.

Another reason for errors is that it is likely that the applied loading distribution in both span and chordwise direction, is incorrect. The potential errors are caused by not modelling the aerodynamics accurately, therefore, relevant effects are left out. General viscous effects are not modelled, which occur

during flight because separation is always present for LEI kites [7, 38]. Separation is not only present but also relevant. Newman et al. and Smith et al. went as far as stating that the difference between aerodynamic simulations and experiments is largely caused by not modelling separation [44, 64]. Another relevant not modelled effect is 3D crossflow. Therefore accurate aerodynamic modelling requires either a 3D model or 3D corrections [14]. One of the factors causing 3D flow is caused by the pressure side and suction side meeting one another at the tips. This causes a tip vortex, that induces 3D cross flow and a reduction of the loading by lowering the pressure difference. Not including these effects causes a discrepancy between the real and modelled loading distribution, mainly spanwise. Besides the magnitude of the lift force, the uniform chordwise application is prone to change for different flight settings. Hummel et al. tested multiple LEI kites and found the force ratio between LE and TE bridles to change from roughly 0.1 to 0.5 [33]. Not taking into account the changes in chordwise loading distribution is another relevant factor that is potentially introducing errors.

8

Conclusions and recommendations

Improving the aerodynamic performance of a soft wing membrane AWES kite is complex, mainly due to the deformations occurring during flight. The deformations are relevant and can not be neglected because they alter the aerodynamic characteristics, allowing efficient operation. The kite is controlled through actuation inputs, asymmetric actuation for example makes the kite turn. Novel structural models that can assess the main deformations modes have, therefore, been developed. To evaluate the accuracy and validity of the models, data was extracted using photogrammetry. The research efforts have brought concluding answers to the research questions (see Sec. 8.1). Furthermore, several research opportunities have been identified, which are formulated as recommendations for future studies (see Sec. 8.2).

8.1. Conclusions

The research goal was to assess the aeroelastic deformation effects on a soft wing membrane kite by developing a structural model. First, data governing the deformations and other empirical relations were retrieved (see Ch. 4). The V3 LEI kite wing was represented by plates, which are described by the bridle line attachment points (see Ch. 5). The wireframe wing models were coupled to different bridle line system models that describe the bridle line attachment point changes upon an actuation input (see Ch. 6). Lastly, a comparison was made between the simulations and the photogrammetry results. This section serves to highlight the main conclusions from this research by answering the research questions in line.

A photogrammetry analysis of the V3 was performed, using camera footage of the KCU in flight. Distortion effects are caused by: the type of camera lens, angle changes and line-of-sight length changes. The distortion effects are relevant due to the perspective nature of the image and several assumptions were needed to remove them. Straight flight results showed reasonable agreements over the taken samples, indicating that the existing random errors were not problematic. It was decided that the uncertainty of the straight flight results for the bridle tip-to-tip width changes was low enough to be used as validation data. For turning flights, however, the distortion effects caused high uncertainties, which made the quantitative result, for the small sample set, too inaccurate. Ballooning of the canopy on the TE is a function of the amount of loading. Therefore, the expectation was that it would change depending on the power setting. This behaviour was confirmed and linearised to form an empirical relationship needed for the developed structural model.

Structural models able of predicting deformation as a function of actuation were developed under the hypothesis that: ‘by modelling the changes of bridle line system attachment points and empirical ballooning relations, one can predict the deformation of the kite’. A wireframe representation of the tubular frame of the wing segment was used to model the kite wing. Each segment of the wireframe forms a plate, with each corner point representing a bridle line system attachment point. From the results, it was concluded that a purely geometric model is not accurate enough. Extending the geometric models by including empirical relations, made the non-uniform 7-plate model with a trilateration algorithm

the best geometric model. This confirms that non-uniform actuation is a better representation of the in-flight behaviour. Two different depower tape changes were used as input, to study the sensitivity and because it is uncertain which is a better representation. The best results were found for the model using $\Delta l_d = 13\%$. In both cases, including local ballooning was found to increase the global width.

In straight flight, two slacking bridles were found. By removing the accompanying plate on each side this problem is resolved. A 7-plate model was therefore developed instead of a 9-plate model. In the qualitative photogrammetry analysis of the turning flight, it was found that another bridle line slacks, making that even a 7-plate representation does not suffice. Developing a different non-uniform bridle line representation by not modelling a certain plate was infeasible this time, because the slacking line is attached to the tip, which must be modelled. A PSM was developed that can deal with slacking lines and the full complexity of the bridle line system, without needing empirical relations. This is possible because it is a dynamic model that finds a force equilibrium for which only its steady-state solution is considered relevant. The sensitivity is again studied and found to be higher compared to the non-uniform 7-plate model. The difference in sensitivity is attributed to the 0.25 factor with which the depower tape input of the 7-plate model is multiplied. The predicted width change of the PSM that uses $\Delta l_d = 13\%$ shows the best results, whereas the width predictions for $\Delta l_d = 8\%$ are too low. Assuming that the photogrammetry results are correct, the differences are mainly attributed to modelling incorrect bridle lines, starting from the wrong initial shape and using inaccurate loading conditions. Unlike the other developed models, the PSM can deal with asymmetric actuation input.

With a run time of about 40 s, the PSM is the most expensive. Second, comes the non-uniform 7-plate model with a run time below 2 ms. Based on the width change prediction accuracy under symmetric actuation, the non-uniform 7-plate model is the most accurate for $\Delta l_d = 13\%$. The PSM is the most accurate for $\Delta l_d = 8\%$, where the results agree within 1% to the photogrammetry results. Besides symmetric deformation, the ability to predict asymmetric deformation is key. Taking this into account, the PSM is considered better at providing an overall accurate representation of the deformation of the kite. Furthermore, the PSM is the most modular because it can run without using empirical relations. This is possible as it uses a force-based approach which allows the necessary bridle line slack. The PSM is therefore considered the best and most useful building block for a FSI model.

Concluding, it is found possible to model the main aeroelastic deformation modes using a fast structural model based on actuation inputs. The PSM can model slacking bridles, does not need empirical relations, is easily coupled to an aerodynamic model and hence shows the greatest potential. Using the research insights and the PSM as a building block, a foundation for the next generation of design models of soft wing membrane kites is formed.

8.2. Recommendations

The identified high-level goal for this research is to increase the energy yield of AWES by improving aerodynamic performance. This research has focused on the development of a building block for a FSI module of a design model with which one could perform iterative shape optimisation procedures. As input for the model, the design specifications used during the experiments of 2017 needed to be determined. Not all details were retrieved, therefore some had to be reconstructed. In future work, it would be more accurate to use the precise measured bridle lengths. Besides these lengths, the coordinates describing the shape of the kite were extracted from the CAD drawings in 2012 and used as inputs. The CAD shape is, however, likely not equal to that observed in powered flight, which was however assumed. For future work, it would be recommended to develop a method with which one could determine the precise shape of the kite during flight. Such data could be used to validate the similarity of the CAD shape to the flown powered shape.

In this research, photogrammetry was used to obtain validation data. Photogrammetry has some shortcomings and several assumptions were needed to remove the distortions. In future research, one should: take more samples to reduce random errors, identify both up and downwards flight, average the results to remove the KCU gravity-induced swing, let different researchers analyze the samples to improve intra observed reliability and other practices to increase the reliability of the results. Besides

one camera-based photogrammetry, one could use two cameras preferably without a wide-angle lens to reduce distortions. By using such a test setup one might get up to an accuracy level that would leave one with useful turning results. This would improve the general quality of the research since one could quantitatively assess the accuracy of the predicted asymmetric deformation.

Alternatively, one could develop a novel method or use a different existing one to obtain shape information during flight. One could for example use inertial measurement units that know their relative position to one another [34]. Sticking enough of them onto the kite and flying pumping cycles with it, would leave one with a relatively accurate representation of the kite shape. An example of a novel method could be to use a 3D laser scanning technique, known for its ability to make relative accurate 3D representations of objects by measuring laser reflections [65]. Attaching a 3D laser scanning device onto the KCU seems the best option because the kite is always visible from that perspective, i.e. no further tracing activities would be required. When doing such measurements, ideally the measurement setup would also be airborne, enabling one to link inflow conditions to the observed deformations. This would remove the need to linearize the behaviour between the approximate maximal and minimal states, which would allow for assessing the multi-variable non-linear relations between kite shape and flow conditions. These relations are considered key towards further validation efforts.

Regarding the structural representation of the kite wing, the best method is the PSM since it can deal with a 9-plate representation of the kite. Furthermore, the model opens up possibilities for improvements and easy extrapolation to other shapes. One could increase run times by coding more efficiently and improve accuracy by including more details, e.g. use a particle system representation of the tubular frame [37]. Another way of approaching the tensile membrane structure problem is through a force density method, used previously to analyze the Munich stadium [55]. Further research could compare the methods to see which provides a higher accuracy to computational cost ratio. For visualisation and reference frame consistency purposes, the models had their LE points remain in place. Future research could investigate the effect of these assumptions. For the three or more plate models one could restrict the movement of only one LE point in the middle of the kite, instead of both LE points of the middle plate. Because restricting two points limits the movement more than restricting one point, restricting only one point is expected to lead to an increase in accuracy.

The ballooning of the TE is now modelled using empirical relations. In reality, it is a function of the wing loading acting on the canopy. If one were to use a structural model that takes force as an input, a force-based ballooning relation could be developed. This would alleviate the need for empirical relations allowing easier extrapolation to other kite shapes, hence increasing modularity. A force-based structural model would require an aerodynamic model. Several research efforts have been made in this regard for LEI kites in general, but also for the V3 specifically. Because of the relevance of the aerodynamic model, the identified points of key importance from literature and several discussions with kite designers will be briefly discussed here.

The requirements for an aerodynamic model suited for a design model are that it must be fast and take into account the relevant phenomena. The former leads to lower fidelity modelling procedures, which means assumptions must be made. For the general use of LEI kites, the Mach number is low enough to assume an incompressible flow outside of the boundary layer [40]. The inviscid flow assumption does not fully represent the flow due to the presence of multiple separation regions, which are viscous phenomena [24]. The difference in the order of magnitude between frequency modes (see Sec. 2.1.1) makes that a quasi-steady-state assumption can hold, i.e. neglecting sub-scale frequency modes does not induce large inaccuracies [35]. Turbulent flow regions were found for the LEI kite, attributed to the surface roughness at the LE causing transition [24]. Furthermore, 2D modelling is not accurate enough, because strong 3D cross flows have been observed [14].

Outside of the boundary layer, one could use an inviscid and irrotational flow assumption [40]. To take into account separation and transitional effects, one could couple this model to a boundary layer model which operates without these assumptions or use corrections to represent the viscous and turbulent effects. The best models considering the low-computational cost requirements, therefore, seem 3D potential flow methods coupled to 2D boundary layer methods, where a method that can predict chordwise

load distributions would be the most useful for a FSI model. Research opportunities lie in developing such a model and investigating wake interactions effects, of which relatively little is yet known. Furthermore, one could verify whether the lift vector tilt of the developed PSM matches the tilt observed during flight due to an asymmetrical actuation input [47]. Chordwise tilting occurs as well and should be incorporated in future work to increase model accuracy [33].

With proper validation data, a structural model, a fast aerodynamic model and a way of coupling the two one should start developing a way of simulating the kite flight path. One could either test the design on an experimentally obtained flight path or develop a flight dynamic model with a controller. The latter would obtain the flight path per design and with it the energy production that the new shape enables. Furthermore, tether slack affects the incoming angle of the tether, which in turn influences the inflow angle at the kite. The inflow angle has a large effect on the force production, therefore, the model should include tether slack [47]. The deformations of the shape will affect the centre of mass and moment of inertia, the significance of these changes should be assessed. Modelling the wind velocity should be addressed because too simplistic wind models, e.g. assuming wind acts only parallel to the earth surface, lead to inaccurate results [68]. The model should also include gravity because besides actuation, this is the main factor driving inflow angle changes during flight [47].

Furthermore, aerodynamic damping must be taken into account to reach a stable solution. Adding artificial damping to resolve the stability issues does not suffice, because it results in an incorrect representation of the in-flight behaviour [27]. The current damping term, spring stiffness and lift force magnitude are all tuned to get to steady-state fast. Future work should investigate if incorporating the correct terms based on the material properties and the aerodynamic model, increases the accuracy of the prediction. The bridle line system is now modelled to start from a point. In reality, not all lines attach at the same point. Furthermore, there is an asymmetry because the wheels actuating the kite are not centred, i.e. the steering wheel is on the left and the depower wheel on the right [53]. The effect of the asymmetry could be analyzed in future research.

References

[1] Kitepower B.V. [V3 test flights]. [Unpublished raw data]. (2017).

[2] P. Bechtle et al. “Airborne Wind Energy Resource Analysis”. In: *Renewable Energy* 141 (Oct. 2019), pp. 1103–1116. DOI: 10.1016/j.renene.2019.03.118.

[3] J. Berens. “Dynamic Nonlinear Aeroelastic Behaviour of Flexible Wings in an Airflow”. MSc Thesis, Delft University of Technology, Mar. 20, 2015.

[4] R. den Boer. “Low speed aerodynamic characteristics of a two dimensional sail wing with adjustable slack of the sail.” Tech. Rep. LR-307, Delft University of Technology, 1980.

[5] H.A. Bosch. “Finite Element Analysis of a Kite for Power Generation”. MSc thesis, Delft University of Technology, The Netherlands, 2012.

[6] A. Bosch et al. “Nonlinear Aeroelasticity, Flight Dynamics and Control of a Flexible Membrane Traction Kite”. In: *Airborne Wind Energy*. Ed. by U. Ahrens, M. Diehl, and R. Schmehl. Green Energy and Technology. Berlin Heidelberg: Springer, 2013. Chap. 17, pp. 307–323. ISBN: 978-3-642-39964-0. DOI: 10.1007/978-3-642-39965-7_17.

[7] A. Bosch et al. “Dynamic nonlinear aeroelastic model of a kite for power generation”. In: *Journal of Guidance, Control and Dynamics* 37.5 (2014), pp. 1426–1436. DOI: 10.2514/1.G000545.

[8] J. Breukels. “An Engineering Methodology for Kite Design”. Phd Thesis, Delft University of Technology, The Netherlands, 2011.

[9] J. Breukels et al. “Aeroelastic Simulation of Flexible Membrane Wings based on Multibody System Dynamics”. In: *Airborne Wind Energy*. Ed. by U. Ahrens, M. Diehl, and R. Schmehl. Green Energy and Technology. Berlin Heidelberg: Springer, 2013. Chap. 16, pp. 287–305. ISBN: 978-3-642-39964-0. DOI: 10.1007/978-3-642-39965-7_16.

[10] A. Candade et al. “Structural Analysis and Optimization of a Tethered Swept Wing for Airborne Wind Energy Generation”. In: *Wind Energy* 23.4 (Jan. 8, 2020), pp. 1006–1025. DOI: 10.1002/we.2469.

[11] S. Costello et al. “Analysis of the maximum efficiency of kite-power systems”. In: *J. Renewable Sustainable Energy* 7 (2015). DOI: https://doi.org/10.1063/1.4931111.

[12] H. S. M. Coxeter and S. L. Greitzer. “Ptolemy’s Theorem and its Extensions”. In: *Geometry Revisited, Mathematical Association of America* (1967), pp. 42–42.

[13] M.E. Deaves. “An Investigation of the Non-Linear 3D Flow Effects Relevant for Leading Edge Inflatable Kites”. MSc Thesis, Delft University of Technology, 2015.

[14] P. Demkowicz. “Numerical analysis of the flow past a leading edge inflatable kite wing using a correlation-based transition model”. MSc thesis, Delft University of Technology, The Netherlands, 2019.

[15] M. Diehl. “Real-Time Optimization for Large Scale Nonlinear Processes”. In: 920 (Jan. 2001).

[16] M. Diehl et al., ed. *The International Airborne Wind Energy Conference 2017: Book of Abstracts*. Freiburg, Germany: University of Freiburg | Delft University of Technology, Oct. 5–6, 2017. 188 pp. DOI: 10.6094/UNIFR/12994.

[17] C. Elfert et al. *Measurement of the Turning Behaviour of Tethered Membrane Wings Using Automated Flight Manoeuvres*. 2021.

[18] M. Erhard and H. Strauch. “Theory and experimental validation of a simple comprehensible model of tethered kite dynamics used for controller design”. In: vol. Ch.8. 2013, pp. 141–65. DOI: http://dx.doi.org/10.1007/978-3-642-39965-7_8.

[19] L. Fagiano et al. “Automatic crosswind flight of tethered wings for airborne wind energy: modeling, control design and experimental results”. In: *IEEE Trans Control Sys Technol* (2014). DOI: http://dx.doi.org/10.1109/TCST.2013.2279592.

[20] U. Fechner and R. Schmehl. “Model-Based Efficiency Analysis of Wind Power Conversion by a Pumping Kite Power System”. In: *Airborne Wind Energy*. Ed. by U. Ahrens, M. Diehl, and R. Schmehl. Green Energy and Technology. Berlin Heidelberg: Springer, 2013. Chap. 14, pp. 249–269. ISBN: 978-3-642-39964-0. DOI: 10.1007/978-3-642-39965-7_14.

[21] U. Fechner and R. Schmehl. “Feed-Forward Control of Kite Power Systems”. In: *Journal of Physics: Conference Series* 524.1 (2014), p. 012081. DOI: 10.1088/1742-6596/524/1/012081.

[22] U. Fechner and R. Schmehl. “Flight Path Planning in a Turbulent Wind Environment”. In: *Airborne Wind Energy – Advances in Technology Development and Research*. Ed. by R. Schmehl. Green Energy and Technology. Singapore: Springer, 2018. Chap. 15, pp. 361–390. ISBN: 978-981-10-1947-0. DOI: 10.1007/978-981-10-1947-0_15.

[23] U. Fechner et al. “Dynamic Model of a Pumping Kite Power System”. In: *Renewable Energy* 83 (2015), pp. 705–716. DOI: 10.1016/j.renene.2015.04.028.

[24] M. Folkersma and A. Viré. “Flow transition modeling on two-dimensional circular leading edge airfoils”. In: *Wind Energy* 22.7 (2019), pp. 908–921. DOI: 10.1002/we.2329.

[25] M. Folkersma et al. “Steady-state aeroelasticity of a ram-air wing for airborne wind energy applications”. In: *publisher of Physics: Conference Series* 1618 (2020), p. 12. DOI: https://doi.org/10.1088/1742-6596/1618/3/032018.

[26] A. Furey and I. Harvey. “Evolution of neural networks for active control of tethered airfoils”. In: *University of Sussex* (2007), pp. 1–10.

[27] N.H. Geschiere. “Dynamic modelling of a flexible kite for power generation: Coupling a fluid-structure solver to a dynamic particle system”. MSc thesis, Delft University of Technology, The Netherlands, 2014.

[28] M. Geyer. *Earth-Referenced Aircraft Navigation and Surveillance Analysis.* June 2016.

[29] M. Ghilardi. *Innovation Stamp of Kitepower B.V. made by PostNL*. 2021. URL: https://www.tudelft.nl/en/innovation-impact/development-innovation/innovation-stamps/kitepower (visited on 12/05/2021).

[30] *GIMP, an image manipulation program (Version 2.10.24)*. [Computer software]. (2021). URL: https://www.gimp.org/.

[31] E. Hairer and G. Wanner. “Stiff differential equations solved by Radau methods”. In: *Journal of Computational and Applied Mathematics 111 (1999) 93–111* (Apr. 1998).

[32] J. Hummel. “Automatisierte Vermessung und Charakterisierung der dynamischen Eigenschaften seilgebundener, vollflexibler Tragflächen”. Technical University Berlin, PhD Thesis, 2017.

[33] J. Hummel et al. “Automatic Measurement and Characterization of the Dynamic Measurands of Tethered Flexible Wings”. In: *Wind Energy Science* 4.1 (Jan. 2019), pp. 41–55. DOI: 10.5194/wes-4-41-2019.

[34] S. Jonard. “In-flight measurement of kite deformations with inertial sensors”. MSc Thesis, Delft University of Technology, 2021.

[35] R. van Kappel. “Aerodynamic Analysis Tool for Dynamic Leading Edge Inflated Kite Models: A Non-Linear Vortex Lattice Method”. MSc thesis, Delft University of Technology, The Netherlands, 2012.

[36] A. Kleidon. “Physical limits of wind energy within the atmosphere and its use as renewable energy: From the theoretical basis to practical implications”. In: *Meteorologische Zeitschrift* (2020). DOI: 10.1127/metz/2021/1062.

[37] E. F. van der Knaap. “A Particle System Approach for Modelling Flexible Wings with Inflatable Support Structures”. MSc thesis, Delft University of Technology, The Netherlands, 2013.

[38] G. Lebesque. “Steady-state (RANS) simulation of a leading edge inflatable wing with chordwise struts”. MSc Thesis, Delft University of Technology, 2020.

[39] M. de Lellis et al. “The Betz limit applied to Airborne Wind Energy”. In: *Renewable Energy* 127 (2018), pp. 32–40. DOI: 10.1016/j.renene.2018.04.034.

[40] R.C. Leuthold. “Multiple-Wake Vortex Lattice Method for Membrane Wing Kites”. MSc thesis, Delft University of Technology, The Netherlands, 2015.

[41] M. L. Loyd. “Crosswind kite power”. In: *Journal of Energy* 4.3 (1980), pp. 106–111. DOI: 10.2514/3.48021.

[42] M. Maughmer. *A comparison of the aerodynamic characteristics of eight sailwing airfoil sections.* 1972.

[43] F. Miller Maley et al. “On the areas of cyclic and semicyclic polygons”. In: *Advances in Applied Mathematics* 34.4 (2005). Special Issue Dedicated to Dr. David P. Robbins, pp. 669–689. ISSN: 0196-8858. DOI: https://doi.org/10.1016/j.aam.2004.09.008.

[44] B.G. Newman and H.T. Low. “Two-dimensional impervious sails: experimental results compared with theory”. In: *Journal of Fluid Mechanics* 144:445–462 (Apr. 1984).

[45] M.N. Noom. “Theoretical Analysis of Mechanical Power Generation by Pumping Cycle Kite Power Systems”. MSc thesis, Delft University of Technology, The Netherlands, 2013.

[46] J. Oehler. “Measuring apparent flow vector on a flexible wing kite”. In: (May 17, 2017). DOI: 10.18419/opus-9890.

[47] J. Oehler and R. Schmehl. “Aerodynamic characterization of a soft kite by in situ flow measurement”. In: *Wind Energy Science* 4.1 (Jan. 2019), pp. 1–21. DOI: 10.5194/wes-4-1-2019.

[48] J. Oehler et al. “Experimental investigation of soft kite performance during turning maneuvers”. In: *Journal of Physics: Conference Series* 1037.5 (2018), p. 052004. DOI: 10.1088/1742-6596/1037/5/052004.

[49] S. Piperno. “Design of efficient partitioned procedures for the transient solution of aeroelastic problems”. In: *Revue Europeenne des Elements* 9 (2000). DOI: 10.1080/12506559.2000.10511480.

[50] *Python, a programming language (Version 3.7)*. [Computer software]. (2020). URL: https://www.python.org/.

[51] M.R. van Reijen. “The turning of kites, a quantification of known theories”. MSc Thesis, MSc Thesis, Delft University of Technology, 2018.

[52] Paris REN21 Secretariat. “Renewables 2020 Global Status Report”. In: *ISBN 978-3-948393-00-7* (2020).

[53] A. Roullier. “Experimental analysis of a kite system’s dynamics”. MSc Thesis, Delft University of Technology, 2020.

[54] M.B. Ruppert. “Development and Validation of a Real Time Pumping Kite Model”. MSc Thesis, Delft University of Technology, The Netherlands, 2012.

[55] H.J. Schek. “The force density method for form finding and computation of general networks”. In: *Computer Methods in Applied Mechanics and Engineering* 3.1 (1974). Special Issue Dedicated to Dr. David P. Robbins, pp. 115–134. ISSN: 0196-8858. DOI: https://doi.org/10.1016/0045-7825(74)90045-0.

[56] M. Schelbergen and R. Schmehl. “Validating a dynamic performance model for flexible kite pumping airborne wind energy systems”. In: *16th EAWE PhD Seminar on Wind Energy* (2020).

[57] M. Schelbergen and R. Schmehl. “Validation of the quasi-steady performance model for pumping airborne wind energy systems”. In: *Journal of Physics: Conference Series 1618 (TORQUE 2020)* (2020). DOI: 10.1088/1742-6596/1618/3/032003.

[58] R. Schmehl. “Kiting for Wind Power”. In: *Wind Systems Magazine* 7 (July 2012). URL: http://www.windsystemsmag.com/media/pdfs/Articles/2012_July/0712_Kite.pdf.

[59] R. Schmehl. *Airborne wind energy: an introduction to an emerging technology*. EU Horizon 2020 doctoral training network AWESCO. June 20, 2019. URL: http://awesco.eu/awe-explained/ (visited on 02/15/2021).

[60] R. Schmehl and M. Folkersma. “Airborne Wind Energy System Modelling, Control and Optimisation”. In: *AWESCO* (Dec. 24).

[61] R. Schmehl et al. “Traction Power Generation with Tethered Wings”. In: *Airborne Wind Energy*. Ed. by U. Ahrens, M. Diehl, and R. Schmehl. Green Energy and Technology. Berlin Heidelberg: Springer, 2013. Chap. 2, pp. 23–45. ISBN: 978-3-642-39964-0. DOI: 10.1007/978-3-642-39965-7_2.

[62] J. Schwoll. “Finite Element Approach for Statically Loaded Inflatable Kite Structures”. MSc thesis, Delft University of Technology, The Netherlands, 2012.

[63] *SciPy, an scientific computing package for Python (Version 1.7.2)*. [Computer software]. (2021). URL: https://scipy.org/.

[64] R.W. Smith. “A viscous flow based membrane wing model”. Phd thesis, University of Florida, U.S., 1994.

[65] T. S. Taylor. *Introduction to Laser Science and Engineering.* 2019.

[66] E. Terink et al. “Flight Dynamics and Stability of a Tethered Inflatable Kiteplane”. In: *Journal of Aircraft* 48.2 (Mar. 2011), pp. 503–513. ISSN: 0021-8669. DOI: 10.2514/1.C031108.

[67] J. van Til et al. “Dynamic Model of a C-shaped Bridled Kite Using a few Rigid Plates”. In: *Airborne Wind Energy*. Ed. by U. Ahrens, M. Diehl, and R. Schmehl. Green Energy and Technology. Berlin Heidelberg: Springer, 2018. Chap. 5, pp. 99–115. DOI: https://doi.org/10.1007/978-981-10-1947-0_5.

[68] R. van der Vlugt et al. “Design and Experimental Characterization of a Pumping Kite Power System”. In: *Airborne Wind Energy*. Ed. by U. Ahrens, M. Diehl, and R. Schmehl. Green Energy and Technology. Berlin Heidelberg: Springer, 2013. Chap. 23, pp. 403–425. ISBN: 978-3-642-39964-0. DOI: 10.1007/978-3-642-39965-7_23.

[69] R. van der Vlugt et al. “Quasi-Steady Model of a Pumping Kite Power System”. In: *Renewable Energy* 131 (Feb. 2018), pp. 83–99. DOI: 10.1016/j.renene.2018.07.023.

[70] R.M. Waldman and K.S. Breuer. “Shape, lift, and vibrations of highly compliant membrane wings”. In: *Fluid Dynamics Conference, San Diego, California* 43 (2013).

[71] P. Williams, B. Lansdorp, R. Ruiterkamp, and W. Ockels. “Modeling, simulation, and testing of surf kites for power generation”. In: *AIAA Journal* 6693 (2008), pp. 18–21. DOI: https://doi.org/10.2514/6.2008-6693.

[72] P. Williams et al. “Flexible Tethered Kite with Moveable Attachment Points, Part I: Dynamics and Control”. In: *Collection of Technical Papers - 2007 AIAA Atmospheric Flight Mechanics Conference* 2 (Aug. 2007). DOI: 10.2514/6.2007-6628.

[73] L. Zhang et al. “A loosely-coupled scheme for the flow-induced flapping problem of two-dimensional flexible plate with strong added-mass effect”. In: *Ocean Engineering* 217 (2020). DOI: https://doi.org/10.1016/j.oceaneng.2020.107656.

A

Geometry specifications

This appendix serves to provide numerical details of the design of the V3 that were retrieved during this research. In figure A.1 the KCU bridle line system is shown. J.Breuer, the CTO of Kitepower B.V., provided the length specifications. The depower tape is 0.2 m at maximum power settings and 5 m at minimal power setting. The steering tapes are both 1.6 m in neutral position and at steering settings of 100% the steered side becomes 0.2 m and the non-steered side 3 m. The red lines are both 5.2 m long.

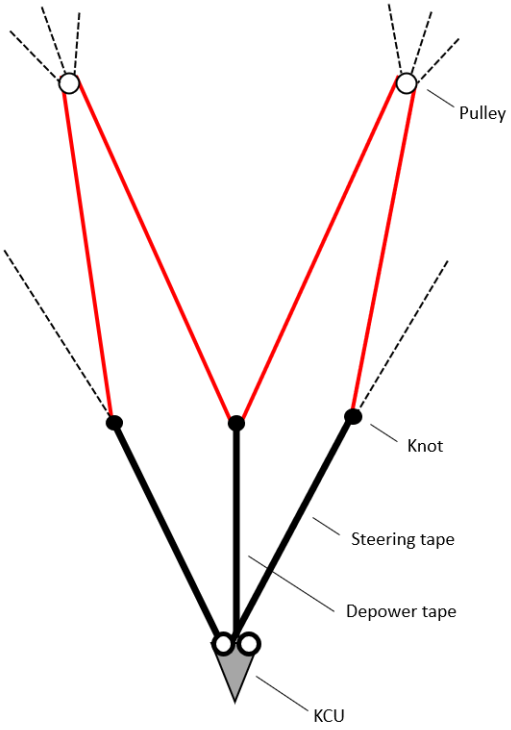

Figure A.1: KCU bridle line system.

In figure A.2 an altered flat kite shape of the V3 is shown. Where each point, representing a bridle line attachment point is numbered. In figure A.3 and A.4 the TE and LE bridle line systems respectively are shown as they are modelled. Each knot and pulley is identified and numbered. The parameters are numbered, such that the reversed engineered coordinates of the V3 design state based on the CAD drawing of 2012, can be represented in table A.1.

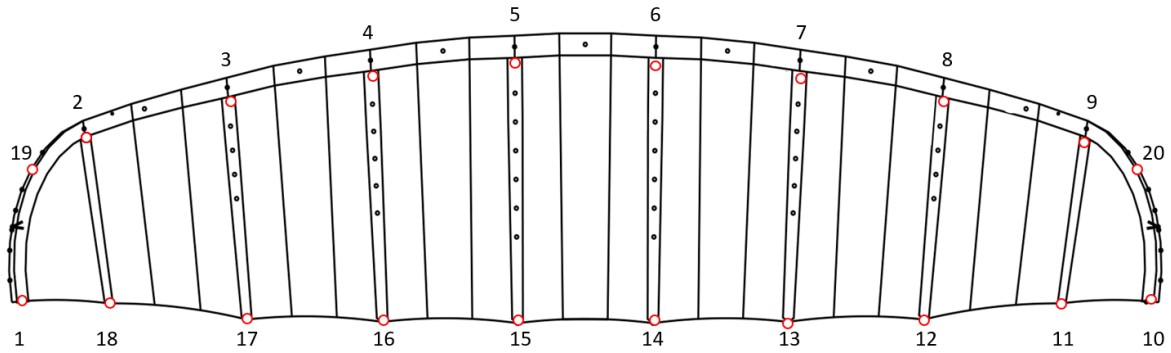

Figure A.2: Altered view of the flat V3 shape, where the bridle attachment points are indicated [60].

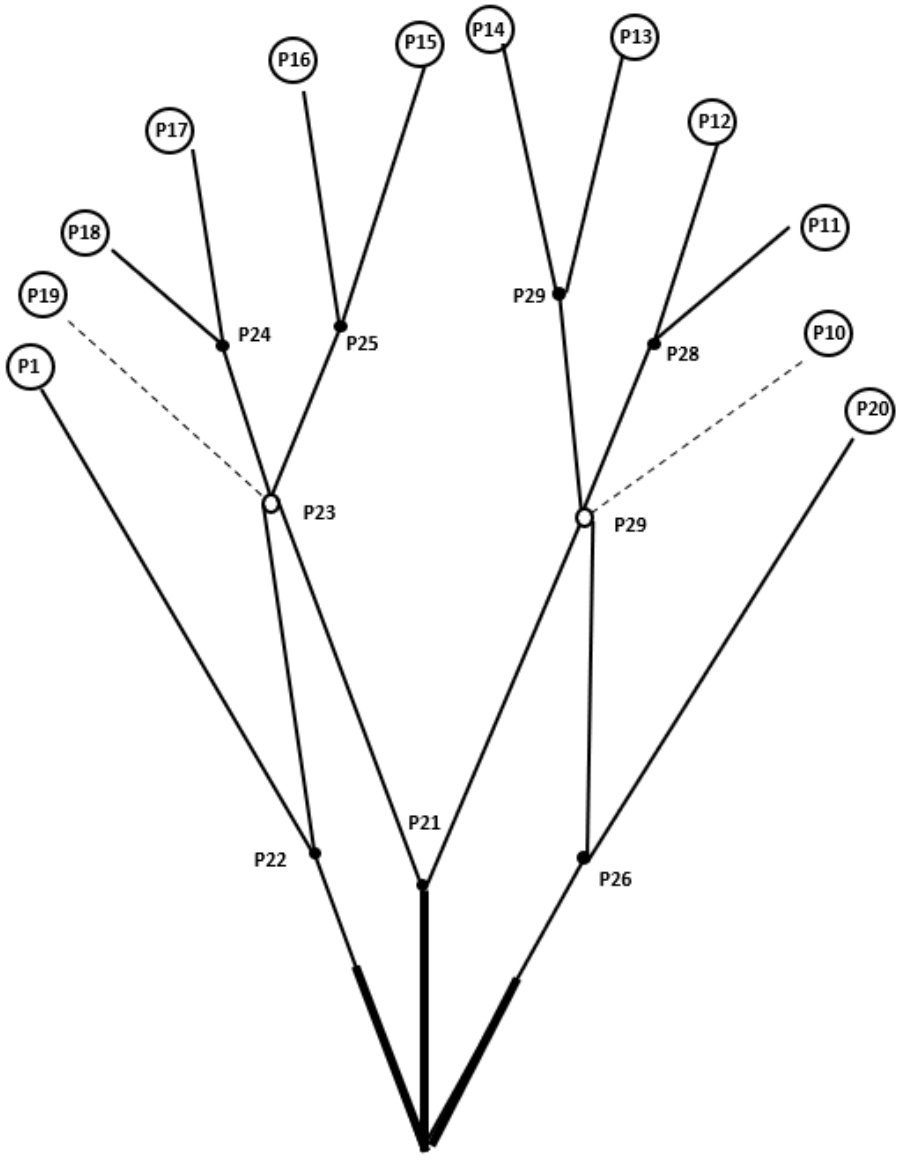

Figure A.3: Schematic illustration of the TE bridles, with the particles numbered.

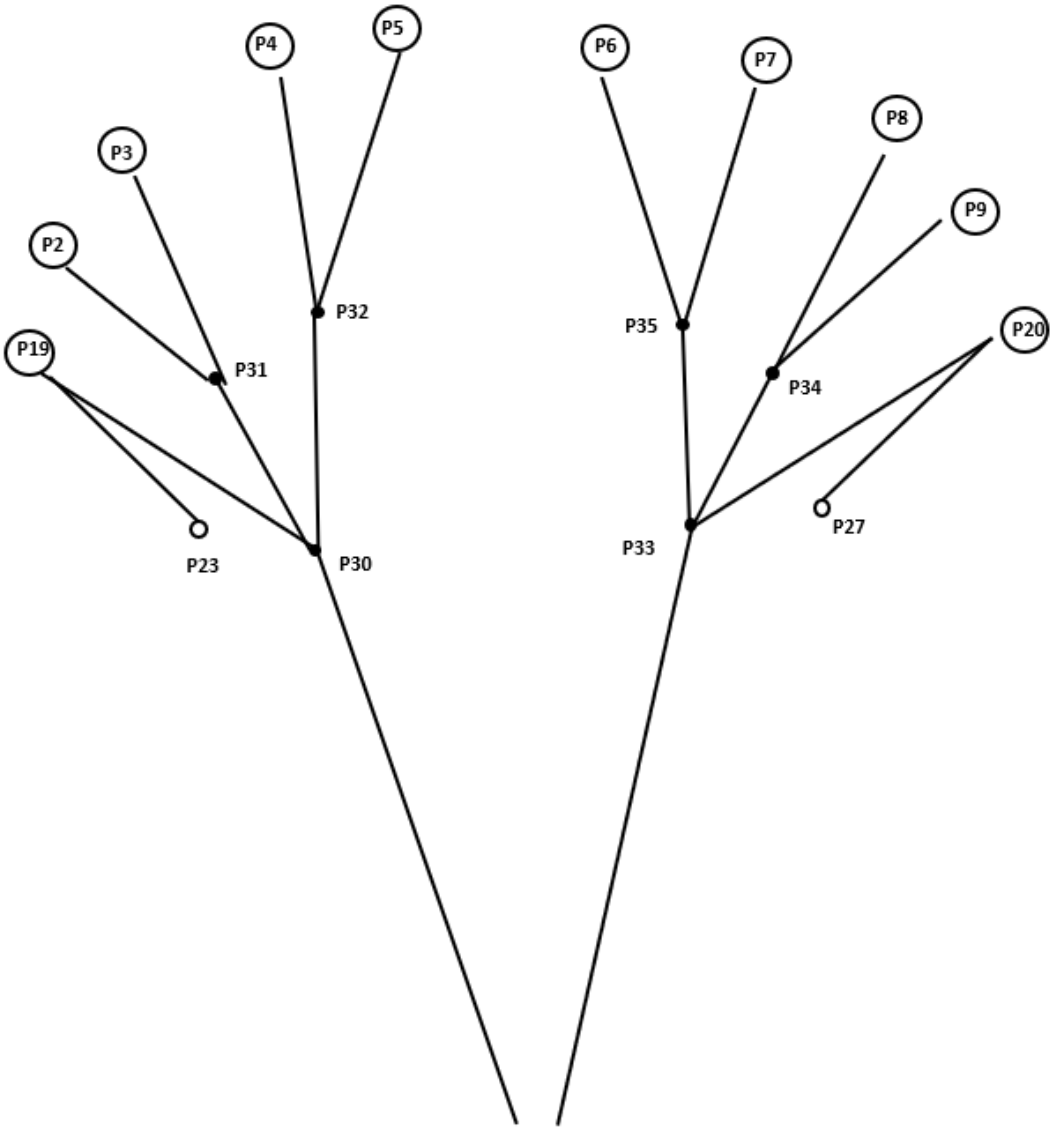

Figure A.4: Schematic illustration of the LE bridles, with the particles numbered.

Point Number	x-coordinate [mm]	y-coordinate [mm]	z-coordinate [mm]
1	0	0	0
2	1366	4142	7099
3	477	3952	8006
4	230	3069	8905
5	69	1942	9548
6	0	661	9800
7	0	-661	9800
8	69	-1942	9548
9	230	-3609	8905
10	477	-3952	8006
11	1366	-4142	7099
12	1801	-3947	8024
13	2057	-3135	9059
14	2145	-1979	9698
15	2200	-666	9843
16	2200	666	9843
17	2145	1979	9698
18	2057	3135	9059
19	1801	3947	8024
20	819	4129	7091
21	819	-4129	7091
22	238	0	1047
23	659	1209	2981
24	1203	1646	5416
25	1555	2905	6932
26	1594	1386	7169
27	659	-1209	2981
28	1203	-1646	5416
29	1555	-2906	6932
30	1594	-1386	7169
31	88	1762	5223
32	181	2713	6733
33	63	1499	7391
34	88	-1762	5223
35	181	-2713	6733
36	63	-1499	7391

Table A.1: Design specifications, with the coordinates of each point given.